UNIVERSITÀ DEGLI STUDI DI PADOVA


UNIVERSITÀ DEGLI STUDI DI PADOVA

**DIPARTIMENTO DI INGEGNERIA INDUSTRIALE (DII)**

LAUREA MAGISTRALE IN INGEGNERIA AEROSPAZIALE


---

# Numeric comparative study on Advanced Nozzles in subsonic counter-flows


*Supervisor:*

**Daniele PAVARIN**

*Co-supervisors:*

**Giuseppe SCARLATELLA**

**Martin PROPST**

*Candidate:*

**Marco GARUTTI**

**2026872**


**ACADEMIC YEAR 2022/2023**

*Your assumptions are your windows on the world.*
*Scrub them off every once in a while, or the light won't come in.*

Alan Alda

# *Riassunto*

Al giorno d'oggi, la stragrande maggioranza dei razzi regolarmente commercializzati impiega convenzionali ugelli a campana, i quali si stanno avvicinando ai loro limiti di miglioramento. Alcuni concept di ugelli avanzati (ANC) offrono potenziali soluzioni alternative per la futura generazione di veicoli di lancio riutilizzabili (RLV). Nell'ottica migliorare le prestazioni delle manovre di recupero (Powered Descent and Landing), l'integrazione di queste tecnologie negli RLV sembra essere promettente, grazie alla loro capacità di compensazione ad altitudine variabile. In particolare, durante la fase finale della manovra – nota come landing burn – il veicolo affronta una fase di retro-propulsione subsonica, in cui il motore viene acceso in direzione opposta al contro-flusso ambientale. Questo studio mira a valutare e confrontare le prestazioni aerodinamiche e degli ugelli di un RLV durante quest'ultima fase. Ciò è condotto nell'ecosistema del software ANSYS Fluent, tramite simulazioni CFD di quattro distinti concept di ugello: convenzionale ugello a campana (due diversi design: un profilo Rao parabolico e un Truncated-Ideal-Contour), Aerospike, Expansion-Deflection e Dual-Bell. Ognuna di queste tipologie è sottoposta a sua volta a test in quattro scenari: static burn on- e off-design (rispettivamente motore funzionante al punto di progetto e a SLS, senza alcun controflusso), discesa aerodinamica (con motore spento ma contro-flusso attivato) e retro-propulsione subsonica (con motore e controflusso attivati). I risultati numerici vengono successivamente confrontati e convalidati con una parallela campagna sperimentale condotta sugli stessi casi in laboratorio.

# *Abstract*

In the present era, the vast majority of regularly manufactured rockets employ conventional Bell Nozzles, which are approaching their limits of improvement. Advanced Nozzle Concepts (ANCs) offer potential alternative solutions for the future generation of Reusable Launch Vehicles (RLVs). Integrating these technologies into RLVs holds promise for enhancing the performance of Powered Descent and Landing (PDL) recovery maneuvers, owing to their capacity for altitude compensation. Specifically, during the final stage of PDL – known as the landing burn maneuver – the vehicle undergoes a subsonic retro-propulsion phase, wherein the engine is ignited against a low-speed counter-flow. This study aims to assess and compare the aerodynamic and nozzle performance of a reusable launch vehicle during this latter phase. The evaluation is conducted using the ANSYS Fluent software environment, employing Computational Fluid Dynamics (CFD) numerical simulations of four distinct nozzle concepts: conventional bell nozzle (including two different designs: Rao parabolic and Truncated-Ideal-Contour), Aerospike, Expansion-Deflection, and Dual Bell nozzles. Each of these concepts is subjected to testing under four scenarios: on- and off-design static burns (respectively with the engine operating at the design point and at SLS, without any counter-flow), aerodynamic descent (with the engine off and counter-flow activated), and subsonic retro-propulsion (with both the engine and counter-flow activated). The numerical results are subsequently compared to and validated against a parallel experimental campaign conducted on the same cases.

# *Contents*

# *List of Figures*

# *List of Tables*

# *Symbol Glossary*

| Symbol | Value | Unit | Description |
|---|---|---|---|
| $\gamma$ | 1.4 | - | Adiabatic index |
| $\varepsilon$ | - | - | Nozzle expansion ratio |
| $\lambda$ | - | $W/mK$ | Thermal conductivity |
| $\rho$ | - | - | Density |
| $A$ | - | $m^2$ | Area |
| $C_D$ | - | - | Drag coefficient |
| $C_F$ | - | - | Nozzle thrust coefficient |
| $C_{F_{opt}}$ | - | - | Nozzle optimal thrust coefficient |
| $D$ | - | $N$ | Drag resistance |
| $f$ | - | N | Momentum flux |
| $F_x$ | - | $N$ | Axial thrust |
| $g$ | 9.81 | $m/s$ | Gravitational acceleration |
| $h$ | - | $J$ | Enthalpy |
| $I_{sp}$ | - | $s$ | Specific Impulse |
| $\dot{m}$ | - | $kg/s$ | Mass flow rate |
| $M$ | - | - | Mach number |
| $MFR$ | - | - | Momentum-Flux-Ratio |
| $NPR$ | - | - | Nozzle Pressure Ratio |
| $p$ | - | $Pa$ | Static pressure |
| $q$ | - | $Pa$ | Dynamic pressure |
| $r$ | - | $mm$ | Radius |
| $R$ | 287 | $J/KgK$ | Molar gas constant (air) |
| $T$ | - | $K$ | Temperature |
| $u, v$ | - | $m/s$ | Velocity |

| Subscript | Description |
|---|---|
| $\infty$ | Free-stream |
| $a$ | Ambient |
| $c$ | Chamber |
| $b$ | Base |
| 0 | Total |
| $e$ | Nozzle exit |
| $p$ | Propellant |
| $s$ | Side |
| $st$ | Stagnation |

# *Acronyms*

**ACS** ..... Attitude-Control-System

**AR** ..... Aspect Ratio

**AS** ..... Aerospike

**ANC** ..... Advanced Nozzle Concept

**BOS** ..... Background-Oriented Schlieren

**CFD** ..... Computational Fluid Dynamics

**DB** ..... Dual Bell

**DRL** ..... Downrange Landing

**ED** ..... Expansion-Deflection

**FB** ..... Flyback

**FVM** ..... Finite Volume Method

**GTO** ..... Geostationary-Transfer-Orbit

**HPC** ..... High-Performance Computing

**LEO** ..... Low-Earth-Orbit

**MAR** ..... Mid-Air recovery

**MECO** ..... Main Engine Cutoff

**MFR** ..... Momentum-Flux-Ratio

**NPR** ..... Nozzle Pressure Ratio

**offD** ..... Off-Design

**onD** ..... On-Design

**PDL** ..... Powered Descent Landing

**RANS** ..... Reynolds-Averaged-Navier-Stokes

**RCS** ..... Reaction-Control-System

**RLV** ..... Reusable Launch Vehicle

**RTLS** ..... Return To Launch Site

**SOTA** ..... State-Of-The-Art

**SSTO** ..... Single-Stage-To-Orbit

**SubRP** ..... Subsonic Retro-Propulsion

**SupRP** ..... Supersonic Retro-Propulsion

**TIC** ..... Truncated-Ideal-Contour

**TSTO** ..... Two-Stage-To-orbit

**TUD** ..... Technsiche Universität Dresden

**TWR** ..... Thrust-to-Weight-Ratio

**VTHL** ..... Vertical Take-off and Horizontal Landing

**VTVL** ..... Vertical Take-off and Vertical Landing

**V&V** ..... Verification and Validation

# *Chapter 1*

# *Introduction*

The field of space launches has always been characterized by high costs. Since the inception of the earliest space missions, major companies have been seeking new strategies to mitigate expenses, which in the first decades (from the '50s until the Space Shuttle) remained exceedingly high – above 10 $k\$/kg$ for LEO missions. The massive technology development brought significant results, lowering the expense to 2.7 $k\$/kg$ for Falcon 9, and 1.4 $k\$/kg$ for Falcon Heavy (SpaceX) [1].

A critical turning point was marked by the introduction of Reusable Launch Vehicles (RLVs), with the first notable attempts at achieving full reusability dating back to the 1990s (with the McDonnell-Douglas DC-X and the Lockheed Martin X-33 VentureStar). These early endeavors have paved the way for recent successful landing operations. RLVs have played a vital role in further reducing costs by minimizing the need for construction materials and fostering the development of sustainable strategies [2].

Within this context, retro-propulsion has emerged as a fundamental element, particularly in the most successful recovery strategy to date: the Powered Descent and Landing (PDL), operated by SpaceX (Fig. 1.1). PDL consists of a sequence of precise phases, that always conclude with the "landing burn": the primary focus of this work. During the landing burn, the vehicle ignites its engine against the free-stream of the surrounding air, creating a subsonic counter-flow, until the final touch down.

However, the physics behind this phenomenon still has to be properly investigated. This is mainly due to the fact that the state-of-the-art (SOTA) involves only the use of conventional bell-shaped nozzles. This is where the Advanced Nozzle Concepts (ANCs) fit in: according to Hagemann et al. [4], alternative nozzle designs offer diverse opportunities to enhance performance significantly, thereby avoiding losses of up to 15% and potentially yielding substantial gains in payload capacity. It is therefore interesting to study how some of them work in this partic-

Credits: SpaceX [3].

Figure 1.1: Falcon Heavy boosters landing.

ular context, especially because of their altitude adaptive capability [5].

This work is carried out as a follow-up and deepening of what was done by Tapia Mancera at TU Dresden [6]; as such, it compares two designs of conventional bell nozzle (a Truncated Ideal Contour and a parabolic Rao) with three other kinds of advanced nozzles: the Aerospike (AS), the Expansion-Deflection (ED) and the Dual Bell (DB). Various aspects and scenarios will be examined, encompassing engine performance during static burns, aerodynamic characteristics, and behavior during retro-propulsion.

The study primarily relies on a CFD (Computational Fluid Dynamics) analysis, employing RANS simulations conducted using ANSYS Fluent software. The geometry and setup design approach aimed to align as much as possible to the experiments in the wind gallery at the Institut für Luft- und Raumfahrttechnik of TUD – simultaneously performed by Scarlatella [7] and another student working on his thesis at the department – in order to use their data to validate the numerical results. It is worth anticipating that a complete matching has not been feasible due to technical and practical constraints, which will be further elucidated in subsequent discussions.

The analysis of the simulation results will offer an overview of the strengths and weaknesses associated with the various nozzle concepts, particularly in relation to altitude compensation. Furthermore, it will serve as a foundation for future studies with more specific objectives.

# *Chapter 2*

# *Background Theory and Literature*

## 2.1 Reusable Launch Vehicles (RLVs)

A reusable launch vehicle (RLV) is a space vehicle that enables the effective recovery of many of its functional parts, such as rocket engines, fuel and oxidizer tanks, and structures, so those can be used once more with little if any reconditioning or maintenance. Initially, attempts at recovery involved Single-Stage-To-Orbit (SSTO) vehicles (as the NASA DC-XA in fig.2.1); however, companies swiftly shifted their focus towards multi-stage concepts, a more practical and reasonable solution that allows for better adaptation of the engines to their operational conditions and eliminates a significant amount of inert mass at the desired route point. Thus we are going to concentrate on the recovery of the first stage, which is clearly the most valuable component one may be interested in; especially related to the perspective of gradually increasing the launch rate per year and reducing the costs.

In order to classify the recovery strategies, Vernacchia proposes the following diversification by four high-level choices (see fig.2.2) [9]:

1. *Recovery Location* - The stage has two landing location possibilities: return to the launch site (RTLS) or downrange landing (DRL). The first option requires a boost-back maneuver to make the stage aimed again at the launch site; the second occurs away from it, usually on a ship, in another platform in the ocean or on land, or in mid-air with the support of an aircraft (phases described in Section 2.2) [10].

2. *Recovery propulsion method* - Re-entry is achieved by re-igniting the rocket engine (Retro-propulsion), by using additional air-breathing engines, or simply gliding or falling into the desired location, by taking advantage of the aerodynamic drag.

Credits: NASA [2, 8].

Figure 2.1: NASA picture of the DC-XA (1996): unsuccessful project for a prototype SSTO reusable vehicle with the main goal of performing a vertical take-off and landing.

3. *Landing method* - The stage may land under parachutes; on the other hand it may fire its engines to perform the Vertical Take-off - Vertical Landing (VTVL) or the Vertical Take-off - Horizontal Landing (VTHL). The first method involves the re-ignition of the rocket's first-stage engine: over several maneuvers phases, which necessarily require a Reaction-Control-System (RCS) to manage the attitude of the vehicle, the latter slows down until the touchdown on the landing legs (a.k.a. Powered Descent and Landing (PDL)). A stage based on the second approach (VTHL), is instead furnished with wings and, to decelerate, counts only on the aerodynamic forces. VTHL in turn can proceed in two forms: with the In-Air Capturing (IAC) – a.k.a. Mid-Air-Recovery (MAR) – or with the so-called Flyback (FB) method. In both cases, the stage crosses the hypersonic regime and reaches the supersonic one; then in the IAC a second vehicle (aircraft) kicks in, which captures the first one and leads it to the landing site. Alternatively, with the Flyback, the stage starts up its own turbine engines and performs the same procedure by itself. Nonetheless, the FB demand additional propellant to be carried out for the maneuver, similar to a VLVT. [10].

4. *Portion of first stage recovered* - Some recovery procedures seek to recover the entire initial stage, while others merely aim to recover the higher value components (such as the main engines).

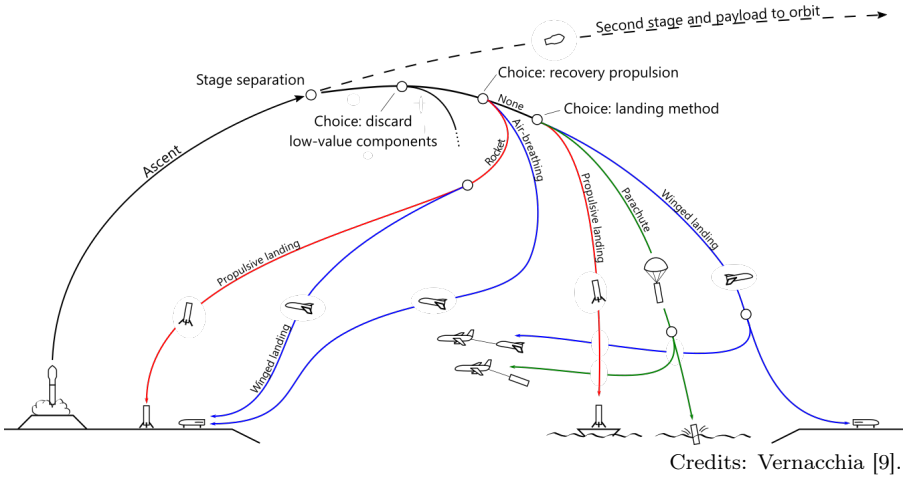


Figure 2.2: First stage recovery strategies.

## 2.2 Powered Descent and Landing

Nowadays, the most frequently used technique for RLVs is the powered descent and landing (PDL). SpaceX adopts retro-propulsion as a landing recovery strategy in both the Falcon Heavy (Fig.1.1) and the Falcon 9: so far the best reusable rocket and the only Two-State-To-Orbit (TSTO) systematically produced and used with proven success (with, at the time of writing, 217 launches and 175 landings [11]). The first stage of such a vehicle is able to perform both the mentioned maneuvers of RTLS and DRL (see fig.2.3 and fig.2.4), respectively associated with the insertion of small payloads into LEO (Low-Earth-Orbit) and bigger ones in GTO (Geostationary-Transfer-Orbit).

A typical – even if not yet optimized – timeline of recovery, as well as the first successful return of the Falcon 9 first stage, is shown in the table (Fig.2.5). The latter exhibit in detail every step of the Orbcomm-OG2 mission (Falcon 9 flight 20), an RTLS that occurred on 22 December 2015 [13]. There, three distinct boosts can be identified, which also correspond to three of the four phases that characterize every SpaceX recovery [5]:

1. *Boost-back burn* (optional)
2. *Re-entry burn*
3. *Aerodynamic descent*
4. *Landing Burn*

### 2.2.1 Boost-back burn

The boost-back burn is the first powered maneuver that takes place subsequently the Main-Engine-Cut-Off (MECO) (see fig.2.3); It commonly occurs after 15-20 $s$

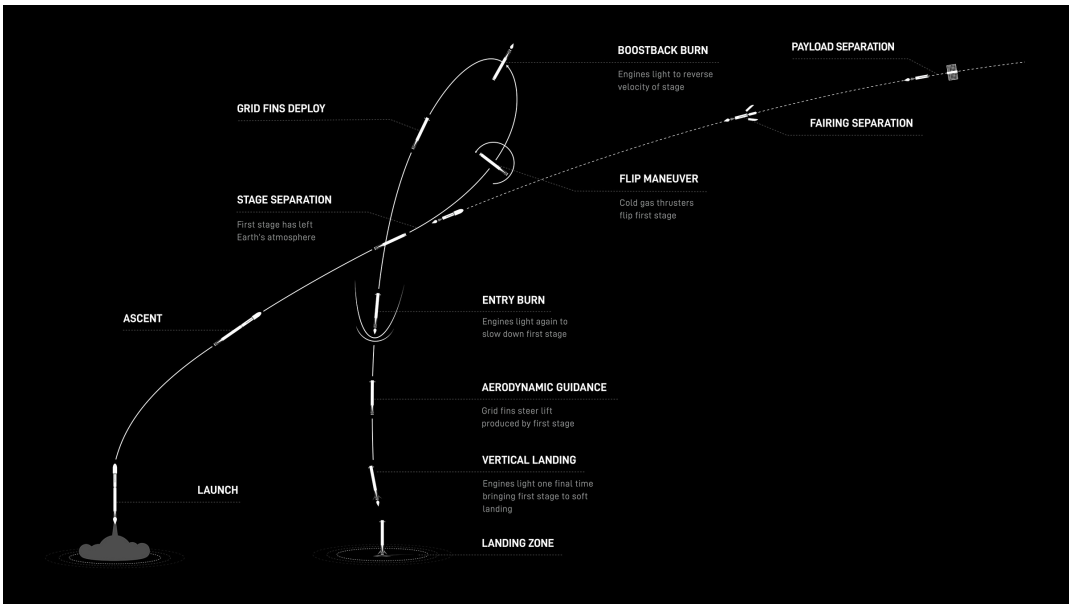


Credits: SpaceX [12].

Figure 2.3: Return To Launch Site (RTLS) SpaceX maneuver.

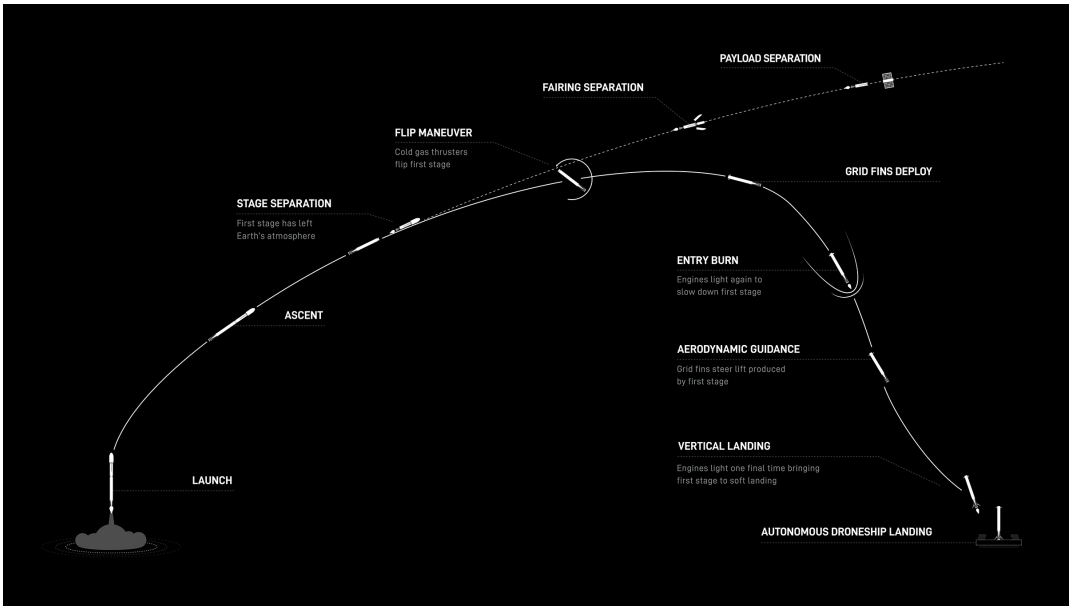


Credits: SpaceX [12].

Figure 2.4: Downrange Landing (DRL) SpaceX maneuver.

| Event | Time [s] | Altitude [km] | Velocity [m/s] |
|---|---|---|---|
| MECO | 0 | 72.9 | 1674.6 |
| 1st burn start | 85.9 | 170.9 | 977.8 |
| 1st burn end | 113.2 | 187.2 | 510.8 |
| Apogee | 153.7 | 194.3 | 361.5 |
| 2nd burn start | 326.0 | 54.0 | 1664.8 |
| *Maximum acceleration* | 354.4 | 23.5 | 442.7 |
| 2nd burn end | 356.7 | 22.6 | 330.0 |
| 3rd burn start | 392.2 | 6.8 | 501.7 |
| *Maximum dynamic pressure* | 392.3 | 6.8 | 501.2 |
| 3rd burn end/landing | 422.6 | 0.004 | 2.25 |

Credits: [14].

Figure 2.5: Timeline of the first stage return for the Orbcomm-OG2 mission.

the latter and above 80 km of altitude. It lasts up to 50 $s$ and drives the vehicle to the trajectory apogee, which can reach altitudes above 130 km [5]. The Orbcomm-OG2 mission seems to display some incoherent values compared to this more recent data, such as the high apogee; this is explained by the comparatively minor pitch-over maneuver carried out at the start of the ascent [14].

The boost-back phase is usually needed only in the case of a RTLS, since it is responsible for reducing/reversing the horizontal component of the velocity and re-orientating the booster towards the landing site. Just in a few cases, a DRL may require it when the guidance through cold thrusters is not sufficient.

At this point, at this altitude is already evident how the conventional bell nozzle is incapable of realizing optimal thrust performance, due to the near-vacuum conditions that induce a strong under-expansion.

### 2.2.2 Re-entry burn (SupRP)

The main stage thus begins the descent, but at a certain point, without re-igniting the engines to slow down, it wouldn't be able to withstand the thermal load it would face. Ecker et al. estimate – at the velocity of $M_\infty = 9.45$ and at $h = 68\ km$ – a temperature of the free-stream up to 3400 $K$, because of the hot gasses coming from the bow shock formed at the aft [15].

Activating the retro-propulsion (usually at around 60 km of altitude) allows to decelerate the vehicle and, at the same time, to drastically reduce the temperature to around 1400 $K$ just after the maneuver, lowering the heat flux by eight times. In exchange, it is more than fair to accept the consequent nearly doubling of the same heat flux on the upper part [5].

This phase of supersonic retro-propulsion (SupRP), which usually lasts about 30 $s$, brings the stage under 40 $km$, guiding it from the hypersonic to the supersonic regime.

### 2.2.3 Aerodynamic descent

When the engines are turned off again, the aerodynamic descent starts, where special control surfaces collaborate with the cold-thrusters of the Attitude-Control-System (ACS) in order to drive the vehicle through increasingly thicker layers of the atmosphere (for a duration of ca. 55 $s$). The thermal load and the dynamic pressure, greatly dependent on the chosen trajectory, are now sustainable thanks to the SupRP phase.

In the first part of the aerodynamic guidance (ca. 30 $s$), the Mach number tends to increase (in RTLS) or at least stays constant (in DRL). Afterward, the drag resistance becomes strong enough to actually start lowering the velocity linearly with altitude [16]. Here's that the *ballistic coefficient* $\beta$ assume an meaningful impact:

$$\beta = \frac{M}{C_D A_{ref}} \tag{2.2.1}$$

The coefficient is defined as the ratio between mass and drag: the lower the value, the higher the aerodynamic resistance suitable for slowing down the vehicle.

### 2.2.4 Landing burn (SubRP)

Finally, the engines are fired for the third and last time for the landing burn (ca. 30-40 $s$), which will be the main focus of this thesis. Table 2.1 shows a few reference values for the start and the end points of the maneuver [5][14]:

Table 2.1: Reference start and end points of a landing burn.

| | **Start** | **End** | **Unit** |
|---|---|---|---|
| Altitude | 6-10 | 0 | $km$ |
| Pressure | 0.47-0.26 | 1.01325 | $bar$ |
| Mach | 1.2-1.5 | $\sim 0.015$ | - |
| Velocity | $> 300$ | $< 5$ | $m/s$ |

This phase of subsonic retro-propulsion (SubRP) is carried out by the re-ignition of the central Merlin engine 2.6, assisted by the activation of hydraulic legs that are able to absorb the residual kinetic energy. In order to achieve a proper *soft landing* at less than 5 $m/s$, the vehicle may follow two approaches: (1) low Thrust-to-Weight-Ratio (TWR) – which accepts a higher propellant cost and throttling capability, in favor of lower mechanical stress and fatigue-life – or (2) high TWR, which reduces the propellant consumption at cost of inferior precision and possibly larger mechanical stress. Generally, a faster maneuver translates into minor performance losses, but a lack of precision and absorption of the mechanical loads. In any case, inaccurate control of the stage may always culminate in a *hard landing*.

## 2.3 Rocket Nozzles design

The performance of a propulsion system can be improved by enhancing the combustion/engine cycle efficiency or the nozzle efficiency. Following the second approach, exploring the potential of Advanced Nozzle Concepts (ANCs) – characterized by their altitude compensation capability – may reveal better performance in PDL of RLVs.

### 2.3.1 Conventional Bell nozzles

Currently, the totality of commercial rocket production is limited to the conventional bell nozzle (e.g. the well-known Merlin engine in fig.2.6). Rightly, the reader might think that there is a reason if this is so; indeed, it is a concept that is been upgraded over the years, starting from the simpler conical nozzle and evolving to various contour design strategies (which will be briefly covered).

Credits: SpaceX, modified image [11].

Figure 2.6: Sea-Level Merlin engine used on Falcon 9 and Falcon Heavy first stages.

Bell nozzles begin with a large divergence angle just downstream of the throat, between 20 and 50° ($\theta_i$); here, the high relative local pressure and pressure gradients, as the rapid expansion of the fluid, prevent the flow separation. The divergence angle then progressively decreases to less than 10° at the nozzle exit ($\theta_e$), smoothly enough to avoid any oblique shock. Compared to the old-fashioned straight cone

nozzle, the bell nozzle exhibits a more efficient gas expansion, which minimizes losses [17, 18].

Out of the variety of possible designs for a bell nozzle, this work will consider two of the most convenient ones – Rao parabolic contour and Truncated-Ideal-Contour (TIC):

- *Rao* - Near-optimum-thrust contour approximation proposed by G. V. R. Rao in 1957, consisting of a first circular entrance section (just after the throat) stitched to a parabolic profile till the exit [18, 19]. It is typically characterized by a percentage value – that specifies the length of the nozzle (from throat to exit) compared to a 15° cone with the same area ratio $\varepsilon$ ($A_e/A_t$) – and a very high turn-back angle, defined as the difference between $\theta_i$ and $\theta_e$ (obviously null in a cone), which are dependent on the required $\varepsilon$ (see fig.2.7) [17].

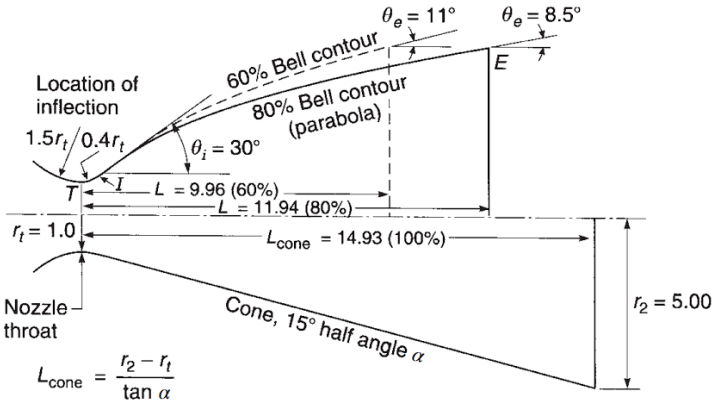


Credits: [17].

Figure 2.7: Comparison between cone and two parabolic bell contours (60% and 80%).

- *TIC* - Truncated version of an Ideal-Contour (IC) nozzle, which in turn is a nozzle designed in order to avoid negative wall pressure gradients. The IC ends with a horizontal tangent, at cost of being very long, so a precisely truncated version may be preferable.

Every bell nozzle is strictly designed in order to answer to precise ambient conditions, since the exhaust gasses have a defined pressure at the exit of the same depending on $\varepsilon$. Therefore, this directly and strongly influences the engine's performance, as we can see in the following axial thrust equation [17]:

$$F_x = \dot{m} \cdot v_e + (p_e - p_a) \cdot A_e \tag{2.3.1}$$

The first term is the *momentum thrust* given by the product of the propellant mass flow rate ($\dot{m}$) and its exit velocity ($v_e$). The second term is the above-mentioned contribution of the *pressure thrust*, where the exit cross-section area $A_e$ is multiplied by the difference between the exit ($p_e$) and the ambient pressure ($p_a$).

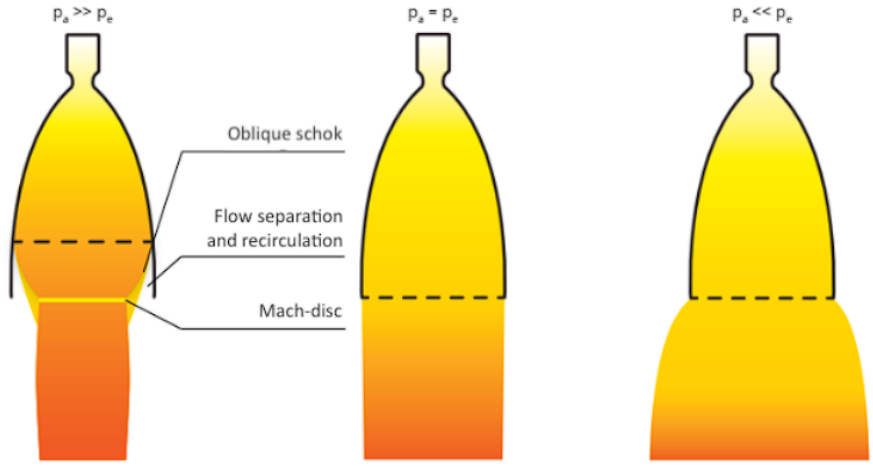


Credits: Bach [20], modified image.

Figure 2.8: Conventional bell nozzle in over- (left), optimal (center) and under- (right) expansion conditions.

If $p_e$ is equal to $p_a$, the engine is operating at its design point with optimal expansion, meaning at its higher efficiency. Otherwise, two possible scenarios may arise:

- *Over-expansion* ($p_a > p_e$) - When the ambient pressure is higher than the exit pressure, it means that the fluid is more expanded than it should be (too large exit area). At a specific point, the regular expansion is suddenly interrupted by a shock wave that occurs to enforce the boundary conditions, causing the separation of the flow from the walls [17].
- *Under-expansion* ($p_a < p_e$) - When the ambient pressure is lower than the exit pressure, the fluid is instead not enough expanded. In this case, the exit area is too small, so further expansion occurs in the ambient, outside of the nozzle.

All the three operative conditions (optimal, over- and under-expansion) are represented in fig.2.8.

### Limitations of conventional bell nozzles in PDL

Bell nozzles of the first stages are conventionally optimized for near Sea-Level-Standard (SLS), at around 40 $kPa$; This, with other inherited characteristics of this kind of design, implies numerous drawbacks during the recovery of the booster. Scarlatella et al. [5] propose an accurate analysis of them, which is here briefly summarized.

During the *boost-back burn*, the three re-ignited nozzles operate with poor efficiency due to the strong under-expansion conditions, since at 80 $km$ the ambient is at near vacuum conditions (far from the nozzle design point).

Out of this, new critical aspects arise in the SupRP phase (*re-entry burn*): the unsteadiness of flow-field behavior coming from plume and shock interactions, and the high thermal loads that challenge the baseplate of the booster [21]. Moreover, the powerful counter-flow could obstruct the transient phase of re-ignition and so the full-thrust potential.

The *landing burn* phase (SubRP) highlights once again the great thermal-loads issue (an aspect that also during the *aerodynamic descent* is not optimized w.r.t. alternative and more suitable configurations). In addition, here conventional bell nozzles exhibit Thrust-Vector-Control (TVC) limitations and lack any kind of altitude compensation capability – which, in a phase where the pressure changes this much (see table 2.1), would bring a huge benefit.

### 2.3.2 Advanced Nozzle Concepts

Exactly where a bell nozzle suffers because of its nature, Advanced Nozzle Concepts (ANCs) may be able to find a spot to shine. Their main goal is to take advantage of the altitude compensation in order to furnish improved performance; in particular, Aerospike (AS) and Expansion-Deflection (ED) nozzles can theoretically achieve a full adaptation, while the Dual-Bell (DB) nozzle is characterized by two-step-wise adaptability (see fig.2.9).

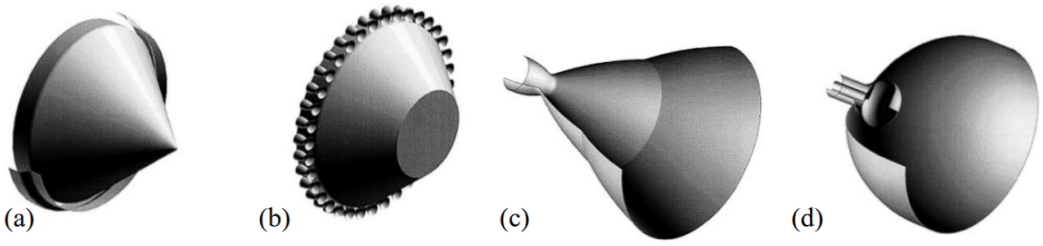


Credits: Hagemann [4], modified image.

Figure 2.9: ANCs models: (**a**) annular aerospike, (**b**) truncated clustered aerospike, (**c**) dual-bell and (**d**) expansion-deflection nozzles

#### Aerospike nozzle

Aerospike nozzles are probably the most unique and trending kind of alternative concept; they can be classified depending on:

- *combustion chamber* – single or clustered chamber (respectively (a) and (b) in fig. 2.9)
- *spike shaping* – full-spike or truncated (respectively (a) and (b) in fig. 2.9)

Figure 2.10 demonstrates how they are theoretically able to achieve an optimal and continuous altitude adaptation.

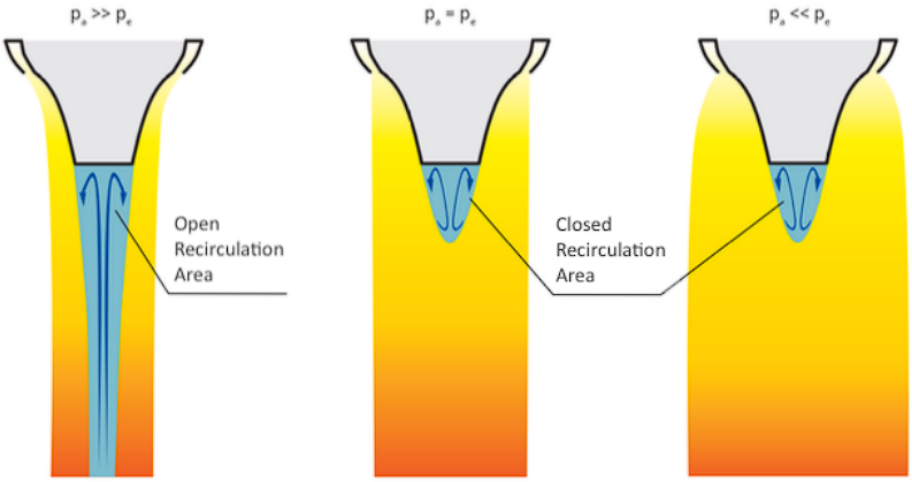


Credits: Bach [20], modified image.

Figure 2.10: Aerospike nozzle in over- (left), optimal (center) and under- (right) expansion conditions.

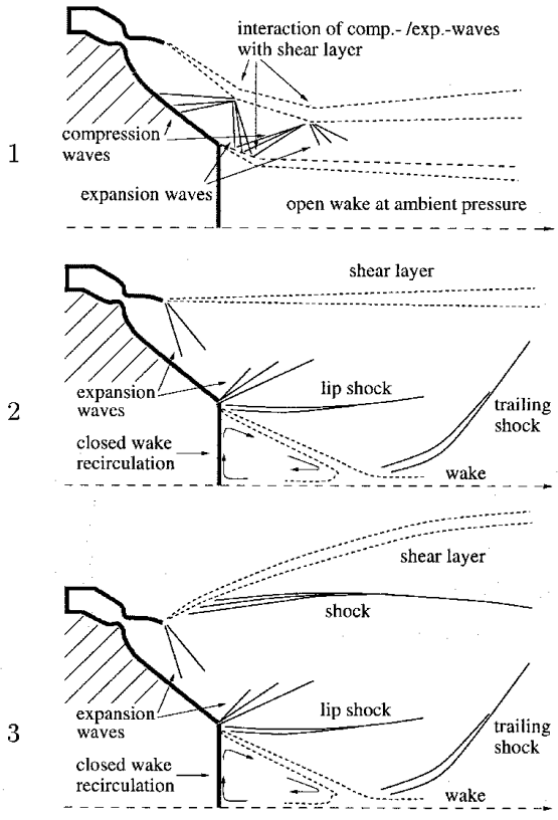


Credits: Hagemann [4], modified image.

Figure 2.11: Flow phenomena of a truncated plug nozzle at different $NPR$ ($p_c/p_a$), off-design (1, 3) and design (2) pressure.

When the external pressure is too high (over-expanded flow), compression and expansion waves keep the jet flow close to the spike walls without any separation, and – in case of truncated nozzle – an open ambient pressure wake is formed (fig. 2.11).

If the ambient pressure is the design one, the flow should develop in the exact axial direction. However, this is true only in theory, since the non-homogeneity in the throat makes it impossible to reach a perfect one-dimensional flow.

Finally, at higher pressure ratios (under-expanded flow), the plume stretches in a barrel-like form, in order to reach the optimal expansion ratio.

### Dual-Bell nozzle

Differently from its cousins, the dual bell nozzle is an advanced concept with a step-wise adaptation (image (c) of fig. 2.9). As such, it is designed to offer optimal adaptation at two different nozzle pressure ratios ($NPR$).

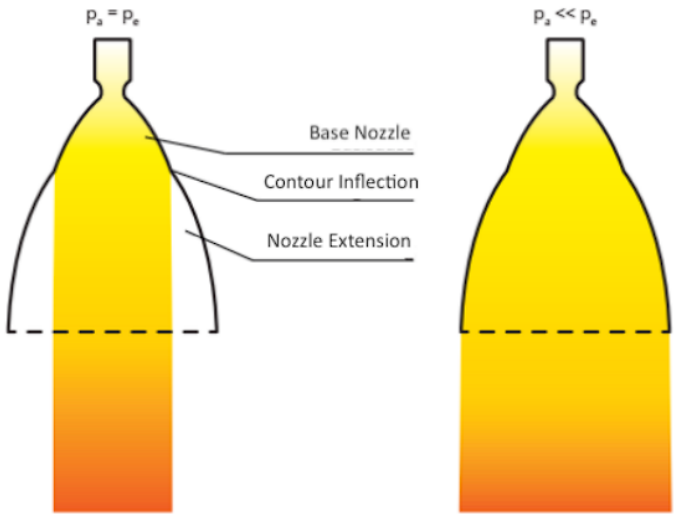


Credits: Bach [20], modified image.

Figure 2.12: Dual-bell nozzle at its high pressure (low altitude) and low pressure (high altitude) design points.

In low altitudes (low $NPR$), the DB acts as a conventional bell nozzle with a small expansion ratio (first wall inflection). But when the altitude increases – and the ambient pressure decreases – the flow attaches to the whole wall until the exit, reaching much higher expansion ratios (figures 2.12 and 2.13).

The transition from the two operative modes is not completely smooth, since occurs before the optimal crossover point, resulting in some thrust losses.

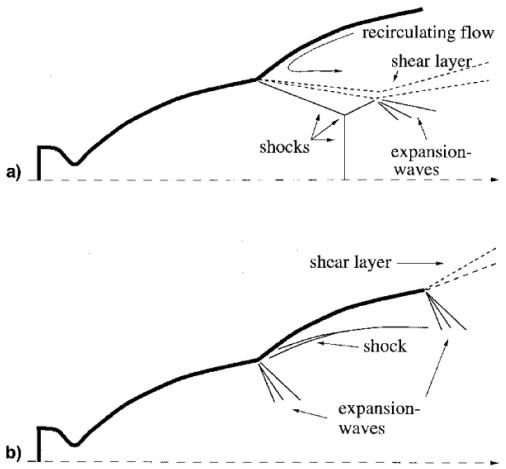


Credits: Hagemann [4].

Figure 2.13: Flowfield phenomena in dual-bell nozzles: a) near SLS mode with flow separation at the wall inflection point and b) altitude mode with a full-flowing nozzle.

### Expansion-Deflection nozzle

Expansion-Deflection nozzles work with the same adaptation principle as the aerospikes, with the main difference being that the compensation takes place from the inside of the nozzle.

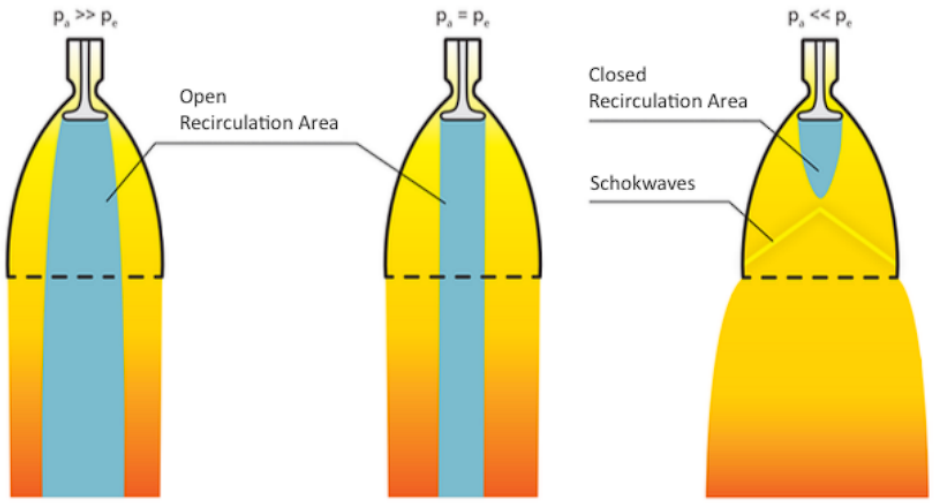


Credits: Bach [20], modified image.

Figure 2.14: Expansion-Deflection nozzle in over- (left), optimal (center) and under- (right) expansion conditions.

At lower altitudes, the combined action of the central body and high pressure (through compression and expansion waves, visible in fig. 2.15) pushes the flow on

the nozzle walls, resulting in a low expansion ratio. While the $NPR$ increases, the flow is allowed to expand, until the middle wake becomes close (fig. 2.14).

Also in this case, this behavior implies some cons: the pressure in the wake is always inferior to the ambient one, due to the aspiration effect, until it becomes almost independent from it during the transition from open to closed. This leads to over-expansion losses, since the exhaust gas expands to this base pressure rather than the ambient one.

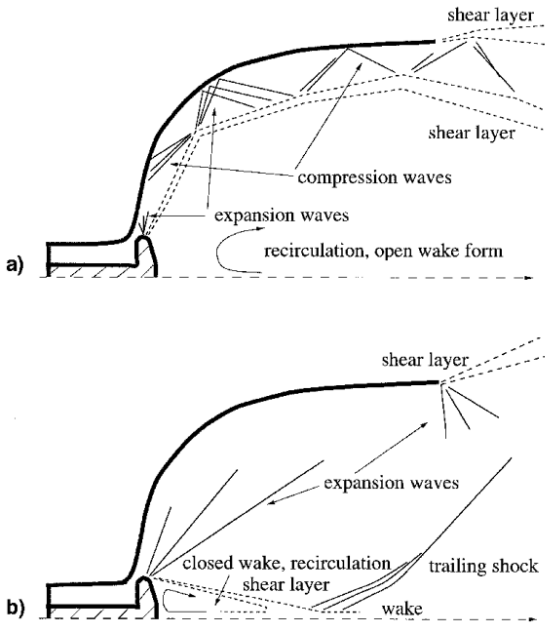


Credits: Hagemann [4].

Figure 2.15: Flow phenomena of an ED nozzle, with a) open and b) closed wakes.

## 2.4 Computational Fluid Dynamics (CFD)

During the 1950s and early 1960s, most aeronautical/space engineers began to deal with complex problems beyond the current state-of-the-art of knowledge and available resources for fluid dynamic analysis. Fortunately, industries and government laboratories were soon able to develop computational techniques to overcome the obstacle. Nowadays, in many fields *Computational Fluid Dynamics* (CFD) represents an incredible tool to do preliminary analysis, or to actually perform numerical experiments, which require the material experience just as fine-tuning or validation support.

One of the crucial advantages of using CFD is the possibility – especially for novice users – of treating the software as a black box, where ready-developed codes are implemented (see fig. 2.16).

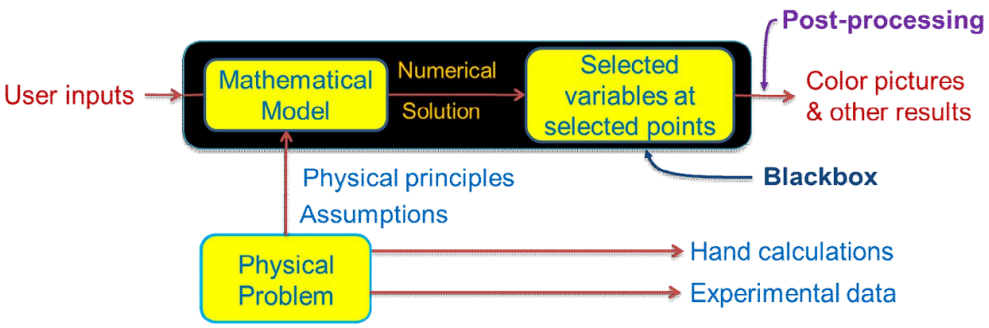


Credits: [22].

Figure 2.16: Schematic representation of CFD black box.

The user can interact with simplified interfaces, getting familiarity with time, but being able very soon to solve some basic problems.

But let's get a little deeper in this black box; every fluid phenomenon is governed by three fundamental conservation laws [23, 24]:

1. *Mass*: must be conserved in the fluid:

$$\frac{\partial \rho}{\partial t} + \nabla \cdot (\rho \mathbf{V}) = 0 \tag{2.4.1}$$

2. *Momentum*: Newton's second law, the rate of change of momentum equals the sum of forces acting on the fluid (a.k.a. Navier-Stokes equations):

$$\rho(\mathbf{V} \cdot \nabla)\mathbf{V} = -\nabla p + \mu \nabla^2 \mathbf{V} \tag{2.4.2}$$

3. *Energy*: First law of thermodynamics, the rate of change of energy equals the sum of the rate of heat addition and the rate of work done on the fluid:

$$\text{Time rate change of energy} = \sum \dot{Q} + \sum \dot{W} \tag{2.4.3}$$

which for a two-dimensional *compressible flow*, becomes:

$$\frac{\partial \rho h}{\partial t} + \frac{\partial (\rho u h)}{\partial x} + \frac{\partial (\rho v h)}{\partial y} = \frac{\partial p}{\partial t} + \frac{\partial}{\partial x}\left[\lambda \frac{\partial T}{\partial x}\right] + \frac{\partial}{\partial y}\left[\lambda \frac{\partial T}{\partial y}\right] + \Phi \tag{2.4.4}$$

where $\Phi$ is the dissipation function.

The basic idea is to take these non-linear coupled conservation principles, divide the flow domain into little chunks and apply them using the integral form, in order to get a system of algebraic equations (Mathematical Model). The latter is advanced in space and/or time – from an initial guess – until convergence, finally obtaining a description of the flow field. After every iteration, the software calculates the numerical residuals for every law with respect to the previous one, which basically constitute errors in the solution. Generally, convergence can be considered achieved when all the residuals are below the specified values (usually inferior of $10^{-5}$), and at the same time the key parameters show stable values in the last iterations.

Typically, every CFD numerical simulation campaign consists of the following steps [22, 23]:

### 1) Problem specification

The first step involves providing a comprehensive description of the physical aspects involved. This includes relevant physics, the specific working fluid, and the boundary conditions. Moreover, the spatial and temporal domains are defined, along with the desired physical quantities and fields of interest.

### 2) Pre-analysis

Prior to conducting the simulations, a preliminary analysis of the problem is conducted by leveraging available experimental data and analytical theories, and through hand calculations. The purpose of this step is to obtain an initial understanding of the flow field's topology and characteristics, in order to serve as a reference for preparing the simulations and verifying the result's accuracy.

### 3) Domain definition and Meshing

It's then time to establish the appropriate dimensions and structure of the domain, typically using external CAD software. Once the geometry is ready, it has to be divided into finite volumes, this process is known as mesh discretization. The mesh varies in size depending on the complexity of the flow field being simulated, ranging from thousands of cells for simpler cases to billions of cells for high-definition simulations. Additionally, it should be finer in the proximity of particular zones of interest as boundary layers and shock waves. An ideal mesh strikes a balance between sufficient resolution, numerical convergence, and minimal cell count to reduce computational costs. Achieving this balance is crucial to obtain accurate and efficient results from simulations [25].

### 4) Model setup

The numerical model setup involves selecting a mathematical model that best represents the expected characteristics of the flow, depending on various factors (e.g., compressible or incompressible, laminar or turbulent, 2D or 3D, steady or unsteady, inclusion of energy/turbulence equations). It is crucial to recognize that the accuracy of computational fluid dynamics (CFD) solutions is directly linked to the level of physics incorporated into their formulation. Once the model is established, the next step is to apply the boundary conditions. These define the physical properties at every boundary surface of the domain (e.g. pressure/velocity inlets/outlets, and walls). These boundary types ensure that the flow variables are mostly independent of the rest of the domain, allowing for a well-defined simulation environment.

**5) Numerical solution**

The configuration for solving the selected mathematical model is established to ensure numerical stability and convergence throughout the solution process. As previously explained, modern software often handles these settings automatically, but there are instances where the user may need to intervene inside the black box, in order to optimize specific algorithms according to desired outcomes.

**6) Numerical results and Post-processing**

Once the simulation is completed, the user can examine the numerical results and generate plots, as vivid contours and animations to clearly visualize the flow behavior.

**7) Verification and Validation (V&V)**

This latter phase plays a crucial role in assessing the precision and reliability of computational simulations. Verification focuses on examining the numerical aspects of the simulation, analyzing the precision of the mathematical model's solution, and determining the level of numerical uncertainty involved (e.g. comparing the results to the pre-analysis ones and verifying the convergence criteria). On the other hand, validation involves comparing the numerical results obtained from the simulation with experimental data, thereby assessing how well the mathematical model represents the real-world phenomena of interest. By conducting the V&V process, the overall confidence in the computational simulation can be established, providing insights into the fidelity and trustworthiness of the results [26].

## 2.5 Literature Review

The academic literature offers valuable data that can be exploited as a starting point for further investigation. In particular, a specific study on subsonic retropropulsion (SubRP) will be considered [27], since it furnishes some interesting hints and trends applicable to the expected results of this thesis.

Moreover, in the Technische Universität Dresden (TUD), previous and parallel test campaigns have been conducted [7, 28], as well as a first CFD study [6]. These add practical insights and empirical evidence to enhance the understanding of the topic.

### 2.5.1 Vertical Landing Aerodynamics of RLVs

Nonaka et al. carried out a paper [27] about the vertical landing phase of a RLV, to study the influences of interaction between the engine plume with the freestream around the vehicle. In order to do so, for the experimental measurements (such as forces and pressure distribution) they used a scaled cold-gas model of a reusable

rocket placed in a wind tunnel. The flow field around the body is visualized using the particle-image-velocimetry (PIV) method.

Figures 2.17 and 2.18 show the vehicle model and the various operative test conditions.

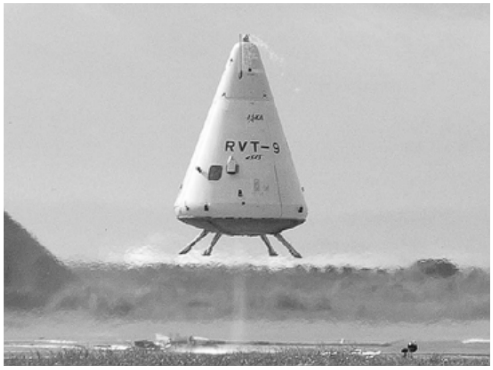


a) RVT vehicle

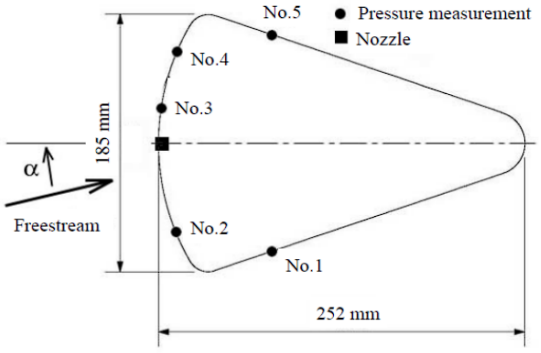


b) Wind tunnel model

Credits: Nonaka et al. [27].

Figure 2.17: RVT vehicle (a) and model (b) for wind tunnel tests.

Table 1. Vehicle flight and wind tunnel test conditions.

| | RVT vehicle flight | Wind tunnel test |
|---|---|---|
| $T_0$ [K] | 3415 | 289 |
| $P_0$ [MPa] | 2.43 | 2.08 |
| $V_\infty$ [m/s] | 70 | 26.4 |
| $M_j$ | 2.41 | 2.41 |
| $P_e/P_a$ | 1.38 | 1.38 |
| $f_j/f_\infty$ | 0.769 | 0.769 |

Table 2. Wind tunnel test conditions.

| | Case 0 | Case 1 | Case 2 | Case 3 | Case 4 |
|---|---|---|---|---|---|
| $F_j$ [N] | 0 | 2.26 | 4.51 | 6.67 | 8.93 |
| $P_0$ [MPa] | 0 | 0.65 | 1.13 | 1.60 | 2.08 |
| $V_\infty$ [m/s] | 26.4 | 26.4 | 26.4 | 26.4 | 26.4 |
| $P_e/P_a$ | 0 | 0.43 | 0.75 | 1.06 | 1.38 |
| $f_j/f_\infty$ | 0 | 0.240 | 0.418 | 0.588 | 0.769 |

Credits: Nonaka et al. [27].

Figure 2.18: Nonaka's test conditions.

From the study, some essential key ideas can be deducted:

- The *momentum flux ratio* ($MFR = f_j/f_\infty$) is a meaningful parameter to consider when dealing with retro-propulsion, where

$$f_j = \rho_p v_e^2 \cdot A_e \qquad f_\infty = \rho_\infty v_\infty^2 \cdot A_{ref} \tag{2.5.1}$$

  are respectively the jet and the freestream momentum fluxes. This parameter must not be confused with the *aerodynamic thrust coefficient* ($C_T$, see Section 3.2): they both express the intensity of the nozzle jet against the counter-flow, but the first one takes into account just the momentum flux contribution, while the second one considers the entire thrust.

- Figure 2.19 shows that the higher the $MFR$, the lower the drag coefficient ($C_D$) and the pressure coefficients ($C_p$) on the vehicle base, and the higher the pressure coefficients on the sides of the vehicle. This means lower aerodynamic drag and base pressure, in exchange of higher side pressure.

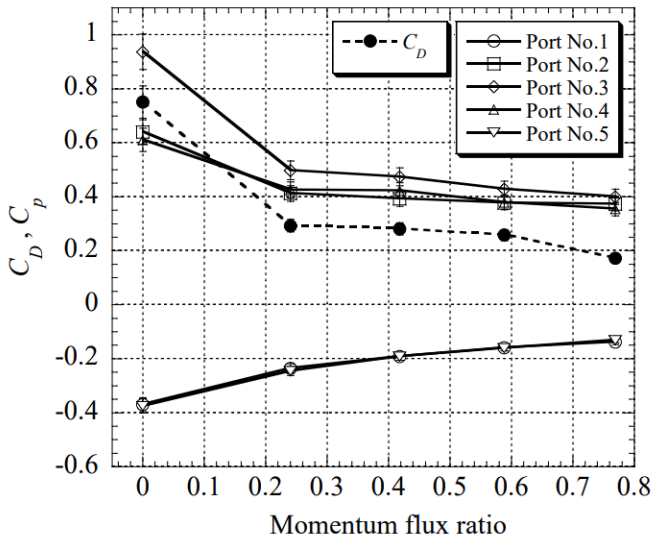


Credits: Nonaka et al. [27].

Figure 2.19: Drag coefficient and surface pressure on the vehicle.

- As expected from the theory [5], the flow re-attaches much sooner with the engine turned on.
- The interaction between jet and counter-flow generates a recirculation area. The distance from the nozzle of this stagnation point appears proportional to the intensity of the jet flow (fig. 2.20).

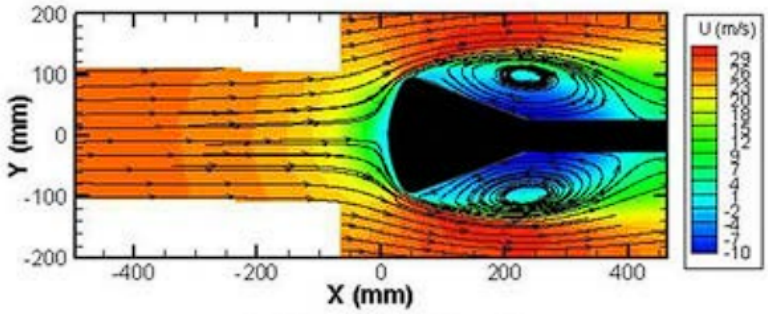


a) Case 0 : $f_f/f_\infty = 0$

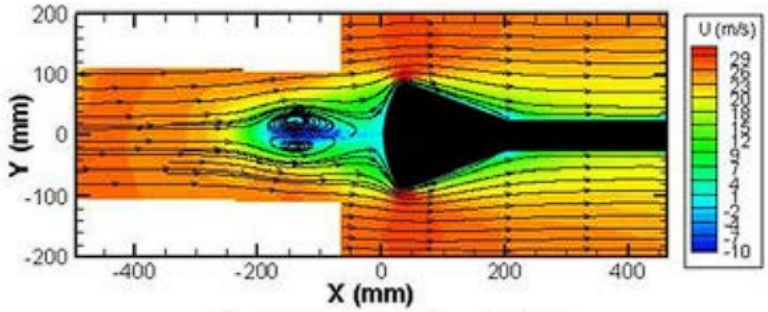


b) Case 1 : $f_f/f_\infty = 0.240$

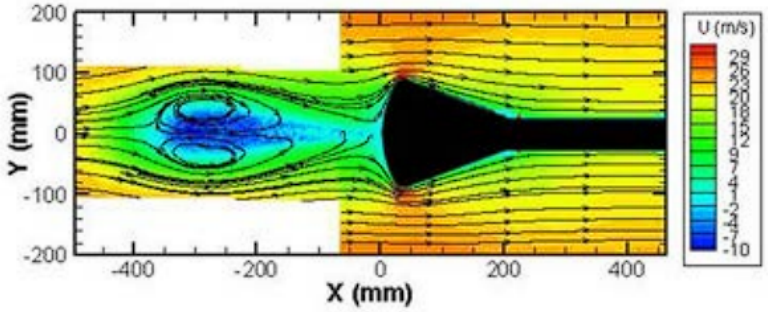


c) Case 4 : $f_f/f_\infty = 0.769$

hb

Credits: Nonaka et al. [27].

Figure 2.20: Velocity distribution using PIV measurement.

### 2.5.2 Cold-Flow Test-Bench for Study of Advanced Nozzles in Subsonic Counter-Flows

This thesis is part of the larger project underway at the Technische Universität Dresden (TUD) carried out by Scarlatella. The first experimental test campaign track and guidelines, valid also for the numerical study, are presented by Scarlatella et al. [7].

#### Wind Tunnel

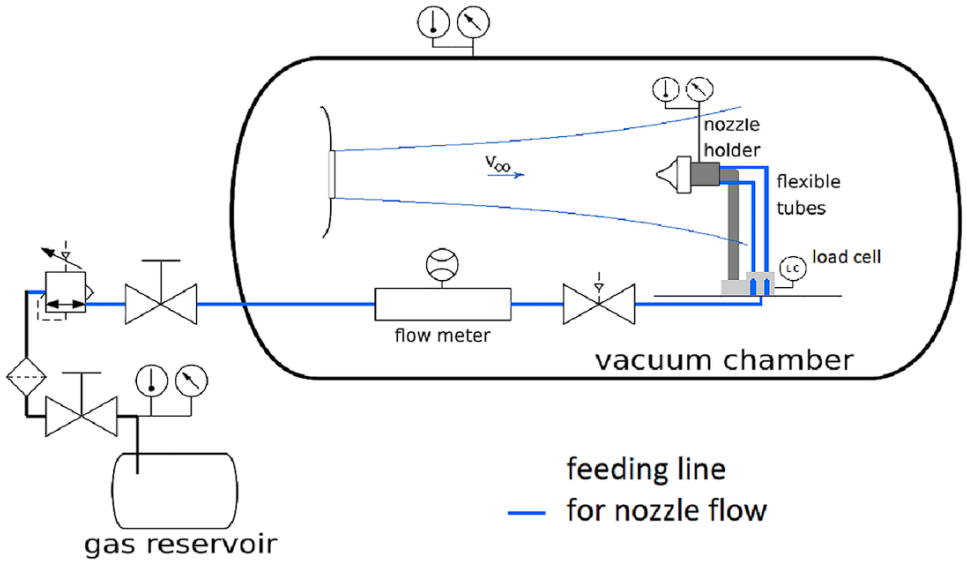


Credits: Scarlatella et al. [7].

Figure 2.21: Wind tunnel schematic.

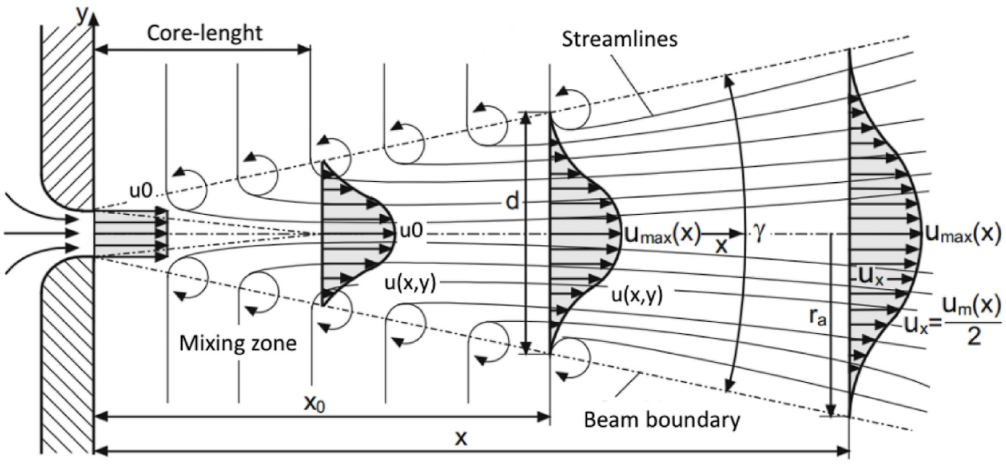


Credits: [29].

Figure 2.22: Conical flow generated by the wind tunnel.

The available experimental system consists of a vacuum wind tunnel, with a cylindrical aluminum vessel of 1200 $mm$ in diameter and 3400 $mm$ in length (fig. 2.21). A fan takes air from the chamber and pushes it via a short conduit into a stilling tank until the convergent nozzle (exit diameter of 100 $mm$), producing the free jet. The latter develops as a conical profile, characterized by a laminar stable core – where the velocity is almost constant and completely axial – and an external turbulent area – where the velocity progressively decreases and gains radial component moving far from the axis (fig. 2.22). Appropriate sensors consent to measure the ambient pressure ($p_a$) – which can be regulated in a range of 10000 - 101325 $Pa$ – and the freestream velocity ($u_\infty$).

Inside the chamber, an L-shaped cold-gas nozzle test bench is collocated on binaries, which allow to move it along the axis (1 d.o.f.), changing the distance from the origin of the counter-flow. At the top of the structure, a specific chamber holder (fig. 2.23) permits to mount the different 3D printed nozzles (bells and ACNs) and to adjust the angle of attack in steps of 5°, with a maximum swivel range of 180° [30].

On the back of the structure, a load cell measures the horizontal force, useful for evaluating thrust and drag. Other sensors placed on the workbench allow to determine chamber pressure ($p_0$) and temperature ($T_0$), and the mass flow ($\dot{m}_p$).

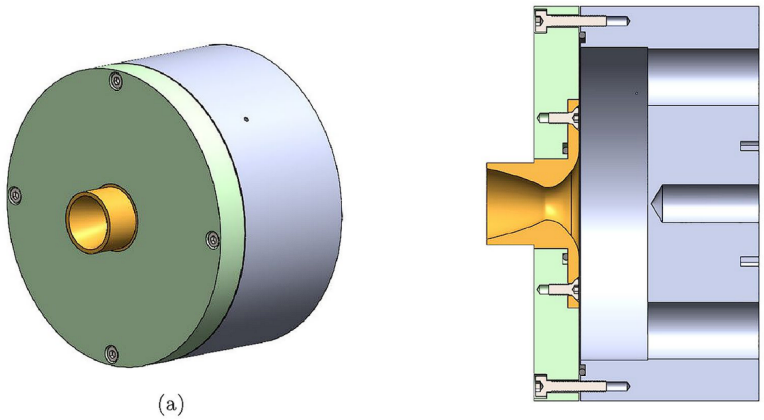

(a) (b)

Credits: Roßberg [30].

Figure 2.23: CAD model of the cold nozzle chamber (diameter of 106 $mm$), example of a configuration mounting a conventional bell nozzle: front (a) and side (b) views of the cold-flow chamber.

The purpose of this specific section is mainly to present the experimental apparatus in the TUD laboratory, and its utility for the goal of my numerical study. The design characteristics of the employed nozzles, as the actual operative chamber parameters, used in the experimental test (and consequently in the numerical one) are explored more in detail in section 4.1.

### Test bench improvements

During my own period of permanence at TUD, the experimental test bench went through a series of modifications to better reflect real-life applications and to perform more accurate measurements, enhancing rigidity and stability.

Scarlatella and Portolani [28] brought the following main improvements:

- An additional L-shaped aluminum support was installed in order to reduce bending and vibrations;

- In order to reach an Aspect Ratio closer to the real case of Falcon 9 (AR $\simeq$ 11), a 500 $mmm$ cylindrical body extension was incorporated through a supporting 3D printed ring. This allowed us to increase the $AR$ from 0.6 to 4.717, still far from the ideal one, but a great improvement considering the limitations and all the further alterations that a longer body would have required.

The final and complete test bench thus obtained is shown in Figure 2.24

Credits: Portolani [28].

Figure 2.24: Final test bench.

**Background-Oriented Schlieren**

Flow visualization in this study is facilitated by a Background-Oriented Schlieren (BOS) system, which is a non-intrusive technique that enables full-field visualization of fluid flows. It relies on a background pattern (e.g. a grid) as a reference for imaging: as the fluid passes through, it induces refractive index variations that distort the pattern. These distortions are captured by a camera, allowing for the generation of images representing the flow field. To record the flow behavior at the nozzle exit section, the camera is positioned in correspondence with the opposing glass windows in the vacuum chamber.

BOS images and videos will serve as a visual reference for the validation of the nozzle's jet flow topology obtained from the Ansys simulations (Section 8.2).

### 2.5.3 Numerical simulations of ACNs in Subsonic Counter-Flows

A first numerical study at TUD was recently carried out by Tapia Mancera [6] in his master thesis. The work provides an analysis of a Rao and an aerospike nozzles (respectively fig. 2.25 and 2.26) – both adapted to near vacuum (10670 $Pa$) – operating in the same four cases involved in this work that will be in-depth described in the next chapters: static burn on-/off-design, aerodynamic descent, and subsonic retro-propulsion. The contour images for the fourth case are shown in figures 2.27 and 2.28.

Tapia Mancera's work yielded a solid starting point for the implementation of the new simulations since the design parameters of the nozzles (established by Scarlatella in [7] and later presented in 4.1 a) and the experimental context are the same; in particular the aerospike nozzle was exactly identical. Moreover, his results – like flow behavior and numeric performance values – were used as a further verification reference. The interaction between jet and counter-flow establishes the expected stagnation point at a certain distance from the booster, which causes a drastic decrease of the base pressure at the expense of an increasing side pressure (as previously observed in Nonaka's et al. study [27]).

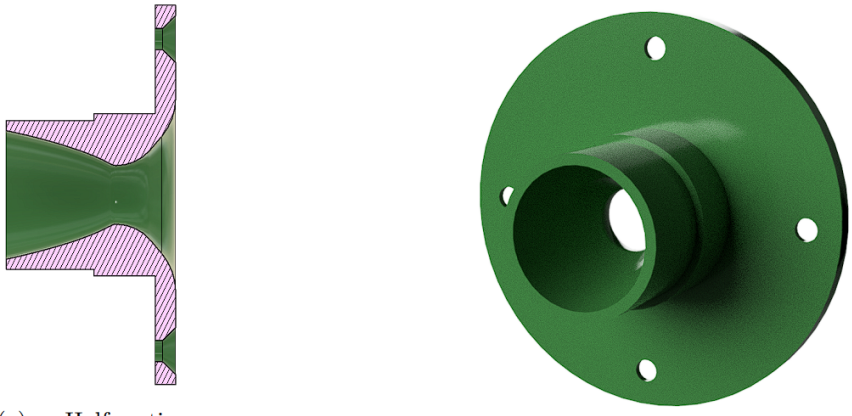

(a) Half-section view.

(b) Render.

Credits: Tapia Mancera [6].

Figure 2.25: Rao bell nozzle model (near-vacuum adaptation).

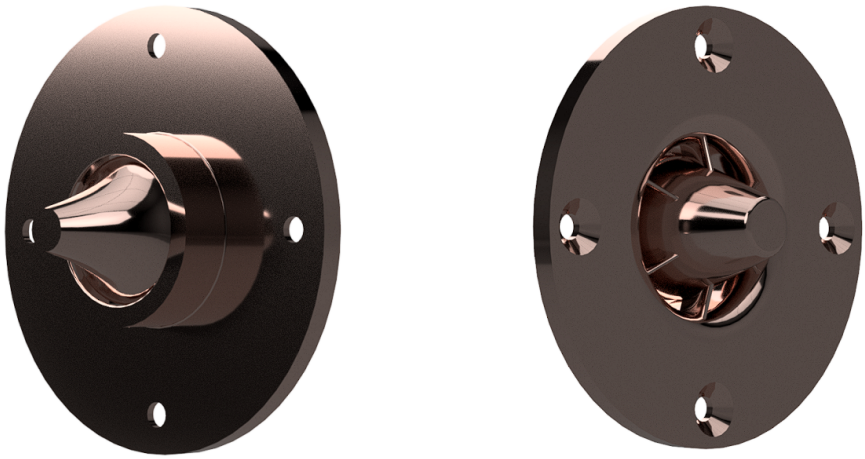

(a) Frontal view (render).

(b) Back view (render).

Credits: Tapia Mancera [6].

Figure 2.26: Aerospike nozzle model (near-vacuum adaptation).

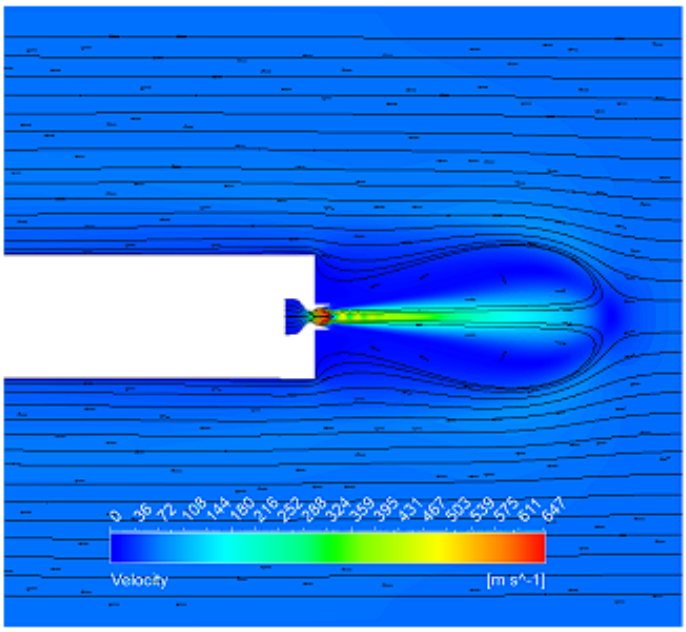


(a) Velocity magnitude contour, vector field and streamlines

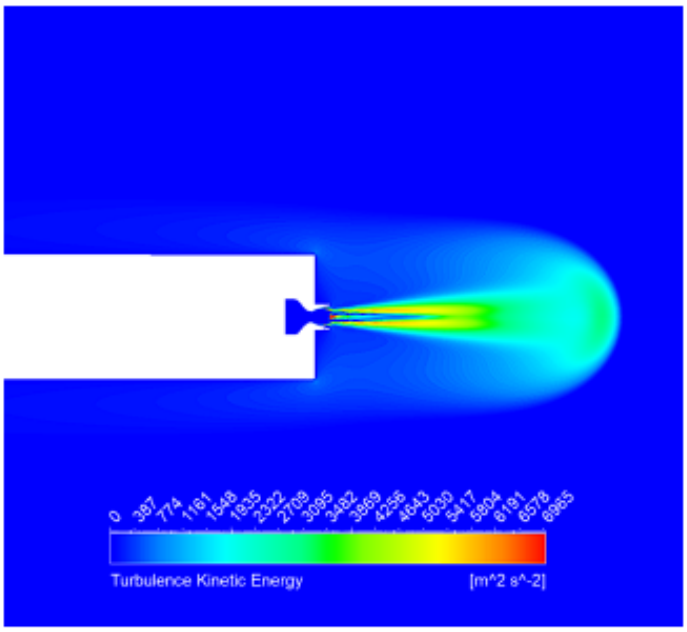


(b) Turbulent kinetic energy contour.

Credits: Tapia Mancera [6].

Figure 2.27: Contours over the booster – Rao nozzle configuration under sub-sonic retro-propulsion conditions.

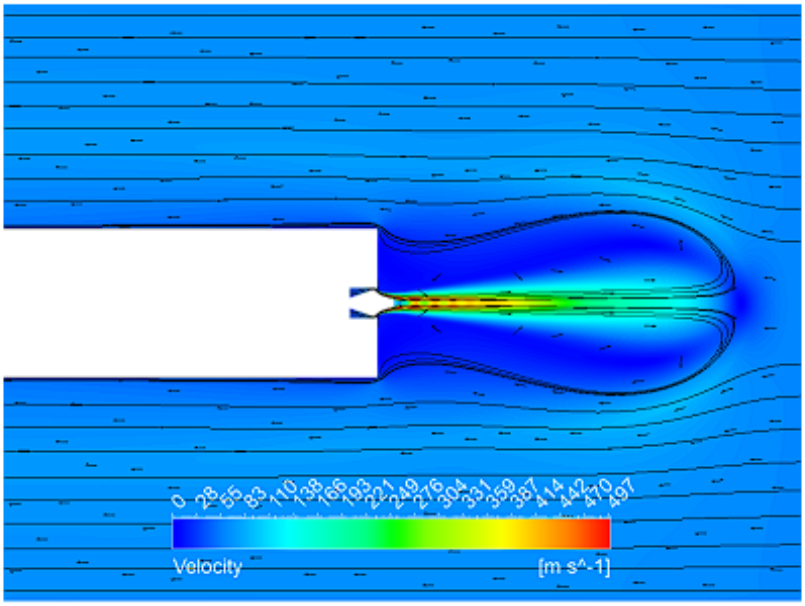


(a) Velocity magnitude contour, vector field and streamlines

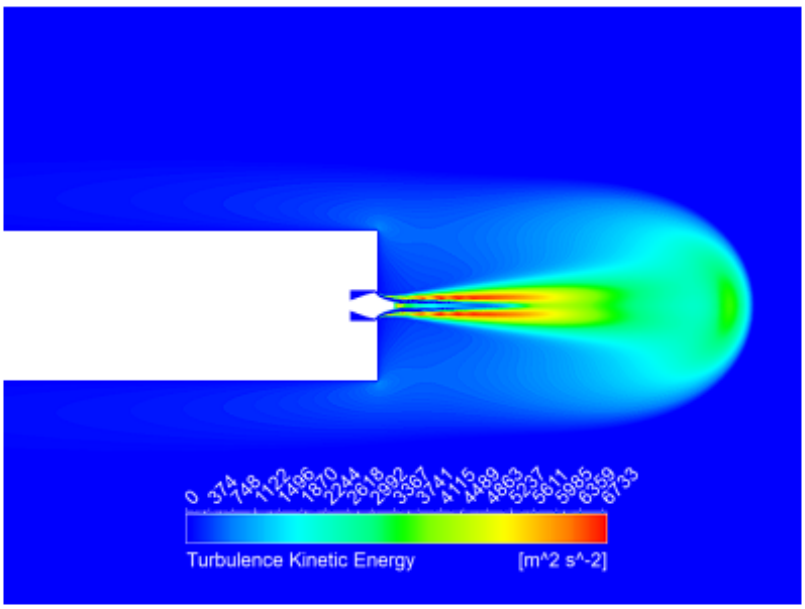


(b) Turbulent kinetic energy contour.

Credits: Tapia Mancera [6].

Figure 2.28: Contours over the booster – AS nozzle configuration under sub-sonic retro-propulsion conditions.

Figure 2.29 shows the most meaningful results, regarding the case of main interest (subsonic retro-propulsion), for Rao and aerospike nozzles.

| Parameter | Symbol | Sim. Value | | Unit |
|---|---|---|---|---|
| | | Conv. bell | Aerospike | |
| Nozzle pressure ratio | $p_0/p_a$ | 4,73 | 4,67 | - |
| Pressure expansion ratio | $p_E/p_a$ | 1,147 | 1,071 | - |
| Axial thrust | $F_x$ | -24,52 | -30,42 | N |
| Thrust coefficient | $C_F$ | 0,8698 | 1,13 | - |
| Specific impulse | $I_{sp}$ | 38,25 | 49,17 | s |

Credits: Tapia Mancera [6], modified image.

(a) Simulated nozzle performance values for the conventional bell and the aerospike nozzles.

| Parameter | Symbol | Sim. Value | | Unit |
|---|---|---|---|---|
| | | Conv. bell | Aerospike | |
| Freestream st. pressure | $p_\infty$ | 1,0127 | 1,0199 | bar |
| Freestream velocity | $u_\infty$ | -60 | -60 | m/s |
| Side pressure coefficient | $C_{ps}$ | 0,0098 | -0,3398 | - |
| Base pressure coefficient | $C_{pb}$ | 0,53 | 0,2993 | - |
| Side velocity | $u_s$ | -38 | -39 | m/s |
| Drag force | $D$ | -9,262 | -10,89 | N |
| Aero. drag coefficient | $C_D$ | 0,4752 | 0,5642 | - |
| Momentum flux ratio | $f_j/f_\infty$ | 0,5283 | 0,6836 | - |
| Aero. thrust coefficient | $C_T$ | 1,143 | 1,58 | - |
| Distance to stagnation point | $l_{st}$ | 259 | 258 | mm |

Credits: Tapia Mancera [6], modified image.

(b) Aerodynamic parameters of each nozzle configuration (*the drag values are incomplete and are only valuable as reference).

Figure 2.29: Tapia Mancera's case 4 results.

While no substantial aerodynamic differences seem to emerge among the nozzles, the AS - thanks to its attitude compensation capability – knocks out the bell nozzle in terms of engine performance, which is penalized by the induced normal shock that greatly reduces the propellant exit velocity.

The comparison reveals an advantage of 24% in axial thrust ($F_x$), 30% in nozzle thrust coefficient ($C_F$), 28.5% in specific impulse ($I_{sp}$), and a 38% in aerodynamic thrust coefficient ($C_T$). The latter should suggest a further stagnation point for the AS, but they sit more or less at the same distance. Tapia Mancera suggests that a possible explanation could be associated with the fact that the AS dissipates its momentum at a higher rate, due to the higher jet turbulence.

# *Chapter 3*

# *Methodology*

## 3.1 Simulation features

This thesis aims to create a CFD model to evaluate engine and aerodynamic performance of ACNs (Aerospike, Dual-Bell, and Expansion-Deflection) compared to conventional bell nozzles (Rao and Truncated-Ideal-Contour), in a subsonic counter-flow regime. The verified results should be comparable to those of the experimental campaign, allowing for validation of the simulations; it is therefore crucial that the data can be reproduced, ensuring its reliability and consistency. By undertaking this analysis, valuable insights can be gained regarding the relative merits and capabilities of the various nozzle designs.

The numerical study consists of 2D steady-state Reynolds-Averaged-Navier-Stokes (RANS) simulations, which have been run with double precision through the unlimited teaching license of ANSYS Fluent software on a personal computer (HP Omen 15-ax213ng: 16 GB RAM, Intel Core i7-7700HQ 4 x 2.8 - 3.8 GHz, NVIDIA GeForce GTX 1050 Ti Mobile - 4 GB VRAM graphic card).

#### Preliminary considerations

The whole simulation approach, from the domain geometry to the final setup, was oriented toward a compromised solution between the real-world application (with particular reference to the Falcon 9 recovery maneuver) and the experimental campaign parallelly executed by Scarlatella [7] and Portolani [28]. As such, compared to Tapia Mancera's work [6], the domains have been enlarged and the mesh has been refined. This was done – taking advantage of the unlimited license – in order to get more truthful AR values (body length up to 500 $mm$, as done on the experimental test bench), to reduce the direct influence of the boundary conditions.

On the other hand, the choice of counter-flow type – after many attempts and

reasoning – fell again on the more realistic uniform profile instead of the conical one present in the wind tunnel. The uniform flow allows to facilitate and improve the relevance of the pressure and flow re-attachment analysis on the booster side. The requirements and the implications of using the conical one are later discussed in Chapter 10, since they still constitute a potentially valuable analysis that is worth considering doing in the future.

Each specific methodology aspect (geometry, meshing, pre-analysis, set-up and solution) here anticipated is deepened in the following dedicated chapters.

### Simulation campaign

Each nozzle was tested in the four cases, whose conditions are shown in table 3.1:

Table 3.1: Simulated cases (* onD: on-design – offD: off-design).

| **Case** | **Description** | $NPR$ | $p_a$ $[Pa]$ | $v_\infty$ $[m/s]$ | $Re_\infty$ |
|---|---|---|---|---|---|
| 1 | OnD static burn | Bell: 13.852<br>ANCs: 45 | 34653.15<br>10670 | 0 | 0 |
| 2 | OffD (SLS) static burn | 4.74 | 101325 | 0 | 0 |
| 3 | Aerodynamic descent | 0 | 99156[1] | 60 | $\sim 400000$ |
| 4 | Retro-propulsion | 4.84 | 99156[1] | 60 | $\sim 400000$ |

[1] lower than case 2 since the presence of the counter flow implies a non-zero dynamic pressure that causes the static pressure to decrease

In particular, the cases are selected for the following purposes:

- Case 1: Verify the expected nozzle performance at design condition (optimal expansion);
- Case 2: Verify the expected nozzle performance at sea-level-standard (SLS) conditions, to have a reference without the counter flow for case 4;
- Case 3: Evaluate the aerodynamic performance of the vehicle subjected to the counter-flow, to have a reference with the engine turned off for case 4;
- Case 4: Complete subsonic retro-propulsion scenario.

### Verification criteria

The verification process dwells on two key aspects:

1. Correspondence of the performance with the expected theoretical values, coming from design parameters, hand calculations and previous literature;
2. Meeting of the desired convergence criteria for the simulation, which are:
   - All residual magnitudes below $10^{-5}$;

– Stability and monotonous convergence for at least 100 iterations of key parameters: *momentum thrust* ($f_j = \dot{m}_p v_e$) when the engine is turned on, and *drag coefficient* when the counter-flow is turned on ($C_D$).

**Validation criteria**

The engine performance of each nozzle was compared with the experimentally measured one, except for the dual-bell, for which unfortunately the available time was not enough in order to print and test it. Due to the different types of counter-flow, validation of cases 3 and 4 was not entirely possible: it will focus on qualitative aspects that could still bring meaningful insights to widen the knowledge about ACNs in subsonic counter-flow.

## 3.2 Data extrapolation and evaluation

Two typologies of results were collected:

- *contours* and *graphs* of a few key parameters – such as Mach number, velocity, turbulence kinetic energy (*tke*), and density gradient – obtained from CFD-post, useful to observe the flow-field and the phenomena in it contained (shock and expansion waves);
- *numerical values* obtained by implementing the desired equations at the appropriate locations of the domain; these equations are below illustrated for each specific context.

**Nozzles performance**

Generally, as anticipated in eq. 2.3.1, the *axial* thrust developed by a rocket nozzle can be calculated with the following equation [17]:

$$F_x = \dot{m} v_e + (p_e - p_a) A_e = C_F \cdot p_c \cdot A_t \tag{3.2.1}$$

where $\dot{m}$ is the mass flow, $p_e$ and $p_a$ are respectively the nozzle exit and the ambient pressures, $A_e$ is the cross-section area of the nozzle exit. This equation therefore considers the momentum and the exit pressure contributions, and constitutes a great approximation for most of the cases, however for the aerospike a special one has been implemented [31]:

$$F_x = [\dot{m} v_t cos(\theta) + (p_t - p_a) A_t cos(\theta)] + \int_{A_a} (p - p_a)\, dA + (p_{tr} - p_a) A_{tr} \tag{3.2.2}$$

where the first two terms between squared brackets represent the same momentum and pressure contribution shown in eq. 3.2.1, but this time the velocity and the exit pressure are measured at the annular nozzle throat around the larger base of the spike. Since the throat area is not oriented axially, the turning angle $\theta$ has to be taken into account (see figure 3.1). The third term summarizes the evolving

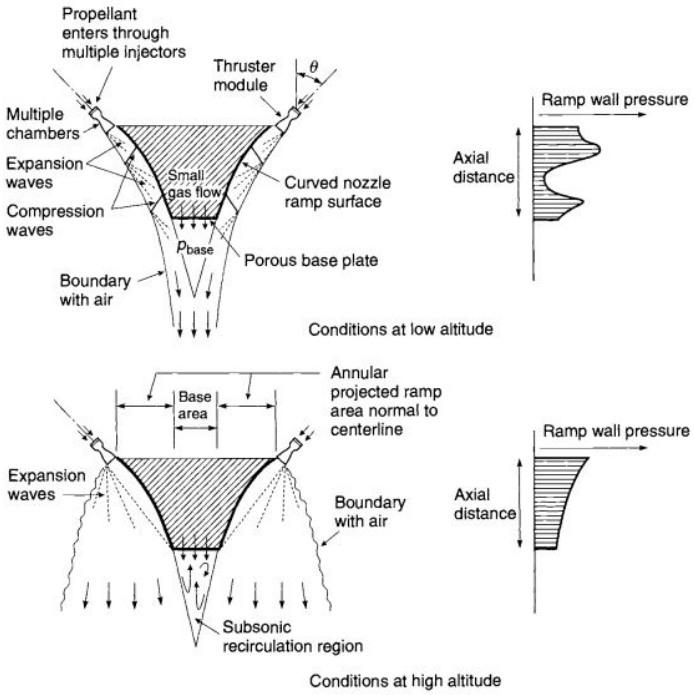


Credits: [32].

Figure 3.1: Aerospike functioning and pressure profiles.

pressure distribution contribution on the spike surface; the difference between the area-weighted and the ambient pressures is integrated over the projected spike area in the axial direction. Since the spike surface is a curve without constant inclination, in order to evaluate the equivalent angle, the MATLAB script shown in Appendix A is used. Finally, the fourth term represents the pressure-induced component at the spike truncation region.

Moreover, the *nozzle thrust coefficient* can be evaluated as follows:

$$C_F = C_{F\,opt} + \varepsilon \left( \frac{p_e}{p_c} - \frac{p_{amb}}{p_c} \right) = \frac{F_x}{p_c A_t} \tag{3.2.3}$$

where

$$C_{F\,opt} = \sqrt{\frac{2\gamma^2}{\gamma - 1} \left( \frac{2}{\gamma + 1} \right)^{(\gamma+1)/(\gamma-1)} \left[ 1 - \left( \frac{p_e}{p_c} \right)^{(\gamma-1)/\gamma} \right]} \tag{3.2.4}$$

represents the value of the coefficient in optimal adaptation conditions, while $p_c$ is the chamber pressure and $\varepsilon$ is the area expansion ratio.

Other important parameters to describe the nozzle performance are the *specific impulse*:

$$I_{sp} = \frac{F_x}{\dot{m} g} \tag{3.2.5}$$

and the *mass flow*:

$$\dot{m} = \frac{A_t p_c}{\sqrt{\gamma R T_0}} \left[ \gamma \left( \frac{2}{\gamma + 1} \right)^{\frac{\gamma+1}{2(\gamma-1)}} \right] \tag{3.2.6}$$

### Aerodynamic performance

The aerodynamic performance are estimated by measuring the *pressure coefficients*, the *drag* and *drag coefficients*. The first ones are obtained from eq. 3.2.7 [33]:

$$C_p = \frac{p - p_\infty}{q_\infty} \tag{3.2.7}$$

where

$$q_\infty = \frac{1}{2}\rho_\infty v_\infty^2 \tag{3.2.8}$$

is the freestream *dynamic pressure*. In particular, the $C_p$ are measured at 2/3 of the radius length on the booster base ($C_{p_b}$) and at one radius of distance from the base on the booster side ($C_{p_s}$), in order to have an indicator for each specific location.

The *drag* and the *drag coefficient* (eq. 3.2.9) are evaluated on the outer nozzle walls, and on the booster base and side.

$$C_D = \frac{D}{q_\infty A_{ref}} \tag{3.2.9}$$

### Retro-propulsion parameters

For what concern the retro-flow analysis, the two main parameters to examine are the *momentum flux ratio* [27]:

$$MFR = f_j/f_\infty = \frac{\rho_p v_e^2 A_e}{\rho_\infty v_\infty^2 A_{base}} = \frac{\dot{m} v_e}{2 q_\infty A_{base}} \tag{3.2.10}$$

and the *aerodynamic thrust coefficient* [34]:

$$C_T = \frac{F}{q_\infty A_{ref}} \tag{3.2.11}$$

which even if it acquires its maximum relevance in the study of supersonic retro-propulsion, it still provides valid information.

# *Chapter 4*

# *Problem specification and Pre-analysis*

This chapter is oriented to show the five nozzle specimens used for the simulations and a pre-analysis of the case studies. The nozzle design parameters, procedures and geometries, as the operative conditions of each scenario, and the expected analytical results for the engine's performance are presented.

## 4.1 Specific nozzles specimens design

The nozzle are mainly divided in two categories with different design parameters:

- Bell Nozzles (RAO and TIC) – near-SLS design point
- Advanced Nozzle Concepts (AS, DB and ED) – near-vacuum design point

It is relevant to acknowledge that the design of the mentioned nozzles falls beyond the scope of this thesis, as the presented models were mainly pre-existing [6, 30]. The only exception is the dual-bell, which was designed by Scarlatella through a set of data extrapolated from my CFD results.

### 4.1.1 Bell nozzles

The parabolic Rao and the Truncated-Ideal-Contour nozzles were developed based on the parameters shown in table 4.1. The operative design pressure is set at near-SLS conditions with $NPR$ of 13.852, which is based on the sea-level Merlin 1D ($\varepsilon$ = 16) [11] used on the first stage of Falcon 9. Thus, if referred to a $p_c$ of 480000 $Pa$, it corresponds to ca. 8 $km$ of altitude. In addition, a thrust range of 28-30 $N$ at SLS was required.

Table 4.1: Design parameters for bell nozzles (near SLS design point).

| **Parameter** | **Symbol** | **Value** | **Unit** |
|---|---|---|---|
| Nozzle pressure ratio | $NPR$ | 13.852 | - |
| Exit pressure | $p_e$ | 34653.15 | $Pa$ |
| Chamber total pressure | $p_c$ | 480000 | $Pa$ |
| Chamber total temperature | $T_0$ | 293.15 | $K$ |
| Isoentropic exponent | $\gamma$ | 1.4 | - |
| Specific gas constant (air) | $R$ | 287 | $J/kgK$ |
| Nozzle expansion ratio | $\varepsilon$ | 2.328 | - |
| Nozzle throat area | $A_t$ | 58.8 | $mm^2$ |
| Mass-flow | $\dot{m}$ | 66.8 | $g/s$ |
| Thrust (@SLS) | F | 28-30 | $N$ |

#### Rao parabolic nozzle

To design the first bell nozzle, the Rao parabolic approximation method (outlined by Huang and Huzelat [18]) was employed. The contour line of the bell nozzle, expressed in $(x, y, z)$ coordinates, was generated using a Python code developed by Tapia Mancera and accessible on Github [35]. The script requires input parameters from table 4.1, along with the divergent inflection angle, convergent half angle, ratio, and radius. Figure 4.1 depicts the final design and contour drawing of the nozzle (measurements are provided in millimeters).

This design was unfortunately later found to be inaccurate in terms of curvature angles and, consequently, length – it was therefore corrected before performing new experiments with it (the updated version of the Rao design can be found in Portolani's thesis [28]).

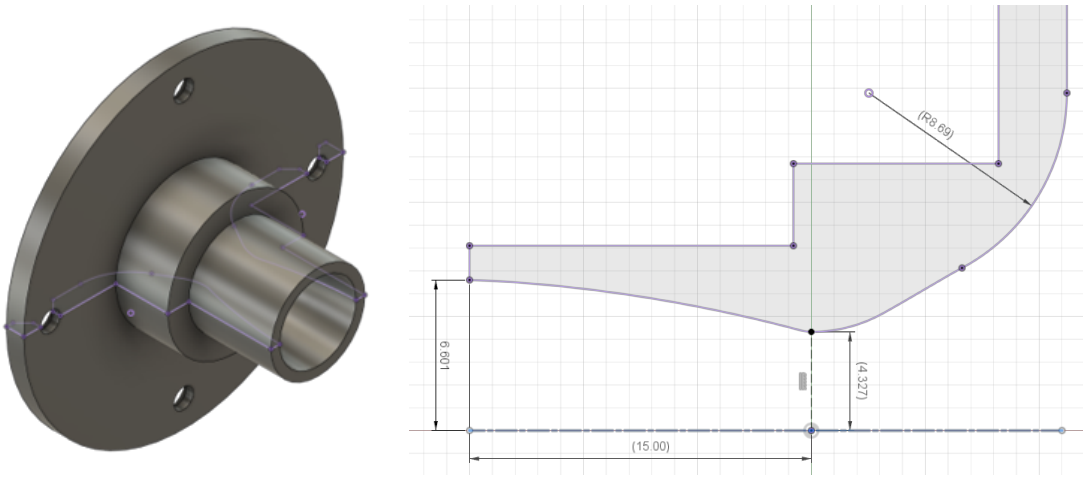


(a) 3D CAD model (b) Contour drawing

Figure 4.1: Rao parabolic bell nozzle design

### Truncated-Ideal-Contour nozzle

An Ideal-Contour nozzle was first designed by using an in-house design tool developed at TUD, which furnished a too-long contour (more than three times the conical one) with horizontal outlet tangent. The latter was thus truncated at a specific length aiming for the same exit angle of the adjusted version of the Rao (5.25°). Through a MATLAB code, this cut point was found to be at 34% of the IC, resulting in a nozzle 14% longer than the conical and 42% longer than the updated version of the Rao [28]. Nevertheless, it is also 34% shorter than Rao's version here used. Figure 4.2 shows the final design and contour drawing of the nozzle.

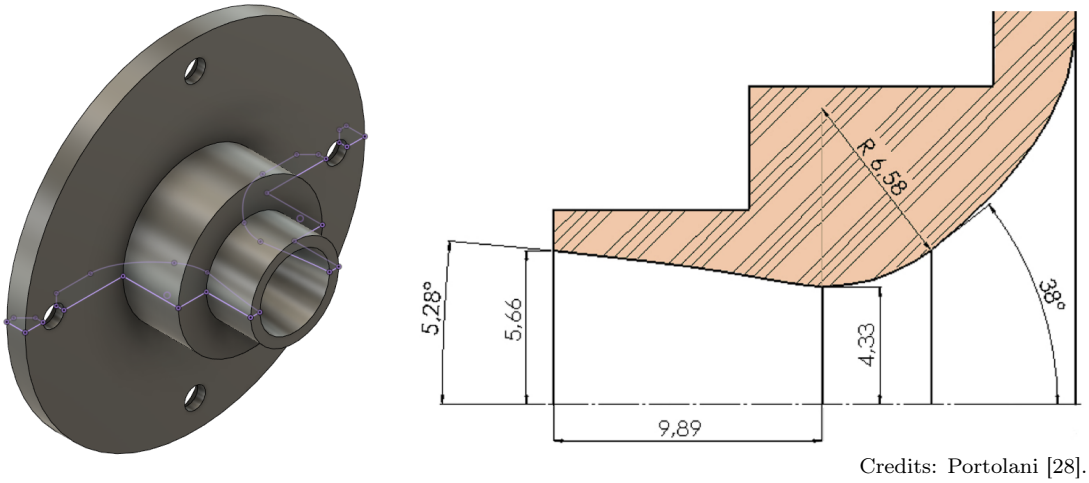


Credits: Portolani [28].

(a) 3D CAD model (b) Contour drawing

Figure 4.2: TIC bell nozzle design

### 4.1.2 Advanced Nozzle Concepts

Aerospike, dual-bell and expansion-deflection nozzles were instead designed for near-vacuum conditions (see table 4.2). More precisely a $NPR$ of 45 is considered (altitude $\simeq$ = 16 $km$, $p_e$ = 10670 $Pa$) and the expected thrust values lie around 40 $N$. The same design parameters were used to model another version of Rao parabolic bell nozzle, previously shown in fig. 2.25 which was already been simulated by Tapia Mancera [6]. This provides an additional reference for comparison of the alternative nozzles.

Table 4.2: Design parameters for ANCs (near vacuum design point).

| **Parameter** | **Symbol** | **Value** | **Unit** |
|---|---|---|---|
| Nozzle pressure ratio | $NPR$ | 45 | - |
| Exit pressure | $p_e$ | 10670 | $Pa$ |
| Chamber total pressure | $p_c$ | 480000 | $Pa$ |
| Chamber total temperature | $T_0$ | 293.15 | $K$ |
| Isoentropic exponent | $\gamma$ | 1.4 | - |
| Specific gas constant (air) | $R$ | 287 | $J/kgK$ |
| Nozzle expansion ratio | $\varepsilon$ | 4.82 | - |
| Nozzle throat area | $A_t$ | 58.8 | $mm^2$ |
| Mass-flow | $\dot{m}$ | 80 | $g/s$ |
| Thrust (@DP) | F | 40 | $N$ |

Credits: Scarlatella et al. [7].

#### Aerospike nozzle

The aerospike nozzle was designed through a Python code developed by M. Vernacchia [36] based on C.C. Lee's contouring method. In order to resemble the shape of Pangea Aerospace's Demo P1 aerospike [37], a 45% truncation was selected, as depicted in figure 4.3b. The program's graphical user interface (GUI) was populated with the relevant input parameters ($p_c$, $T_c$, $p_a$, $\gamma$, $R$, $\varepsilon$, and $F$), generating two separate '.csv' files containing the spike and shroud contours in the form of point coordinates, which were subsequently imported into Fusion 360, a CAD software, for further modeling. The spike and the shroud were then interconnected using NACA 0016 profiles as spokes to secure the spike in place (these are neglected in the CFD analysis) [6].

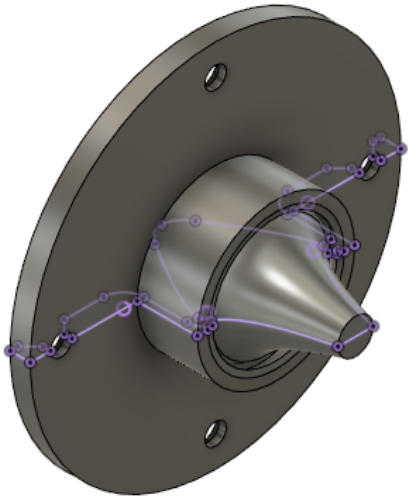

(a) 3D CAD model

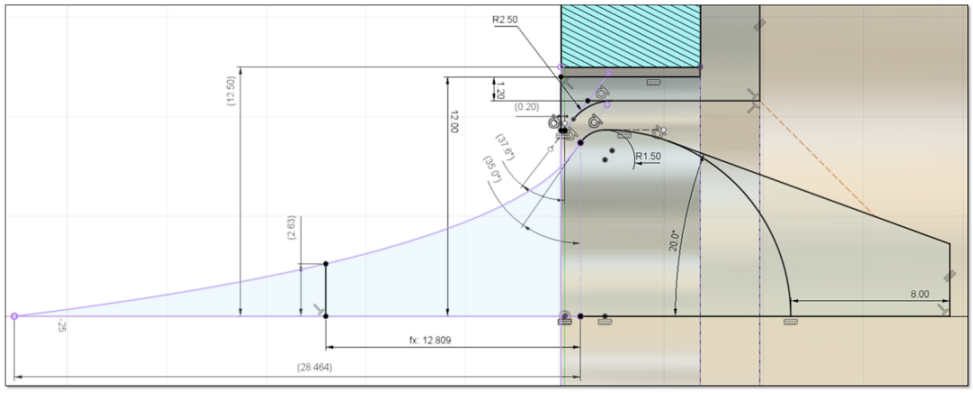


Credits: Tapia Mancera [6].

(b) Contour drawing

Figure 4.3: Aerospike nozzle design

### Dual-Bell nozzle

Differently from every other concept, the dual-bell nozzle is characterized by step-wise adaptability; as such, two different optimal points are selected. Since the nozzle is designed starting from the TIC, the first one is set to its same near-SLS condition, while the second one is the same as the other advanced concepts ($NPR = 45$).

Specifically, in order to generate the contour profile, a 2D simulation of the TIC nozzle operating at 10670 $Pa$ has been run. From the resulting post-processing results, I found the constant pressure points coordinates $(x, y)$ – at the ambient pressure itself – on the expanding plume (see fig. 4.4). These points were then extracted into a '.csv' file, interpolated, and manipulated to delete the undesired ones and regularize them at constant x intervals.

From this final coordinates file, Scarlatella created the actual 3D model of the nozzle. It was conceived to have the same exit radius as the Rao parabolic (9.5 $mm$) so that a direct comparison can highlight the main differences between the two.

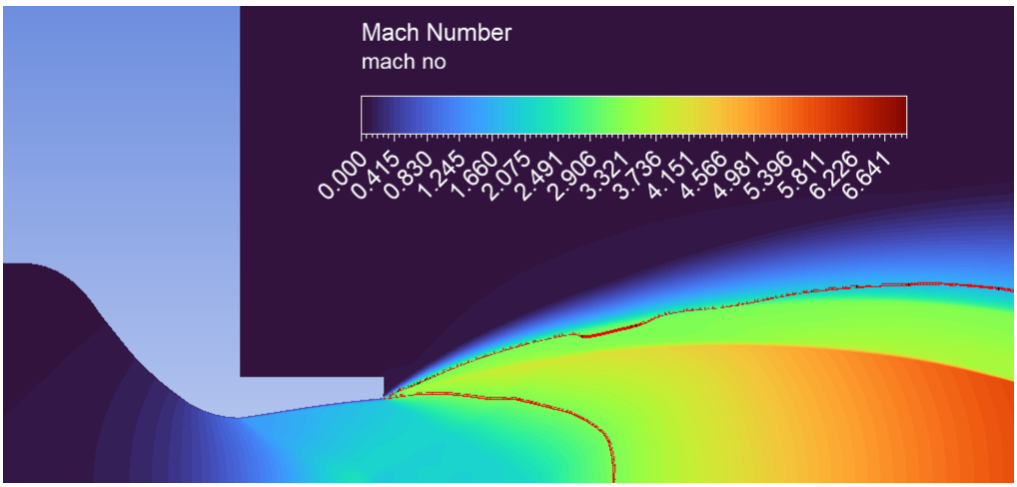


Figure 4.4: TIC pressure point extraction for DB design

The resulting 3D design and the contour drawing are shown in figure 4.5.

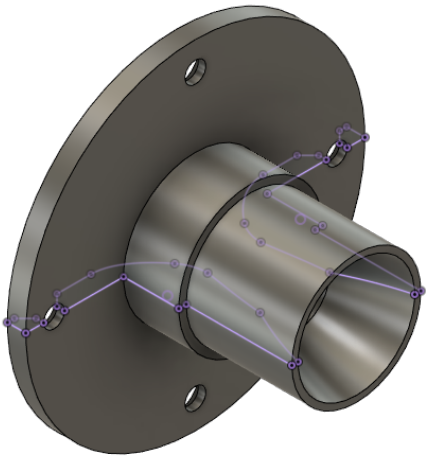

(a) 3D CAD model

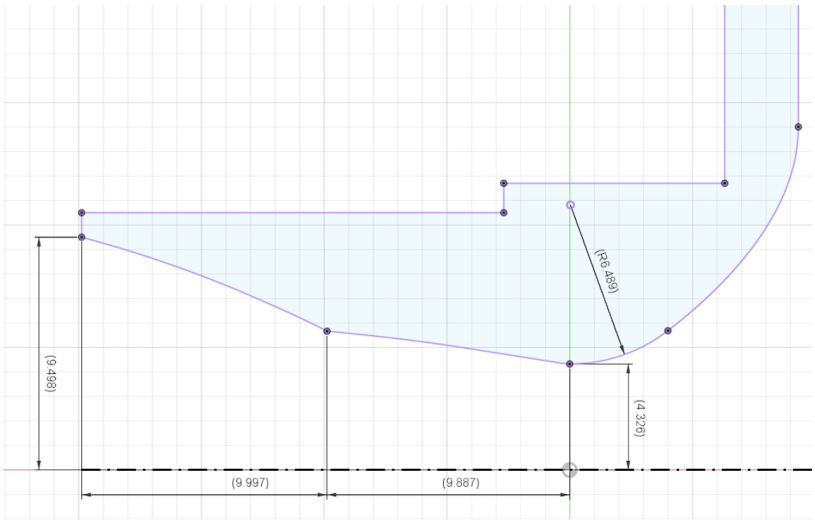


(b) Contour drawing

Figure 4.5: Dual-Bell nozzle design

### Expansion-Deflection nozzle

The ED nozzle in this study has been collaboratively designed with the University of Rome "Sapienza" using a self-developed MATLAB code that applies the Angelino method [38], using the parameters shown in 4.2. This method serves as an analytical approximation of the numerical Method of Characteristics (MoC), specifically tailored for isentropic expansion. By assuming straight characteristic lines, a constant specific heat ratio $\gamma$, and negligible friction effects, the Angelino method provides an idealized representation. However, it should be noted that this method is one-dimensional and does not account for flow divergence [39]. Figure 4.6 shows the resulting nozzle model and contour

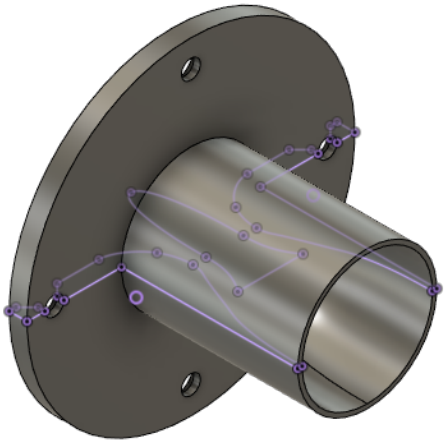

(a) 3D CAD model

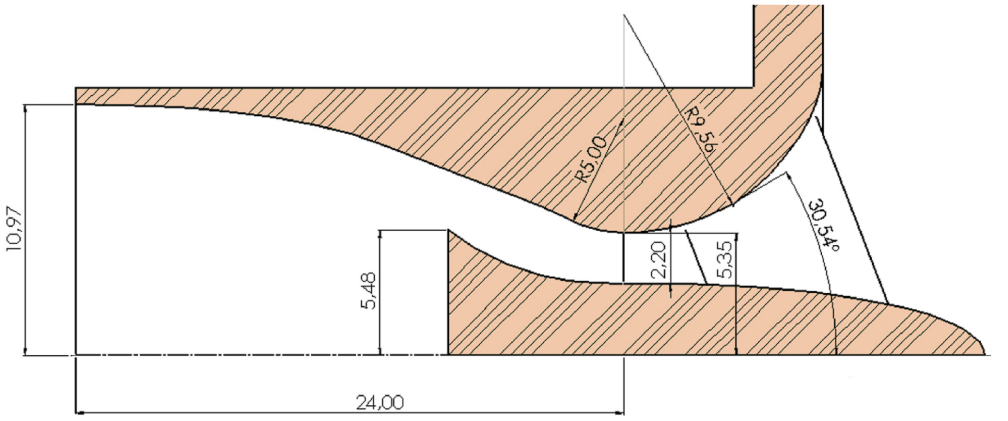


Credits: Portolani [28].

(b) Contour drawing

Figure 4.6: Expansion-Deflection nozzle design

## 4.2 Case studies pre-analysis

The four analyzed scenarios, anticipated in the previous chapter, are described here in more detail. Additionally, a pre-analysis of analytical results is presented, especially regarding the expected performance parameters of the nozzles.

Each case has its own specific operative and boundary conditions (see Chapter 6), but they all share the same following assumptions [6]:

- Cold-flow simulations with constant temperature of 293.15 $K$ (20°$C$) at every boundary condition;
- Axis-symmetrical flow: both the freestream and the thrust vectors are assumed to be aligned to the booster's axis of symmetry;
- Steady-state flow: the time-depending variables are averaged by RANS equations, so the flow behavior remains constant;
- Incompressible freestream flow: since its Mach number is below 0.3;
- Compressible nozzle jet flow: since its Mach number is above 0.3;
- Working fluid is viscous and considered as dry air with ideal gas hypothesis;
- No-slip condition on every wall.

### 4.2.1 Case 1: On-Design Static burn

Case 1 aims to verify the nozzle performance at their optimal adaptation conditions. A schematic representation of it is shown in figure 4.7.

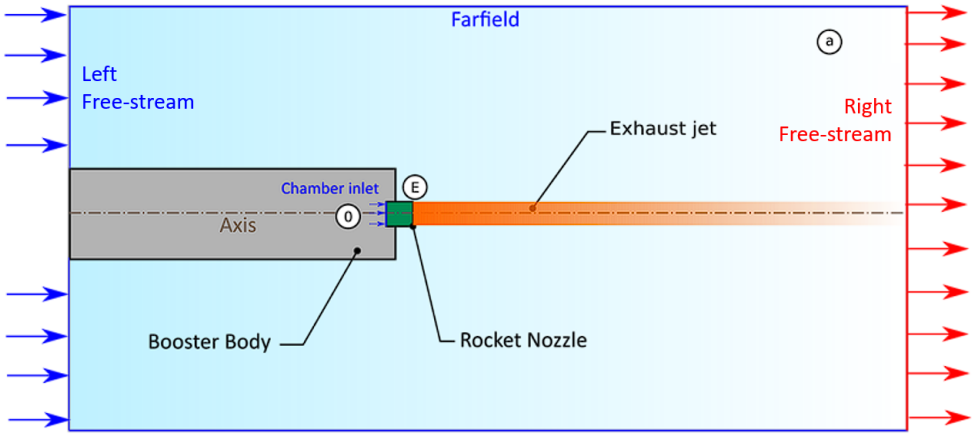


Credits: Tapia Mancera [6], modified image.

Figure 4.7: Static burn case scenario schematic.

Table 4.3 shows the analytical results obtained by using the equations presented in Section 3.2 and adopting isentropic conditions. Each nozzle is assumed to be perfectly adapted, considering the exit pressure $p_e$ to be perfectly equal to the ambient pressure $p_a$ (for the TIC nozzle, it's thus already expected to have some little losses, since the design pressure is referred to the IC).

Table 4.3: Case 1 expected nozzles performance.

| **Nozzle** | $NPR_{ref}$ | $p_a$ $[Pa]$ | $F_x$ $[N]$ | $C_F$ | $I_{sp}$ $[s]$ | $\dot{m}$ $[g/s]$ |
|---|---|---|---|---|---|---|
| RAO | 13.852 | 34653.15 | 37.16 | 1.317 | 56.87 | 66.63 |
| TIC | 13.852 | 34653.15 | 36.67 | 1.303 | 56.29 | 66.63 |
| AS | 45 | 10670 | 40.00 | 1.475 | 63.72 | 64.01 |
| DB | 45 | 10670 | 40 | 1.475 | 60.29 | 66.63 |
| ED[1] | 45 | 10670 | 44.66 | 1.582 | 68.32 | 66.63 |

[1] expected $M_e = 3.136$

### 4.2.2 Case 2: Off-design (SLS) Static burn

The overall setup of case 2 is almost identical to the first one (fig. 4.7), however this time the ambient pressure is set to sea-level-standard (SLS) conditions, meaning a $p_a = 101325\ Pa$. Its main purpose is to act as a reference for nozzle performance with case 4. Naturally, due to the high pressure, a certain over-expansion of the nozzle flow is expected. For the near-SLS bell nozzles and the dual-bell, at least some non-isentropic phenomena (such as compression waves or even normal shocks) should occur in proximity to the nozzle exit. Instead, the aerospike and the expansion-deflection are supposed to adapt to the new ambient conditions, resulting in pressure expansion ratios not far from 1. For this reason, optimal adaptation is assumed as a first approximation for the first one ($p_e = p_a$). For the ED a proper estimation of the off-design performance was not possible, due to the peculiar behavior and shaping of the nozzle.

The expected analytical results are shown in table 4.4; also here, for simplicity reasons, the flow is considered as isentropic. With respect to these data, some losses are therefore contemplated in the numerical results.

Table 4.4: Case 2 expected nozzles performance.

| **Nozzle** | $NPR_{ref}$ | $p_a$ $[Pa]$ | $F_x$ $[N]$ | $C_F$ | $I_{sp}$ $[s]$ | $\dot{m}$ $[g/s]$ |
|---|---|---|---|---|---|---|
| RAO | 4.737 | 101325 | 28.03 | 0.993 | 42.90 | 66.63 |
| TIC | 4.737 | 101325 | 30.06 | 1.065 | 46.00 | 66.63 |
| AS | 4.737 | 101325 | 29.42 | 1.085 | 46.87 | 64.01 |
| DB | 4.737 | 101325 | 30.06 | 1.065 | 45.18 | 66.63 |
| ED | 4.737 | 101325 | - | - | - | 66.63 |

### 4.2.3 Case 3: SLS Aerodynamic Performance

Case 3 is the only one where the engine is turned off (see figure 4.8), its purpose was, in fact, to furnish a reference of the undisturbed counter-flow for case 4. The counter-flow is a uniform velocity profile ($v_\infty = 60\ m/s$) axially oriented against the booster body; it simulates the freestream that the rocket's first stage faces during the final phase of the landing burn.

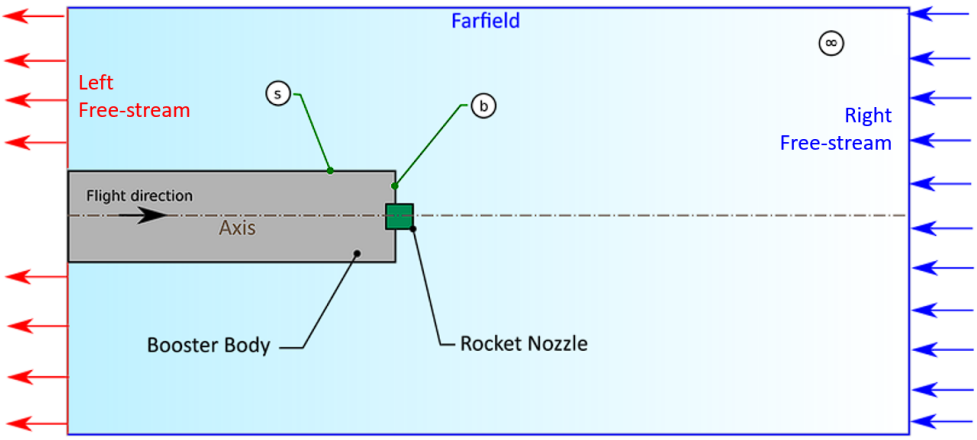


Credits: Tapia Mancera [6], modified image.

Figure 4.8: Aerodynamic descent case scenario schematic.

Since the flow is subsonic, it is able to smoothly adapt around the body, detaching while encountering the base edges and re-attaching further on the side. This behavior generates a lateral recirculation zone where the pressure coefficient $c_{ps}$ falls to negative values (as seen in Nonaka's experiment [27], which translates to an acceleration of the flow:

$$v = \sqrt{(1 - c_p)v_\infty^2} \tag{4.2.1}$$

where it's clear that $v$ increases if $c_p < 0$.

Moving far from the base, the $c_{ps}$ value should progressively get closer to 0. On the other hand, a stagnation zone on the base is expected, where $c_{pb}$ should be close to 1. In fact, from Bernoulli's equation:

$$p_b + q_b = p_\infty + q_\infty \tag{4.2.2}$$

where $v_b = 0$ (which implies $q_b = 0$), $q_\infty = \frac{1}{2}v_\infty\rho_\infty = 2169\ Pa$ and $p_\infty = 101325$ - $2169 = 99156\ Pa$; giving

$$c_{pb} = \frac{p_b - p_\infty}{q_\infty} = 1 \tag{4.2.3}$$

The direct collision of the counter-flow on the body generates a certain aerodynamic drag resistance (and $c_D$), which will be later evaluated on the wall surface. These values are incomplete since the top of the booster and wake effects are not considered for complexity reasons. Nevertheless, it is not strictly relevant to the

qualitative comparison between the nozzle, which is the main goal of this thesis, since it would constitute an equal contribution for all of them.

### 4.2.4 Case 4: Sub-sonic Retro-propulsion

Finally, case 4 basically consists of a combination of cases 2 and 3, where both the engine and the counter-flow are turned one. This retro-propulsion scenario is shown in figure 4.9:

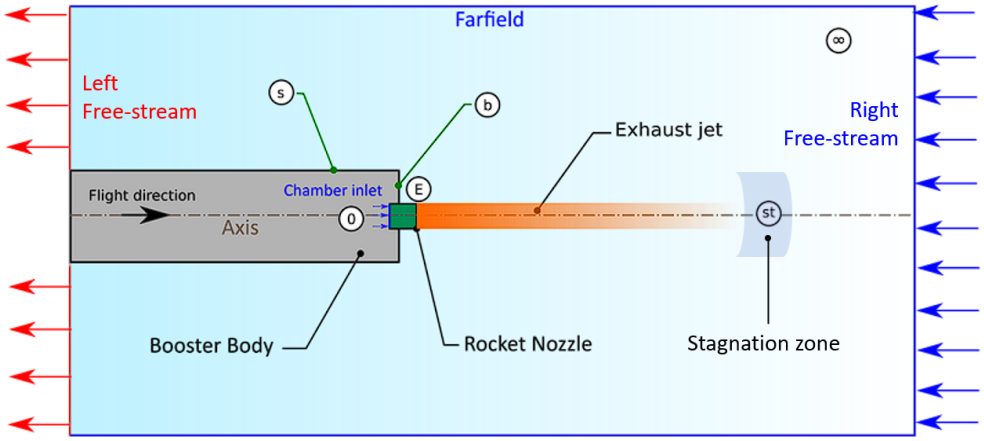


Credits: Tapia Mancera [6], modified image.

Figure 4.9: Retro-propulsion case scenario schematic.

According to Nonaka et al. [27], the presence of the dominant nozzle jet strongly affects the overall flow behavior of the resulting flow, since it breaks the freestream uniform profile causing it to bend around a recirculation area. This interaction drives the flow to an immediate re-attachment on the booster side, where therefore:

$$v_s = v_\infty \rightarrow q_s = q_\infty \rightarrow p_s = p_\infty \rightarrow c_{ps} = 0 \tag{4.2.4}$$

At the same time, a strong decrease in the booster base pressure ($c_{pb}$) is expected compared to case 3. In general, the vehicle should be accordingly subjected to a drastically inferior aerodynamic drag (meaning inferior $c_D$).

An additional secondary effect on the nozzle performance is predicted: since isentropic conditions are assumed, the non-zero dynamic pressure around the nozzle exit area (see fig. 2.20) implies a lower static pressure compared to case 2, where there was no counter-flow (need to change the simulation boundary conditions). Lower pressure mitigates the over-expansion phenomenon, leading to minor losses and slightly improved efficiency.

# *Chapter 5*

# *Domain definition and Meshing*

Starting from all the preliminary analysis, the previous considerations about the study approach, and the expected qualitative and quantitative results, the first real practical step in the CFD campaign is to develop the domain geometry for the simulations. Figure 5.1 shows a preview of the 2D axis-symmetrical design, including its subdivisions, which are fundamental for a proper meshing process. Each location needs in fact to be discretized differently depending on the desired resolution to solve specific phenomena (such as shock/expansion waves and boundary layers). The rocket body is always simplified as a cylinder with diameter $D = 106\ mm$.

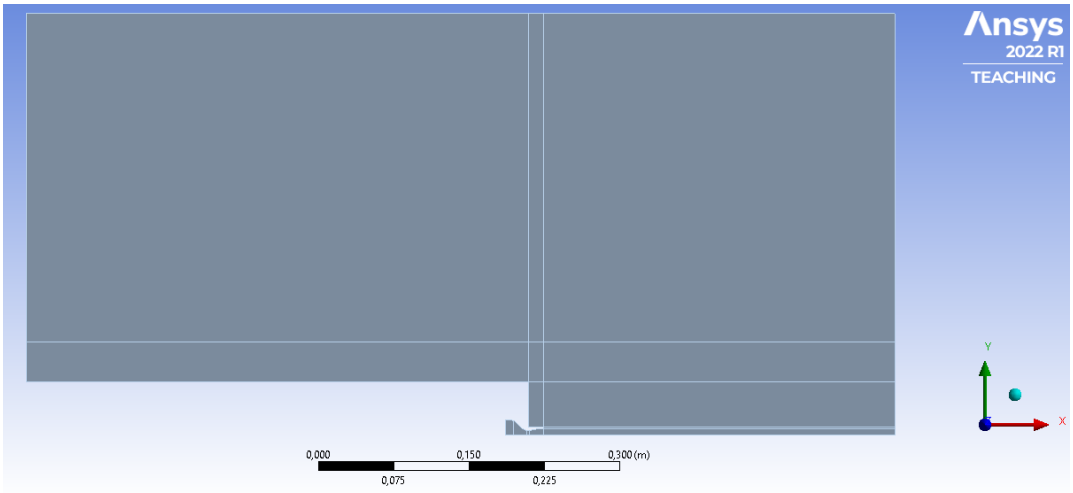


Figure 5.1: Domain subdivision (RAO example).

In particular, two different domains are envisaged. The first one is used for the static burn cases (1 and 2), while the second one for the other two cases, where the counter-flow is involved.

## 5.1 Static burn domain

In cases 1 and 2, attention is focused solely on the nozzle jet; thus the domain is designed to reduce computational cost while still ensuring a correct solution of flow phenomena. The result similarly follows the one used by Tapia Mancera [6], with a width of 5 $r$ from the symmetry axis and the booster length. However, the distance below the booster base was brought to 350 $mm$ measured from the nozzle exit, in order to mitigate the direct influence of the boundary condition and have a better correspondence with the other domain for the comparison.

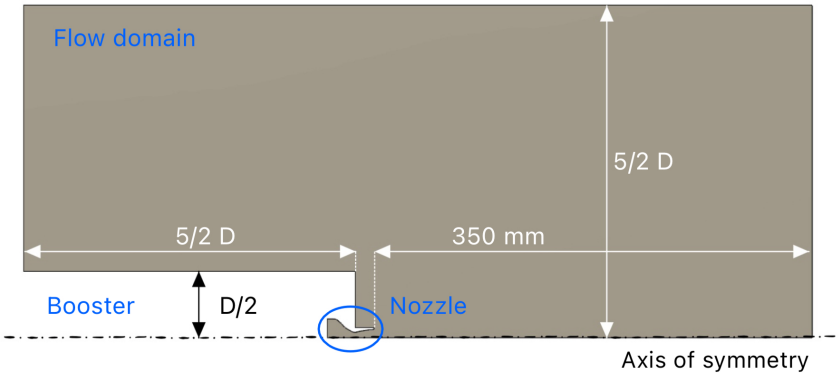


Figure 5.2: Domain dimensions for cases 1 and 2 (RAO example).

## 5.2 Counter-Flow domain

When the counter-flow is involved, it comes opportune to consider a larger domain able to more completely capture the interaction with and around the body, along with the consequent drag influence and evaluation. The increased distance between the nozzle and the right boundary allows here to better solve the stagnation point typical of case 4.

The domain was therefore modified in order to match the experimental conditions as much as possible: the length of the booster was brought to 500 $mm$, as the body extension implemented on the test-bench (fig. 2.24), and the distance from the axis was expanded to 580 $mm$, as the actual dimensions of the vacuum wind tunnel (see figure 5.3).

It's worth noticing that especially this last caution is not really relevant, since in the end a different counter-flow type was used. Nevertheless, it was previously used to study other counter-flow profiles (providing the motivations that brought to choose the uniform one), and it could be useful for further simulations that want to match the experimental environment (see Chapters 9 and 10).

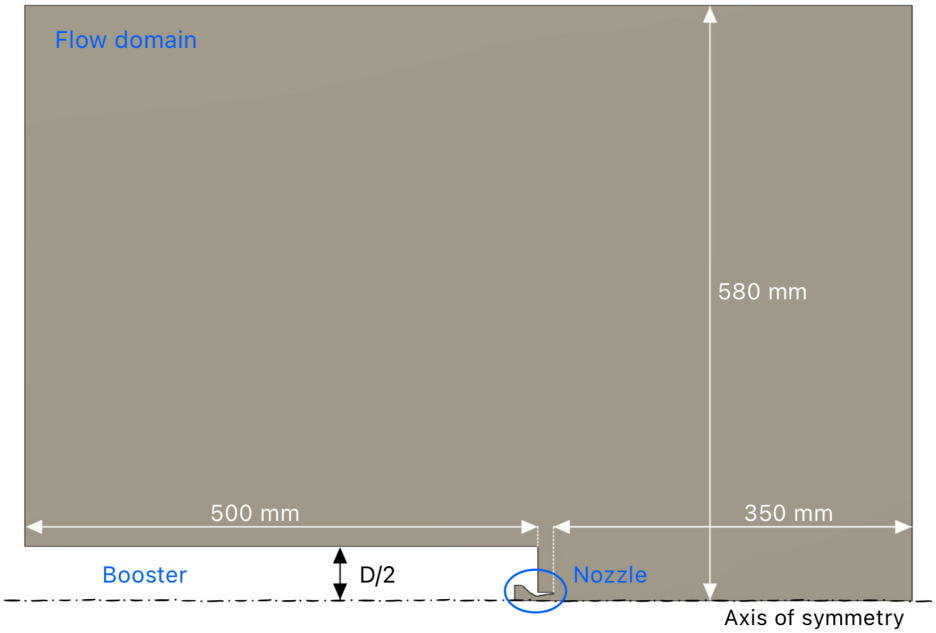


Figure 5.3: Domain dimensions for cases 3 and 4 (RAO example).

## 5.3 Mesh discretization

Since the simulation campaign consisted of four scenarios for five nozzles, for a total of twenty cases, not all the single discretization characteristics are reported here. Instead, the general meshing approach adopted for all of them is presented, with a couple of symbolic images for one of the specific nozzles as an example. Table 5.1 shows the target values set as universal requirements:

Table 5.1: Meshing target values for key parameters.

| **Parameter** | **Target value** | **Comments** |
|---|---|---|
| Avg. orthogonality | $> 0.98$ (w/ min ort. $> 0.5$) | Achieved (often $> 0.99$) |
| Avg. skewness | $< 0.05$ | Highly achieved ($\sim 0.01$) |
| Avg. AR[1] | $< 10$ (w/ max AR $< 50$) | Achieved (high values only in the boundary layers or in non-interest areas) |
| y+ | $< 5$ (as close to 1 as possible) | Achieved (w/ particular attention in specific areas)[2] |
| Number of cells | $> 500$k ($> 1000$k for case 4) | Almost always achieved[3] |

[1] aspect ratio
[2] DB nozzle step area
[3] convergence issues for bell nozzle with high number of cells

The main monitored quality parameters were the average orthogonality, average

skewness, and average aspect ratio; for which satisfactory standards were achieved. Moreover, a minimum number of 500k cells was aimed for the first three cases, doubled for the fourth one (since it needs a higher resolution both for the nozzle and the booster sides areas). Finally, in order to solve the boundary layers, the y+ value was checked to be lower than 5, which is still an acceptable upper limit for $k$-$\omega$ SST simulations [23]. The value was preliminarily monitored in this meshing phase using an online calculator to evaluate the expected size of the boundary layer [40], and later visualized in the post-processing phase to ensure it. The y+ value was particularly refined in specific contexts, such as the passage area from one design point to the other inside the dual-bell nozzle, where the target value was 1.5.

The discretization was not faced with the goal of immediately reaching the desired requirements: it is in fact common practice to divide the process into multiple phases or iterations for several reasons. Firstly, an initial rough simulation with an approximate mesh provided a preliminary evaluation of flow performance or key features, allowing for quick identification of issues and initial modifications associated with a sustainable computational cost. Secondly, a manual refinement of the mesh in a later stage optimized its quality and resolution, leading to more accurate results. This method offers iterative analysis and feedback, guiding the mesh refinement process and enhancing the resolution of flow characteristics of interest. In general, this multi-phase approach in CFD simulations combines efficiency, cost reduction, and improved accuracy [22].

In any case, the final result consisted of a structured mesh of quadrilateral elements, generated by applying to every edge an appropriate number of subdivisions.

### Cases 1 and 2 mesh (static burn)

In cases 1 and 2, the only zone of interest is the nozzle and its plume, as shown in figure 5.4. Hence, the mesh was there especially refined, saving complexity in the rest of the domain.

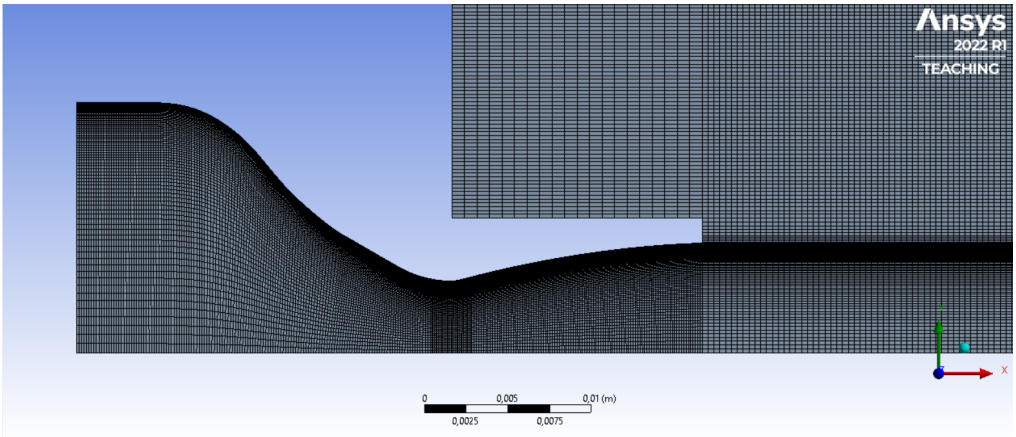


Figure 5.4: Nozzle mesh discretization for cases 1 and 2 (RAO example).

### Case 3 mesh (aerodynamic performance)

On the other hand, for case 3 the focus was on the domain around the booster, saving on the nozzle that was turned off. Figure 5.5 shows an overall view of the domain discretization.

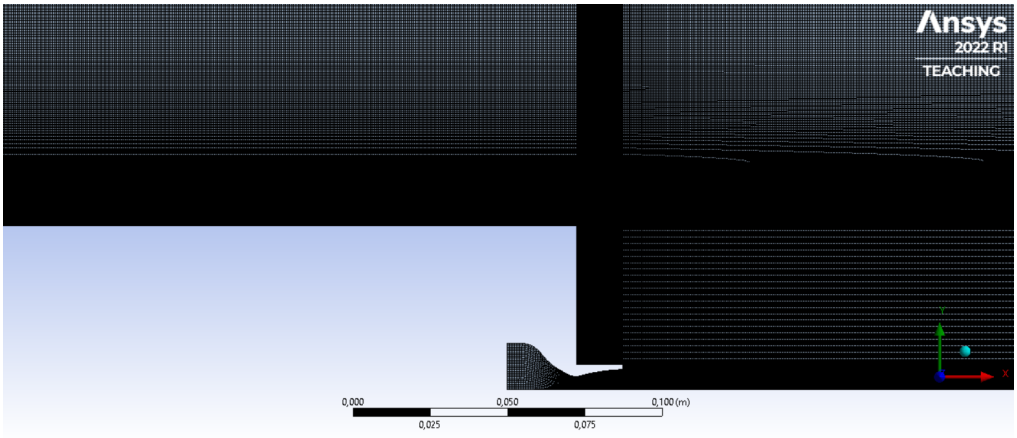


Figure 5.5: Domain mesh discretization for case 3 (RAO example).

### Case 4 mesh (retro-propulsion)

Case 4 mesh, as a combination of the previous ones, was equally refined in both the nozzle and the fluid domain around the booster. This obviously implied a substantially higher number of cells, which translates into increased complexity and computational cost. Figure 5.6 shows such a very dense domain discretization.

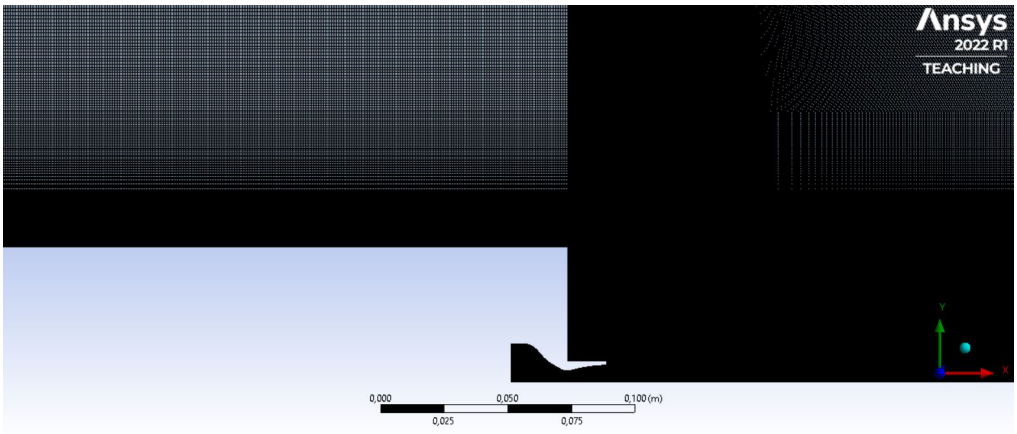


Figure 5.6: Domain mesh discretization for case 4 (RAO example).

# *Chapter 6*

# *Model Setup and Solution*

Before actually being able to run the simulation, it comes vital to arrange the proper setup. First of all, some key simulation properties were equally fixed for all twenty cases (same ones adopted by Tapia Mancera [6] since they were already proven to work well for this kind of scenario, and in order to be able to compare them more consistently):

- Energy equations are activated;
- Working fluid set to dry air (ideal gas with Sutherland-type viscosity);
- Turbulence model is $k$-$\omega$ SST model;
- Initial temperature condition set to 293.15 $K$;
- Initialisation with hybrid method, followed by a full-multi-grid (FMG) initialization method;
- Solver type is pressure-based, steady, and axisymmetric;
- Solver methods set to second order, with higher order term relaxation ticked (at 0,25 overall variables).

Only occasionally, some minor adjustments were made (like starting the solution with a first-order method or modifying the higher-order term relaxation value).

Then, for each case, the boundary conditions shown in 6.1 were set. Booster sides, base, and nozzle walls were always set to no-slip "wall" boundary type, as naturally the axis of symmetry was always the same. The other four boundaries were instead different case by case; they are presented in detail in the following sections.

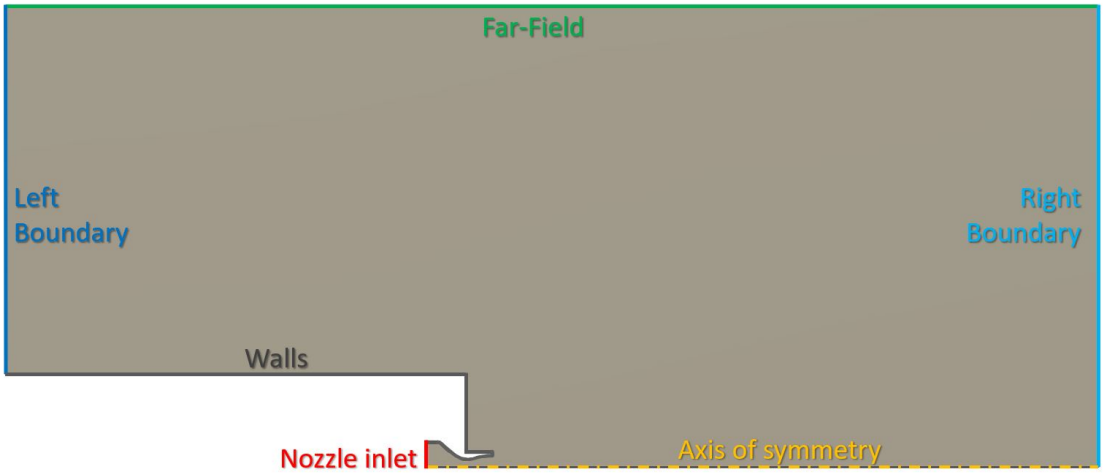


Figure 6.1: Domain boundaries labels.

## 6.1 Case 1 Setup

In case 1, the nozzle engine is activated, so at that location a pressure inlet with the cold chamber pressure is selected. The counter-flow is turned off, so the left and right boundaries only establish the ambient pressure conditions. Finally – since the nozzle flow is expected to create a light suction effect towards the positive "$x$" direction, and in order to facilitate the solver providing an overall direction of the flowfield – the far-filed is set to velocity inlet of 10 $m/s$. Tables 6.1 and 6.2 show these boundary conditions for the two groups of nozzles with different design points.

Table 6.1: Case 1 boundary conditions for bell nozzles (near SLS design point).

| Boundary **label** | Boundary **type** | **Key parameter** | **Value** |
|---|---|---|---|
| Nozzle inlet | Pressure inlet | Gauge pressure | 480000 $Pa$ |
| Right b. | Pressure outlet | Gauge pressure | 34653.15 $Pa$ |
| Left b. | Pressure inlet | Gauge pressure | 34653.15 $Pa$ |
| Far-field | Velocity inlet | Axial velocity | +10 $m/s$ |

Table 6.2: Case 1 boundary conditions for ANCs (near vacuum design point).

| Boundary **label** | Boundary **type** | **Key parameter** | **Value** |
|---|---|---|---|
| Nozzle inlet | Pressure inlet | Gauge pressure | 480000 $Pa$ |
| Right b. | Pressure outlet | Gauge pressure | 10670 $Pa$ |
| Left b. | Pressure inlet | Gauge pressure | 10670 $Pa$ |
| Far-field | Velocity inlet | Axial velocity | +10 $m/s$ |

## 6.2 Case 2 Setup

Case 2 setup is almost identical to case 1: the same ascertainments about the boundary conditions remain valid (shown in table 6.3).

Table 6.3: Case 2 boundary conditions.

| Boundary **label** | Boundary **type** | **Key parameter** | **Value** |
|---|---|---|---|
| Nozzle inlet | Pressure inlet | Gauge pressure | 480000 $Pa$ |
| Right b. | Pressure outlet | Gauge pressure | 101325 $Pa$ |
| Left b. | Pressure inlet | Gauge pressure | 101325 $Pa$ |
| Far-field | Velocity inlet | Axial velocity | +10 $m/s$ |

## 6.3 Case 3 Setup

In case 3, the nozzle is turned off, while the counter-flow is turned on. This is enough to impact every boundary condition, since the only similarity with case 2 in the ambient pressure is also affected by the dynamic pressure of the counter-flow itself. The nozzle inlet is now considered a wall, while the fluid domain edges are set in order to resemble a uniform counter-flow investing the vehicle at 60 $m/s$ in the negative $x$ direction. Table 6.4 shows a summary of these boundary conditions.

Table 6.4: Case 3 boundary conditions.

| Boundary **label** | Boundary **type** | **Key parameter** | **Value** |
|---|---|---|---|
| Nozzle inlet | Wall | - | - |
| Right b. | Velocity inlet | Axial velocity | -60 $m/s$ |
| Left b. | Pressure outlet | Gauge pressure | 99156 $Pa$ |
| Far-field | Velocity inlet | Axial velocity | -60 $m/s$ |

## 6.4 Case 4 Setup

Finally, case 4 is nothing more than case 3 with the nozzle engine on. The nozzle inlet is therefore changed back to a pressure inlet of 480 $kPa$. Table 6.5 shows a summary of these boundary conditions.

Table 6.5: Case 4 boundary conditions.

| Boundary **label** | Boundary **type** | **Key parameter** | **Value** |
|---|---|---|---|
| Nozzle inlet | Pressure inlet | Gauge pressure | 480000 $Pa$ |
| Right b. | Velocity inlet | Axial Velocity | -60 $m/s$ |
| Left b. | Pressure outlet | Gauge pressure | 99156 $Pa$ |
| Far-field | Velocity inlet | Axial Velocity | -60 $m/s$ |

# *Chapter 7*

# *Numerical results and Post-processing*

This chapter presents all the significant results obtained from the simulations of each case. It includes tables gathering the values of all the calculated relevant parameters – directly obtained from the *reports* in *Ansys Fluent*, where I've implemented the formulas explained in Section 3.2 – as the images collected during the post-processing; in particular:

- Case 1 and 2 (static burns) – Mach contours with focus on the nozzle;
- Case 3 and 4 (aerodynamic descent) – Velocity and Turbulence Kinetic Energy ($tke$) contours, to highlight the interaction of/with the counter-flow.

## 7.1 Case 1 results – On-Design static burn

This case is meant to evaluate the performance of the nozzle at its design operative conditions; as such, the latter are shown in table 7.1. Note, once again, that bell nozzles are designed for near-SLS, while ACNs for near-vacuum.

The data show similar values among both the bell nozzles (around 36 $N$) and the ACNs (around 39 $N$), which perform better, with also higher values of the exit Mach number. TIC nozzle is slightly less efficient than the RAO, due to the truncation that automatically modifies its true design pressure (34653.15 $Pa$ are referred to the IC) – this is clearly notable from the under-expansion implied by the high value of pressure expansion ratio ($p_e/p_a$), which is above 1.

Between the ACNs, the AS stands out in terms of $C_F$ and $I_{sp}$, still closely followed by the ED – which presents an odd over-expansion due to its peculiar shaping that would require more investigation – and the DB (which actually behaves well for being an early version designed pretty quickly).

Table 7.1: Case 1 CFD nozzles performance.

| **Nozzle** | $p_a$ $[Pa]$ | $F_x$ $[N]$ | $C_F$ | $I_{sp}$ $[s]$ | $NPR_{sim}$ | $p_e/p_a$ | $\dot{m}$ $[g/s]$ | $M_e$ |
|---|---|---|---|---|---|---|---|---|
| RAO | 34653.15 | 36.16 | 1.284 | 56.43 | 13.83 | 1.015 | 65.32 | 2,32 |
| TIC | 34653.15 | 36.04 | 1.279 | 55.99 | 13.83 | 1.730 | 65.61 | 1.99 |
| AS | 10670 | 39.18 | 1.457 | 63.49 | 44.67 | 1.039 | 62.91 | 3.08 |
| DB | 10670 | 38.96 | 1.383 | 60.29 | 44.91 | 1.156 | 65.88 | 3.06 |
| ED | 10670 | 39.25 | 1.393 | 60.74 | 44.90 | 0.789 | 65.88 | 3.12 |

Following, the Mach number contours of each nozzle are shown, where it's possible to distinguish shock and expansion waves of the exhaust gasses.

### Rao

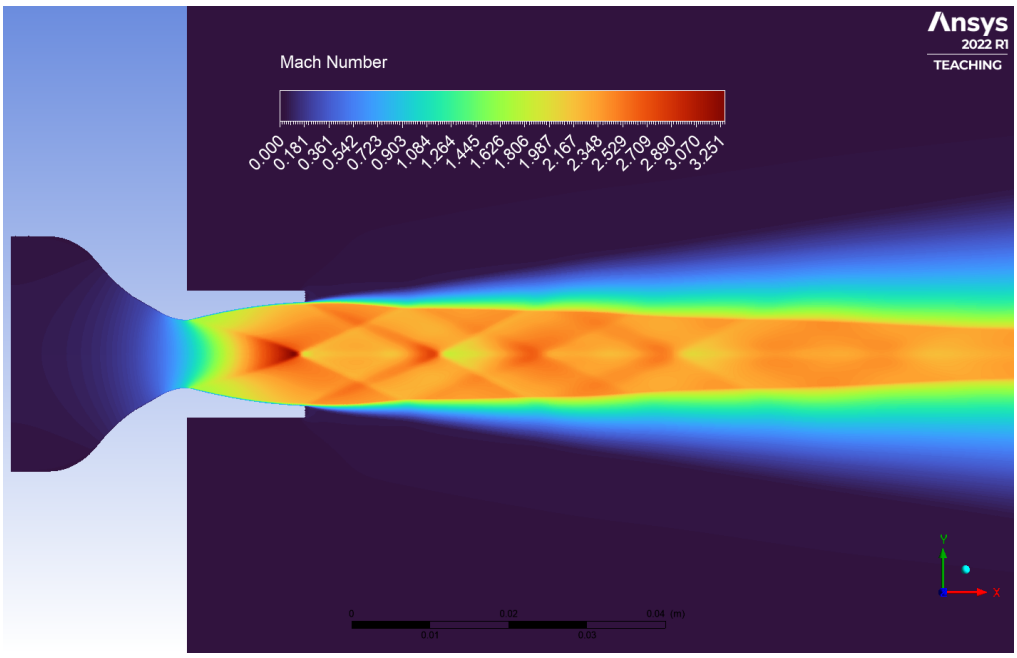


Figure 7.1: RAO case 1 – nozzle Mach number contour.

### Truncated-Ideal-Contour

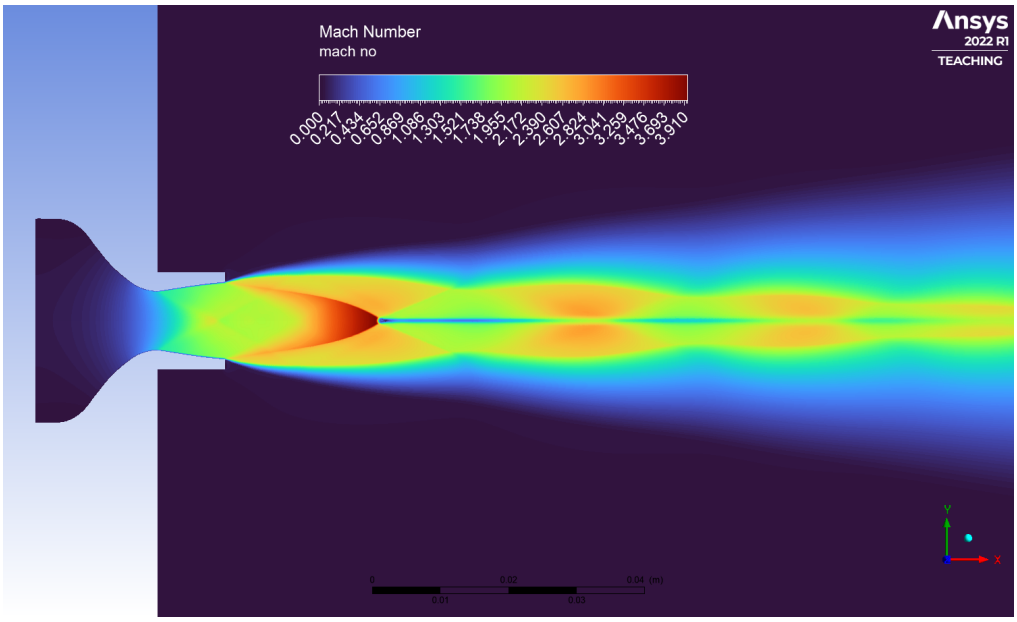


Figure 7.2: TIC case 1 – nozzle Mach number contour.

### Aerospike

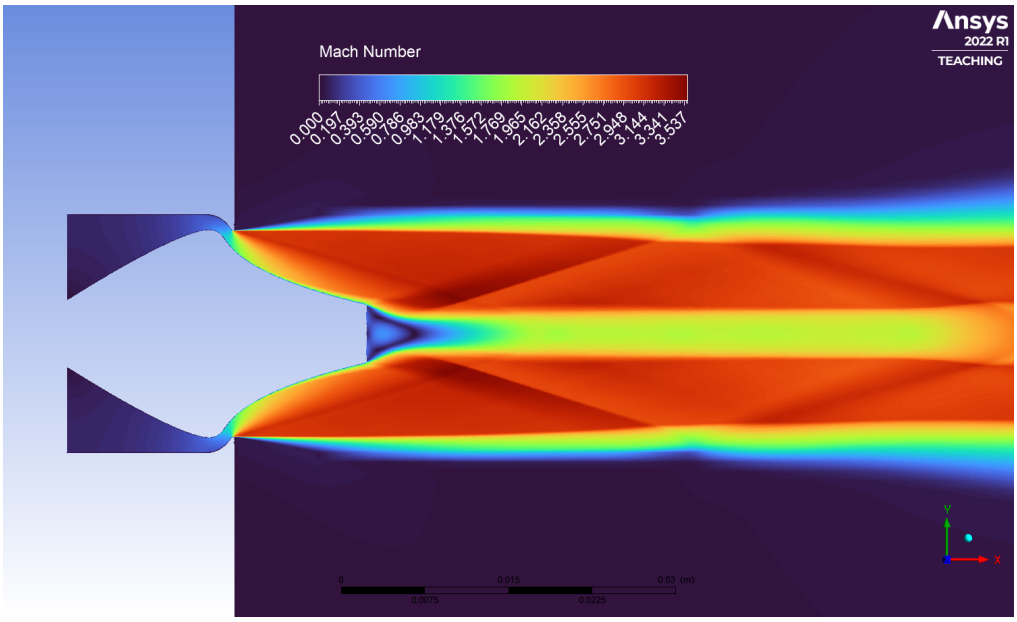


Figure 7.3: AS case 1 – nozzle Mach number contour.

### Dual Bell

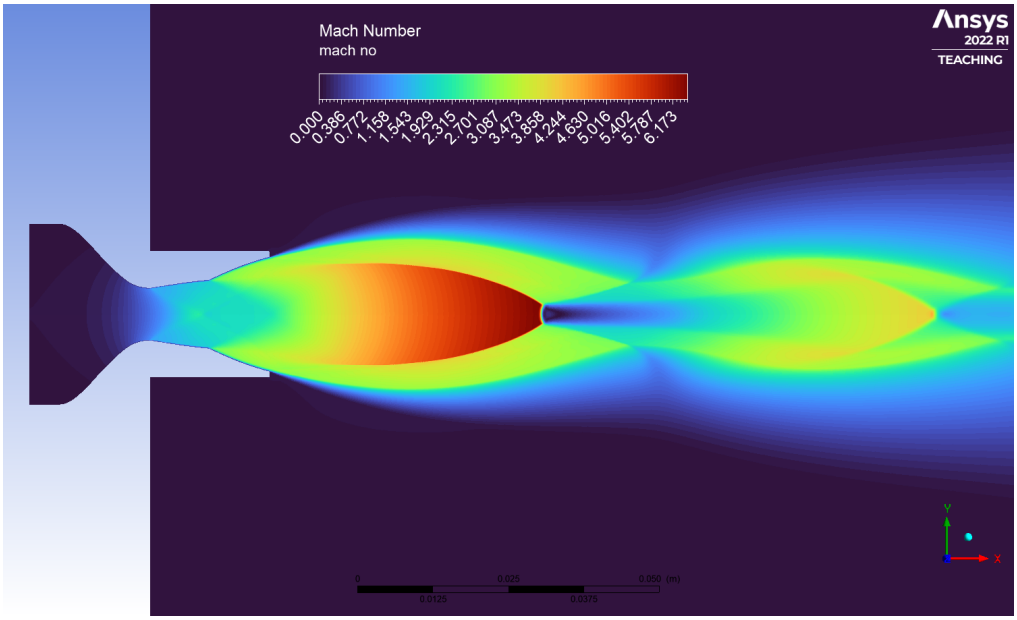


Figure 7.4: DB case 1 – nozzle Mach number contour.

### Expansion-Deflection

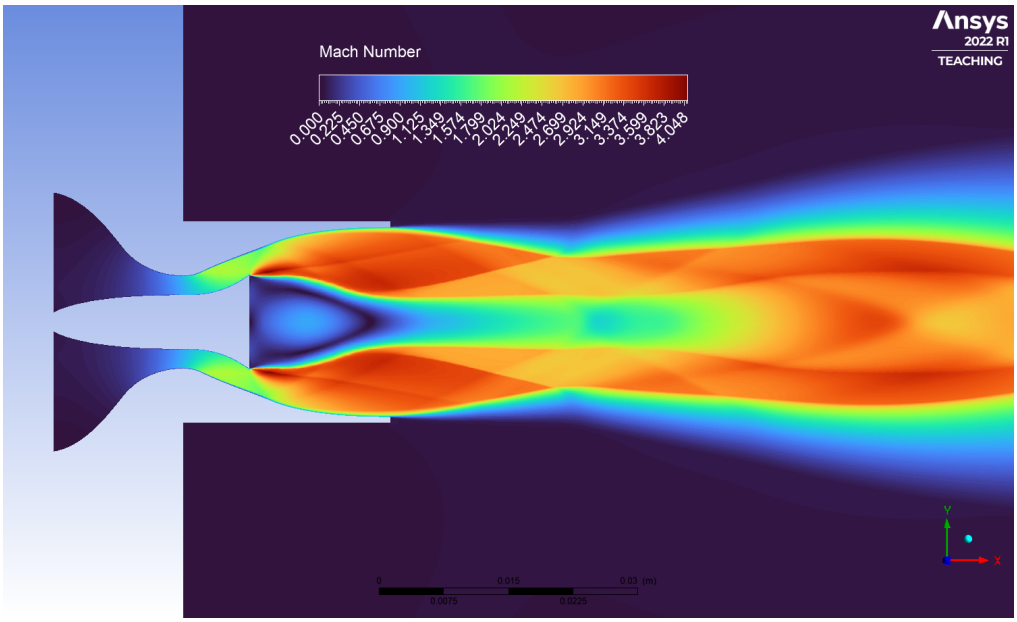


Figure 7.5: ED case 1 – nozzle Mach number contour.

## 7.2 Case 2 results – Off-Design static burn

Similarly to the previous one, case 2 focuses on nozzle performance, but this time at an operating pressure of 101325 Pa (standard atmosphere sea-level pressure). Table 7.2 shows the evaluated nozzle performance.

The first noticeable detail is the very low performance of the ED nozzle, which seems to have a very weak altitude compensation capability (very low $p_e/p_a$). From a first analysis, this is probably accountable to poor design factors and to reasons intrinsic to the simulation software (which will be later discussed in the validation chapter).

Besides, the AS demonstrates a great compensation capability (pressure expansion ratio very close to 1) and great performance, even close – if not higher if compared with the RAO – than the bell nozzles, which obviously take advantage of a design pressure that is less far from the current operative one, despite their unavoidable over-expansion.

TIC and DB obviously show very similar values, since when the DB is operating at higher pressures, they are basically the same nozzle. However, the TIC performs slightly better, due to the little recirculation zone that causes some losses right next to the second-step walls of the DB.

Table 7.2: Case 2 CFD nozzles performance (SLS).

| **Nozzle** | $F_x$ $[N]$ | $C_F$ | $I_{sp}$ $[s]$ | $NPR_{sim}$ | $p_e/p_a$ | $\dot{m}$ $[g/s]$ |
|---|---|---|---|---|---|---|
| RAO | 27.50 | 0.976 | 42.47 | 4.73 | 0.657 | 66.01 |
| TIC | 29.48 | 1.056 | 45.54 | 4.73 | 0.633 | 65.98 |
| AS | 29.29 | 1.089 | 47.42 | 4.7 | 1.067 | 62.69 |
| DB | 29.20 | 1.036 | 45.18 | 4.73 | 0.624 | 65.88 |
| ED | 19.85 | 0.705 | 30.71 | 4.73 | 0.753 | 65.87 |

Following, the Mach number contours of each nozzle are shown. In the bell nozzles, the shock wave due to the over-expansion is clearly visible in the proximity of the nozzle exit – as the adaptability of the ANCs, which greatly mitigate the over-expansion losses.

### Rao

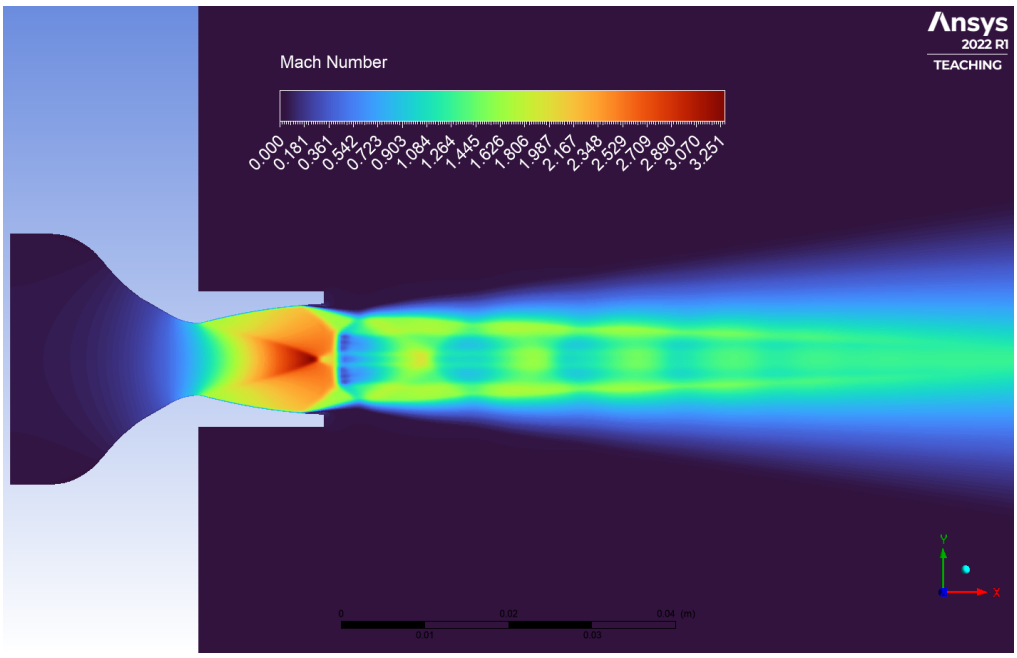


Figure 7.6: RAO case 2 – nozzle Mach number contour.

### Truncated-Ideal-Contour

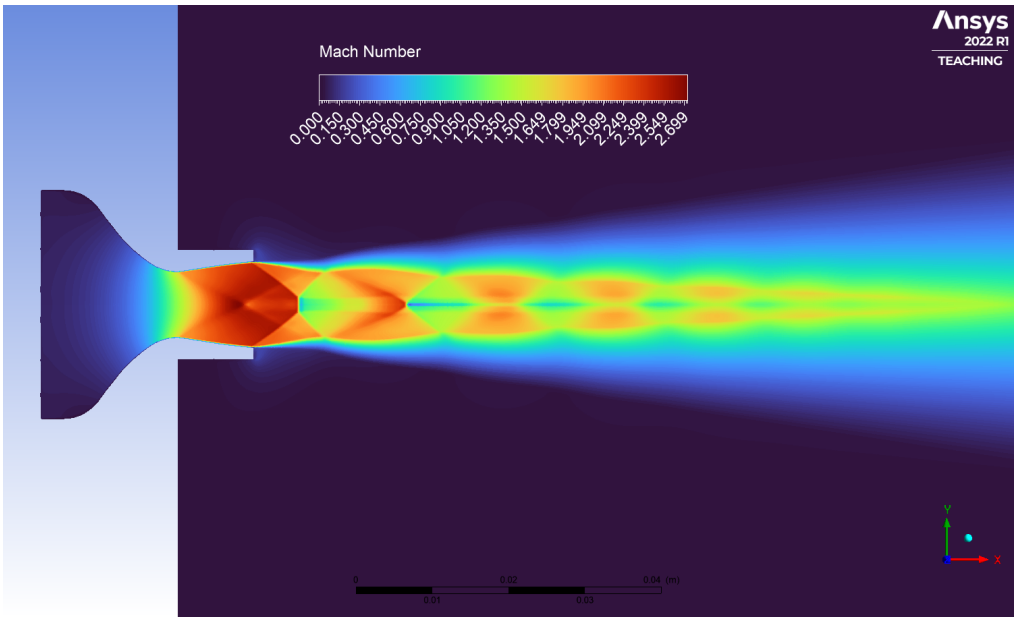


Figure 7.7: TIC case 2 – nozzle Mach number contour.

### Aerospike

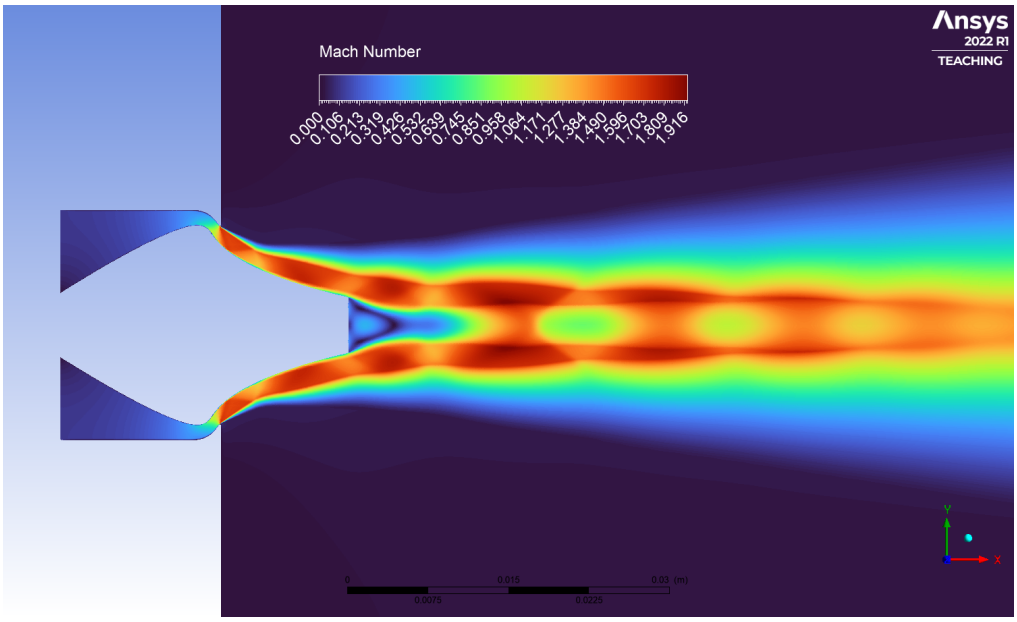


Figure 7.8: AS case 2 – nozzle Mach number contour.

### Dual Bell

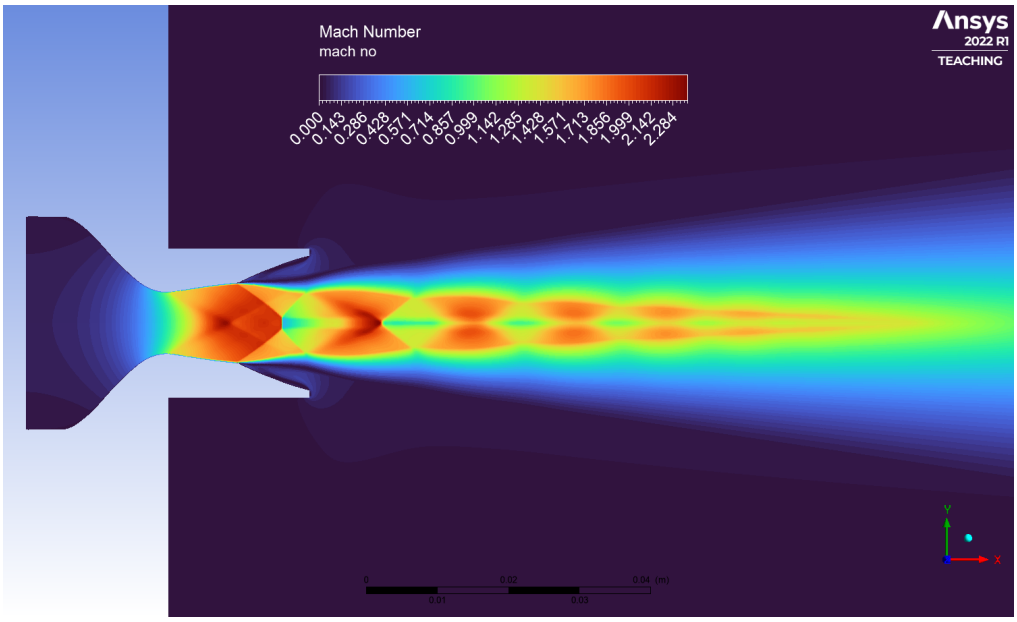


Figure 7.9: DB case 2 – nozzle Mach number contour.

### Expansion-Deflection

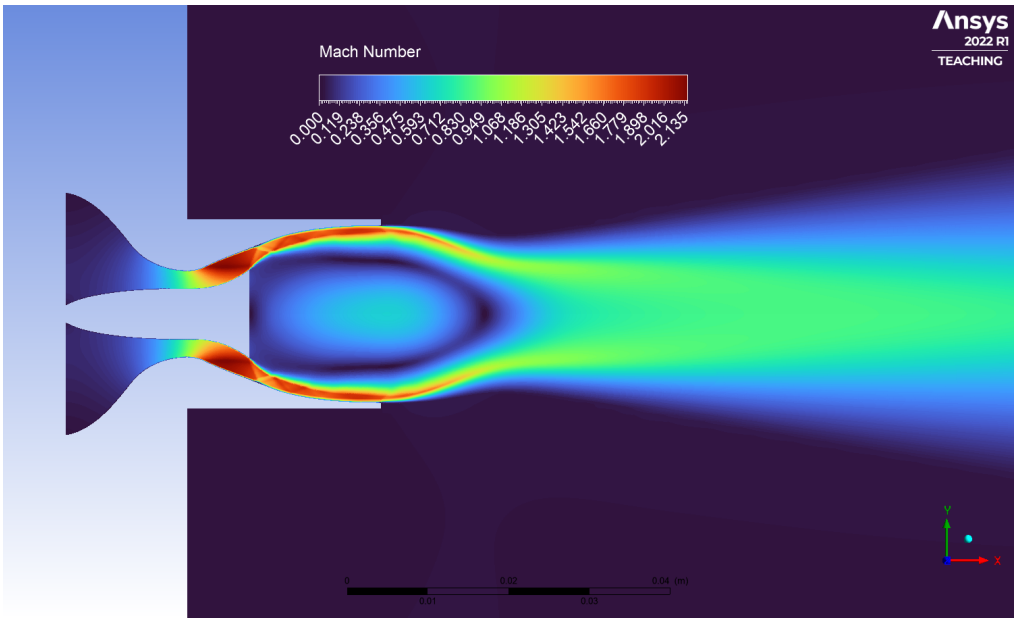


Figure 7.10: ED case 2 – nozzle Mach number contour.

## 7.3 Case 3 results – SLS Aerodynamic Performance

Case 3 doesn't really represent a real case scenario, but mainly aims to provide a term of comparison for the retro-propulsion one. Hence, table 7.3[1] shows the evaluated aerodynamic characteristics. Drag values are still incomplete because the wake effects are not considered; nevertheless, with respect to Tapia Mancera [6], the booster side contribution is now integrated.

From the data, is clear that no substantial differences emerge from the comparison between the nozzles. The macro-behavior of the flow around the booster is weakly influenced by the small structural differences in the nozzle area. However, larger nozzles – as the DB and especially the ED – present slightly lower values of $C_{pb}$ and $C_D$ (and $D$), due to their size that causes the flow to spread wider on the sides.

Table 7.3: Case 3 CFD aerodynamic performance (SLS – 60 m/s counter-flow).

| **Nozzle** | $C_{ps}$[1] | $C_{pb}$[2] | $C_D$[3] | $D$ $[N]$[3] | $v_{side,max}$ $[m/s]$ |
|---|---|---|---|---|---|
| RAO | -0.521 | 0.941 | 0.802 | 15.02 | 73.56 |
| TIC | -0.518 | 0.929 | 0.814 | 15.24 | 73.48 |
| AS | -0.547 | 0.897 | 0.795 | 14.89 | 73.55 |
| DB | -0.533 | 0.952 | 0.768 | 14.39 | 73.46 |
| ED | -0.551 | 0.824 | 0.729 | 13.65 | 73.55 |

[1] measured at 1 $r$ of distance from the baseplate
[2] measured at 2/3 $r$ of the radius of the baseplate
[3] incomplete reference values

Following, for each nozzle, velocity and turbulence kinetic energy ($tke$) contours are shown, where it's possible to observe the counter-flow detachment due to the interaction with the booster and the following re-attachment on the side after a certain distance. Since the flow is subsonic, it begins to diverge before actually reaching the body.

[1]The table shows just vertex values at specific points for the pressure coefficient; a more deepened preliminary analysis around the whole body is faced in Appendix B.

**Rao**

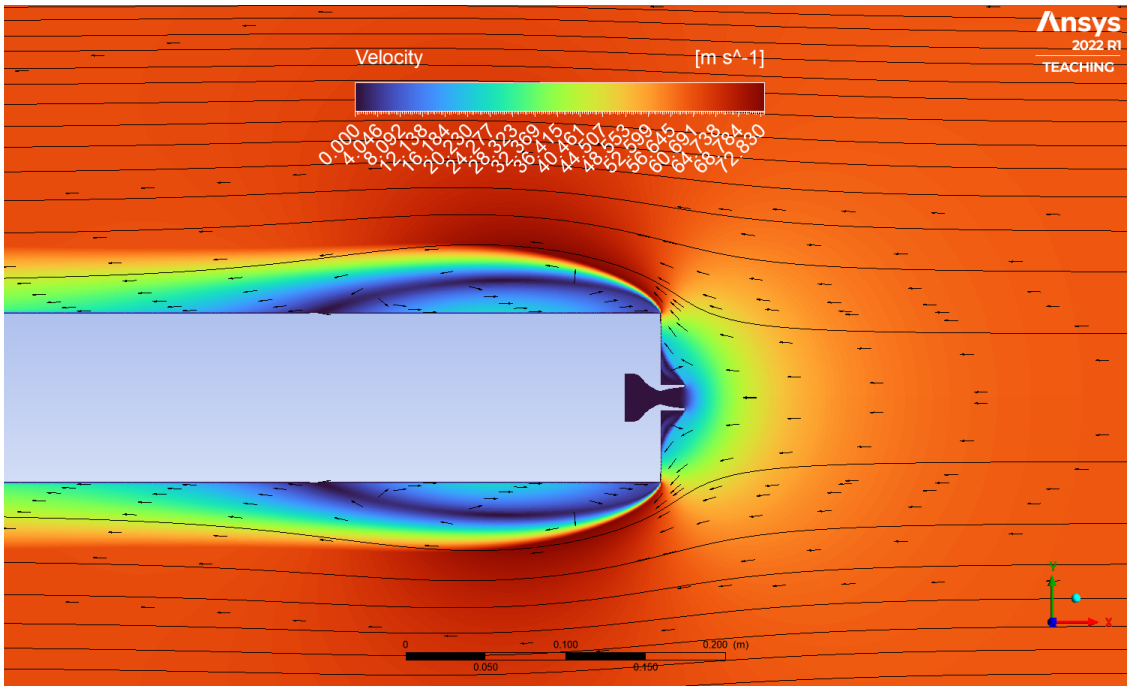


(a) Velocity contour with field vectors and streamlines.

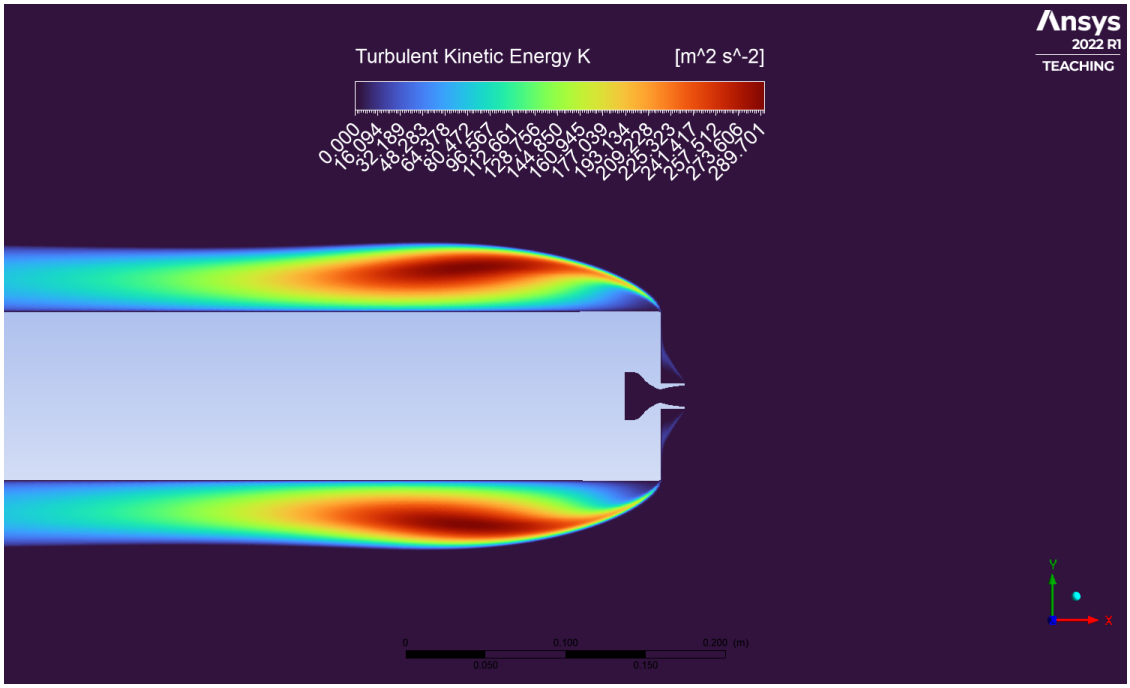


(b) Turbulence kinetic energy contour.

Figure 7.11: RAO nozzle case 3 contours.

**Truncated-Ideal-Contour**

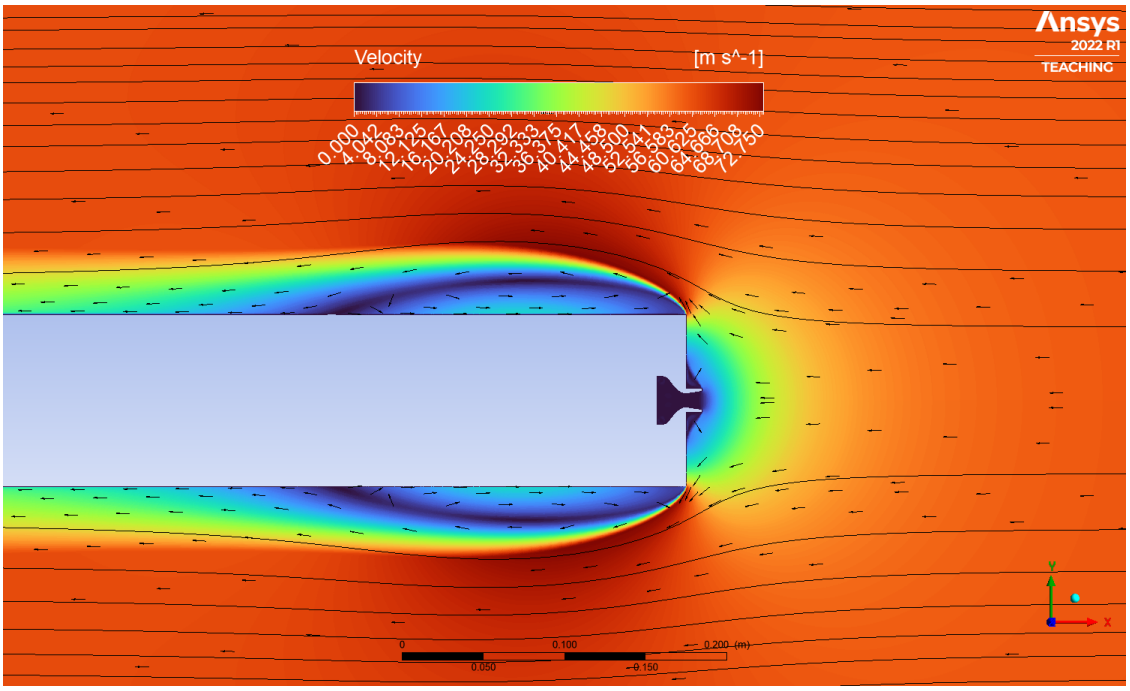


(a) Velocity contour with field vectors and streamlines.

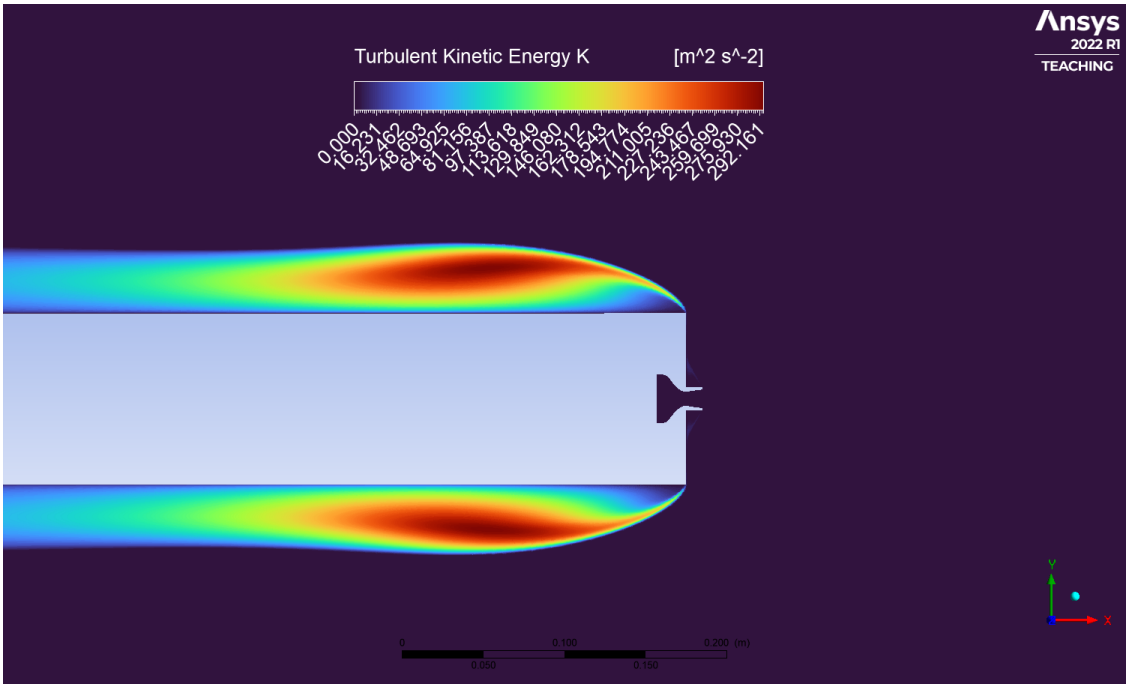


(b) Turbulence kinetic energy contour.

Figure 7.12: TIC nozzle case 3 contours.

**Aerospike**

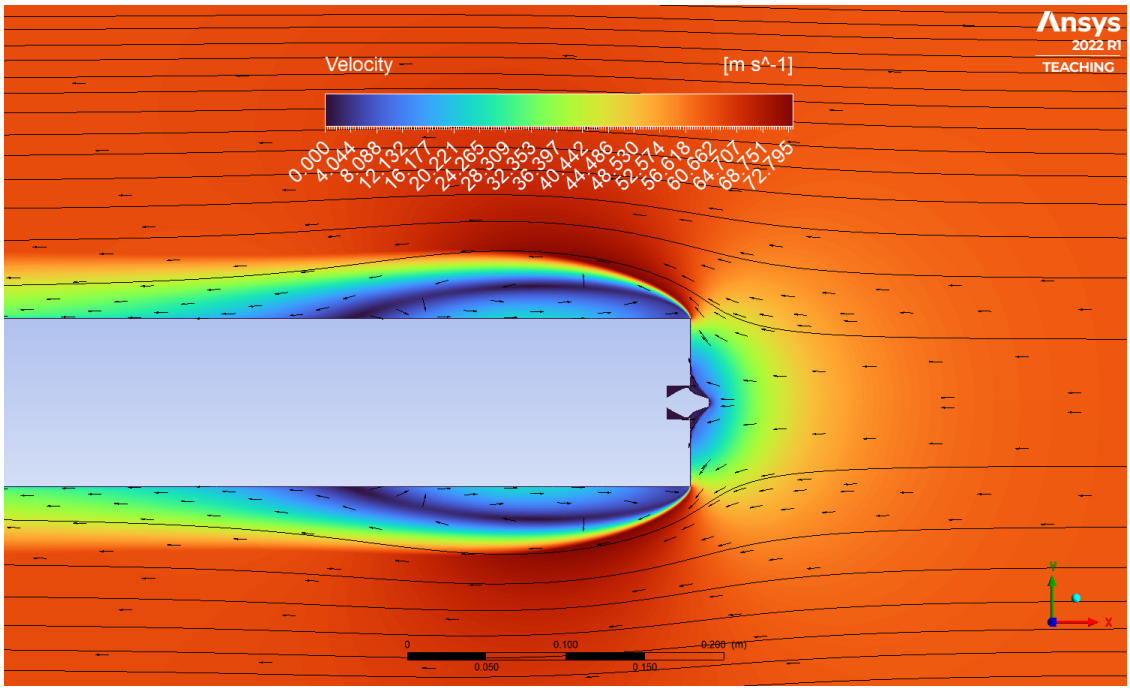


(a) Velocity contour with field vectors and streamlines.

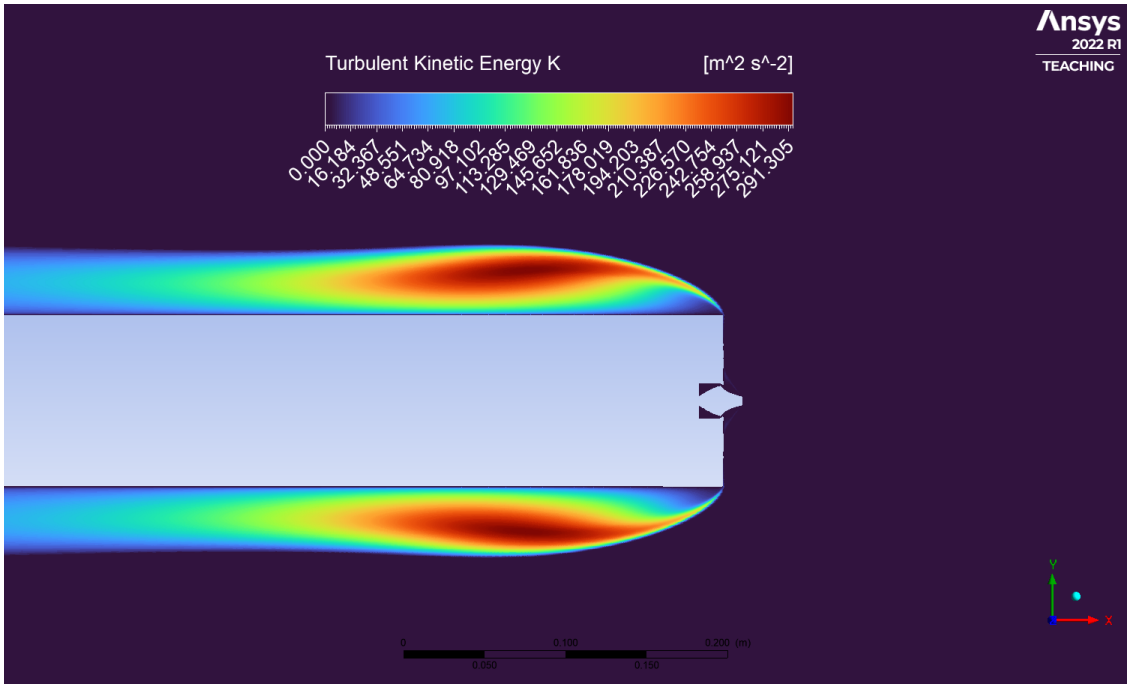


(b) Turbulence kinetic energy contour.

Figure 7.13: AS nozzle case 3 contours.

### Dual Bell

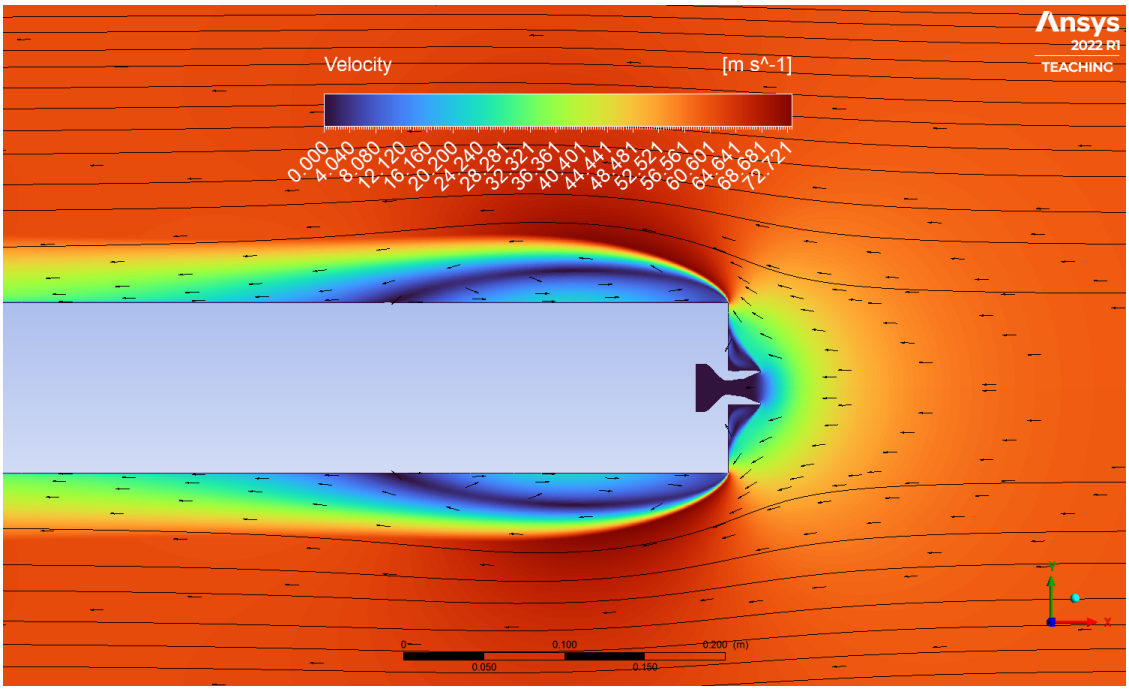


(a) Velocity contour with field vectors and streamlines.

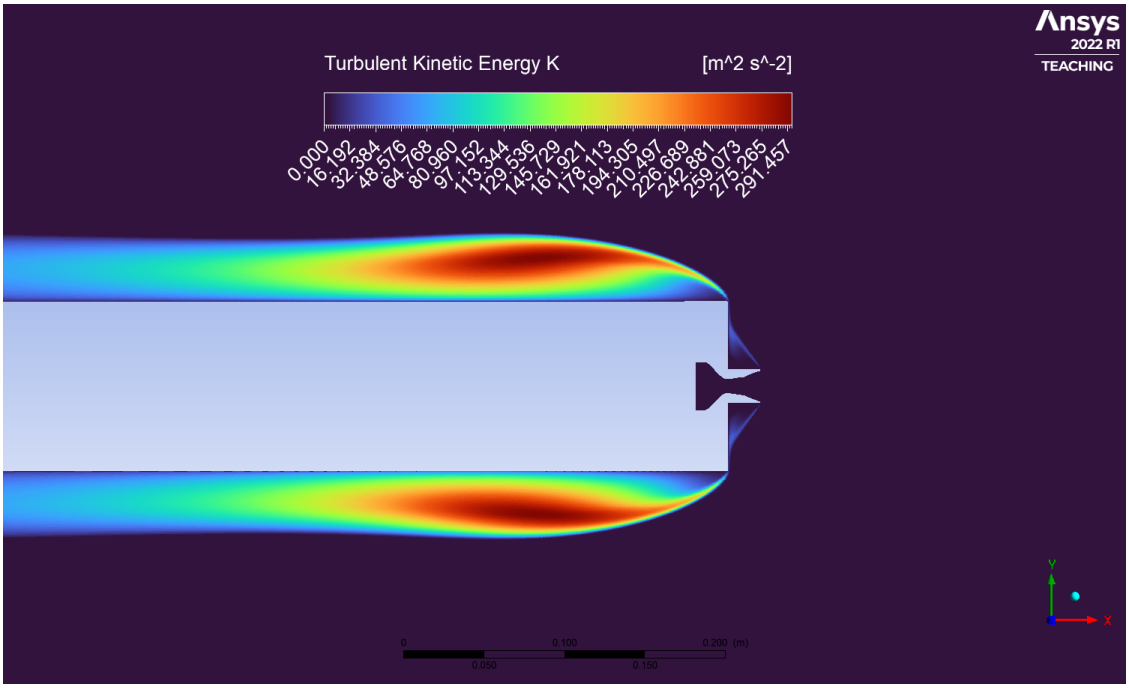


(b) Turbulence kinetic energy contour.

Figure 7.14: DB nozzle case 3 contours.

### Expansion-Deflection

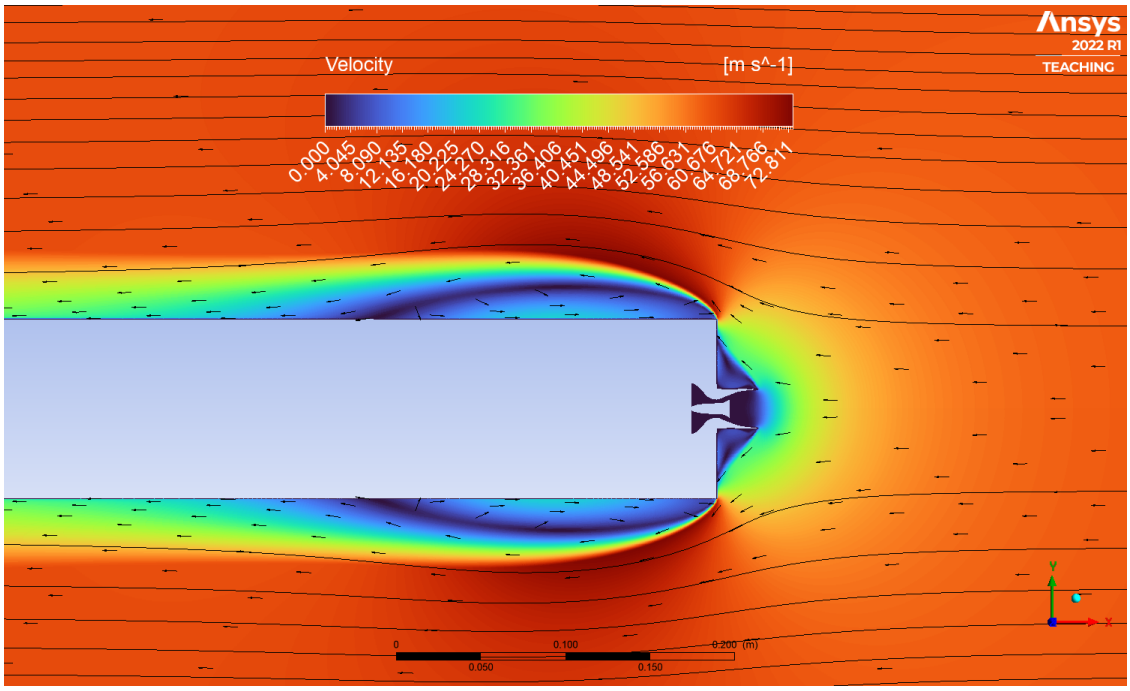


(a) Velocity contour with field vectors and streamlines.

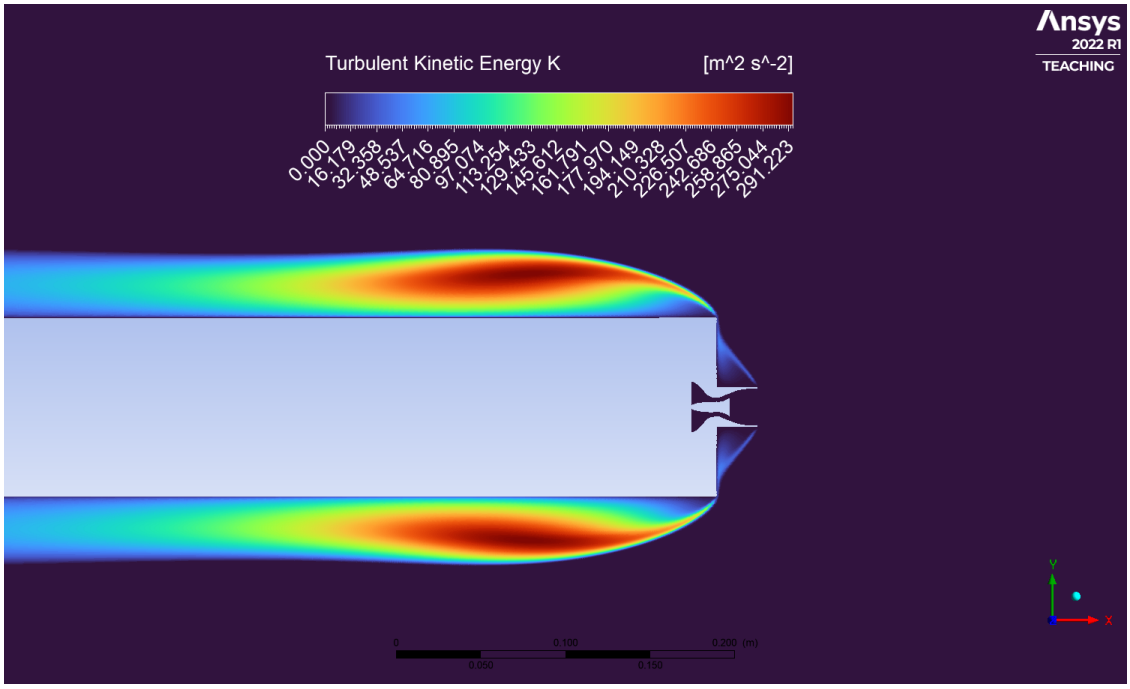


(b) Turbulence kinetic energy contour.

Figure 7.15: ED nozzle case 3 contours.

## 7.4 Case 4 results – Subsonic Retro-propulsion

This fourth case pictures the very last phase of the landing burn, where both the engine and the counter flow are here turned on, so both the nozzle and the aerodynamic performances are interesting to study; table 7.4 shows the first ones.

The data interpretation given for case 2 remains valid: the AS is able to greatly adapt to the high pressure, in contrast to the poor performance of the ED. The DB acts just a bit worse than the TIC, but still similar to the AS; while the RAO follows with around 7% less thrust.

Table 7.4: Case 4 CFD nozzles performance (SLS SubRP).

| **Nozzle** | $F_x$ $[N]$ | $C_F$ | $I_{sp}$ $[s]$ | $NPR_{sim}$ | $p_e/p_a$ |
|---|---|---|---|---|---|
| RAO | 27.77 | 0.986 | 42.94 | 4.833 | 0.637 |
| TIC | 29.70 | 1.054 | 45.86 | 4.827 | 0.644 |
| AS | 29.53 | 1.098 | 47.82 | 4.8 | 1.065 |
| DB | 29.29 | 1.040 | 45.11 | 4.83 | 0.635 |
| ED | 20.29 | 0.720 | 31.40 | 4.828 | 0.755 |

Table 7.5[2] shows instead the aerodynamic characteristics of the booster equipped with each nozzle. In addition to case 3, the momentum thrust ratio, the aerodynamic thrust coefficient, and the stagnation point distance are presented, since these parameters directly come from the interaction of the two opposite flows.

Table 7.5: Case 4 CFD aerodynamic performance (SLS – 60 m/s counter-flow).

| **Nozzle** | $C_{ps}$[1] | $C_{pb}$[2] | $C_D$[3] | $D$ $[N]$[3] | $MFR$[4] | $C_T$ | st.p.d.[5] |
|---|---|---|---|---|---|---|---|
| RAO | -0.046 | 0.443 | 0.459 | 8.60 | 0.873 | 1.482 | 295 |
| TIC | -0.065 | 0.448 | 0.492 | 9.22 | 0.888 | 1.696 | 301 |
| AS | -0.069 | 0.401 | 0.458 | 8.59 | 0.709 | 1.576 | 292 |
| DB | -0.068 | 0.417 | 0.461 | 8.63 | 0.707 | 1.673 | 300 |
| ED | -0.069 | 0.329 | 0.384 | 7.17 | 0.844 | 1.077 | 281 |

[1] m. at 1 $r$ of distance from the baseplate
[2] m. at 2/3 $r$ of the radius of the baseplate
[3] incomplete reference values
[4] momentum-flux-ratio
[5] stagnation point distance from baseplate

The data translate into the following consideration:

1. The $C_{ps}$ is nearly the same for each nozzle and close to zero, which means that the flow is basically attached to the booster side and it's almost horizontal;

[2]The table shows just vertex values at specific points for the pressure coefficient; a more deepened preliminary analysis around the whole body is faced in Appendix B.

2. Again, the ED manifests the poorest performance, with low values of $C_{pb}$ and $C_D$. The different shapes of the plume characteristic of each nozzle affect the aerodynamic performance of the entire body, resulting in non-negligible differences – in particular, the TIC generates ca. 7% higher drag;

3. Figure 7.16 shows a linear correlation between the aerodynamic thrust coefficient and the distance of the stagnation point. The relation is strictly honored by all the nozzles but the AS, which was expected to develop a further stagnation point. This reflects the same issue experienced by Tapia Mancera [6]: the explanation could actually refer to the higher momentum dissipation ratio caused by higher values of jet turbulence, associated with a shorter laminar core of the jet flow, due to the peculiar different shape of the AS's exhaust gasses (far from a classical bell nozzle plume).

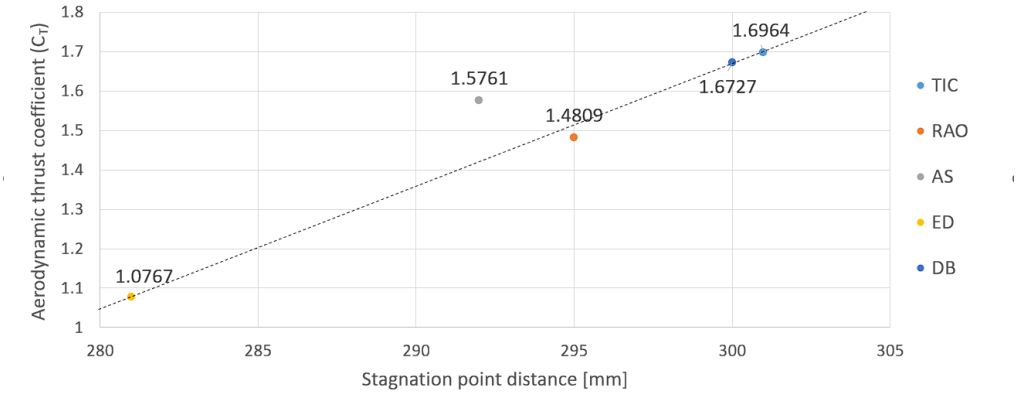


Figure 7.16: Correlation between aerodynamic thrust coefficient ($C_T$) and distance of the stagnation point (from the booster base).

Following, the velocity contours show a very different flow re-attachment compared to case 3, because by the time the counter-flow reaches the booster, it has already had time to become nearly horizontal again. On the other hand, the *tke* contours highlight the stagnation point that generates from the interaction between the counter-flow and the nozzle plume jet.

**Rao**

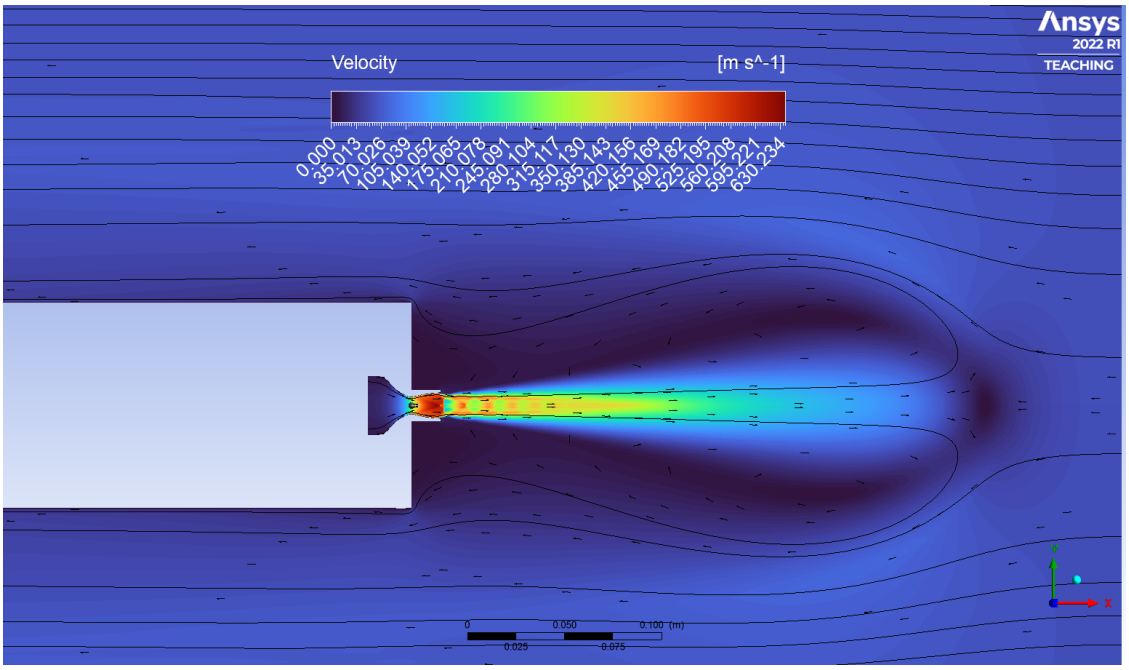


(a) Velocity contour with field vectors and streamlines.

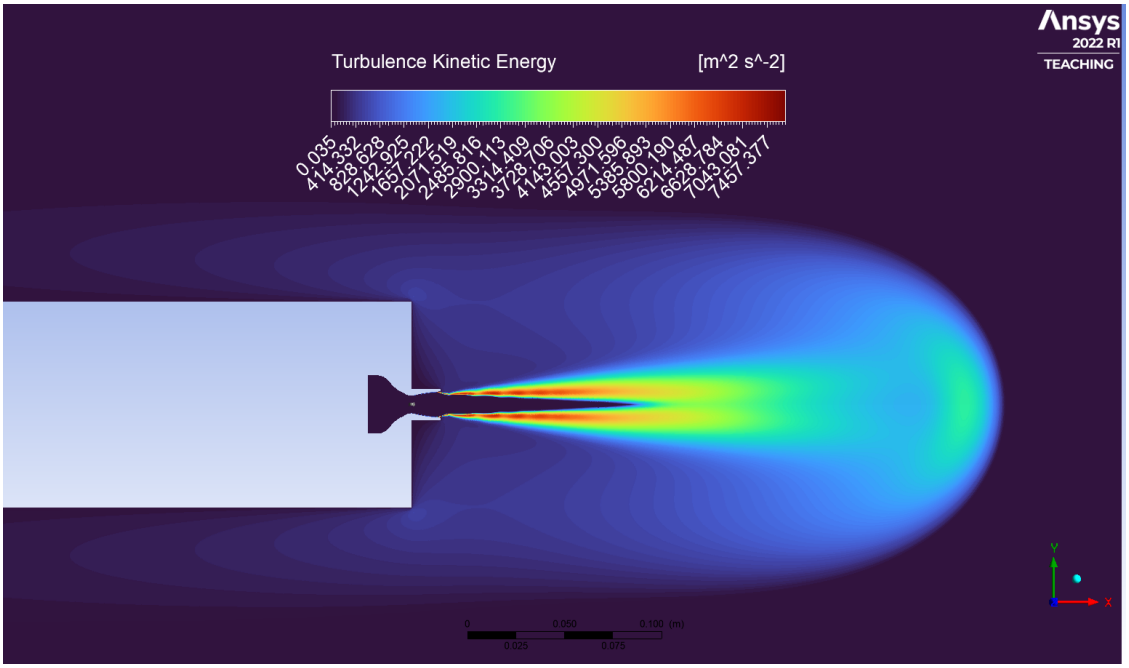


(b) Turbulence kinetic energy contour.

Figure 7.17: RAO nozzle case 4 contours.

**Truncated-Ideal-Contour**

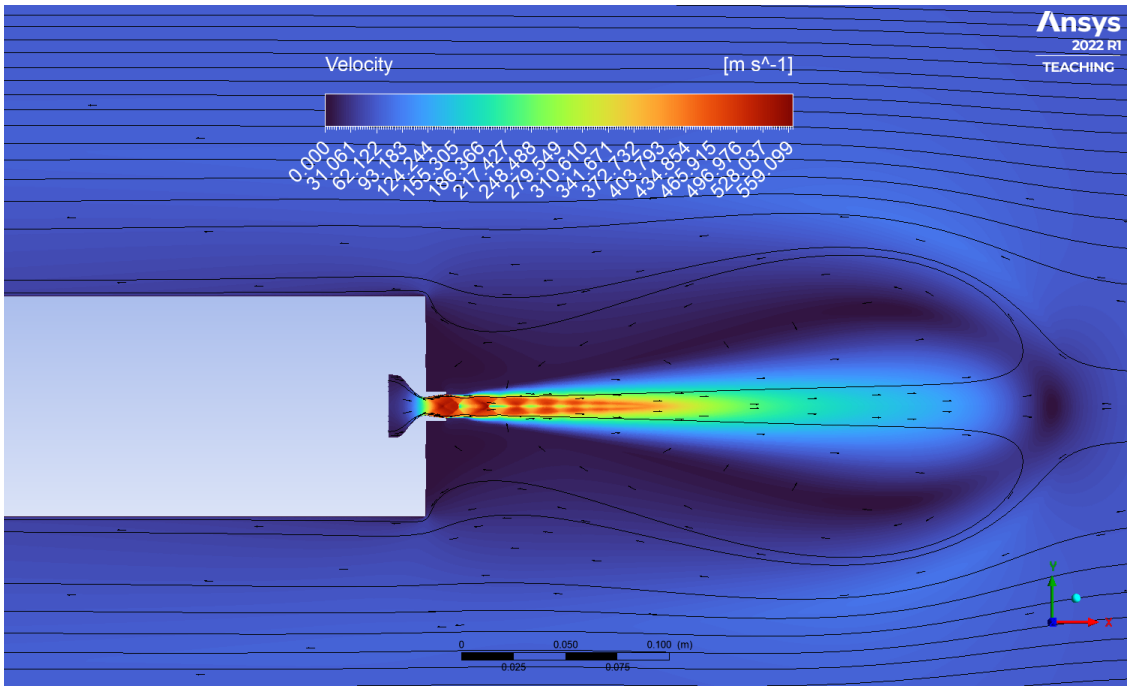


(a) Velocity contour with field vectors and streamlines.

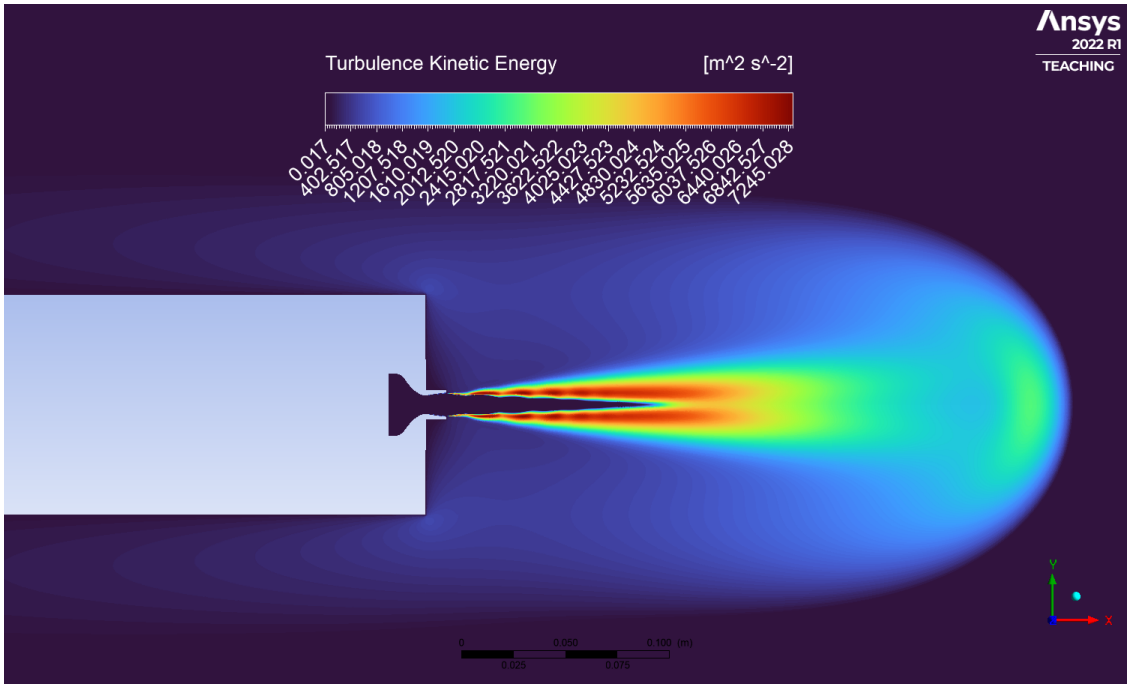


(b) Turbulence kinetic energy contour.

Figure 7.18: TIC nozzle case 4 contours.

**Aerospike**

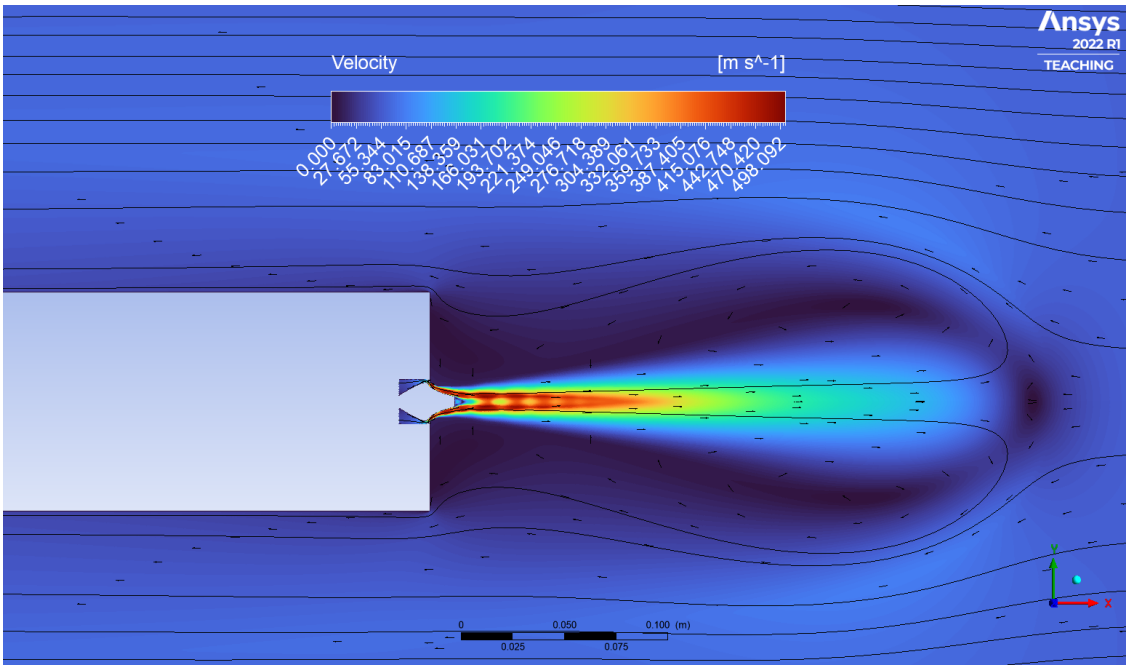


(a) Velocity contour with field vectors and streamlines.

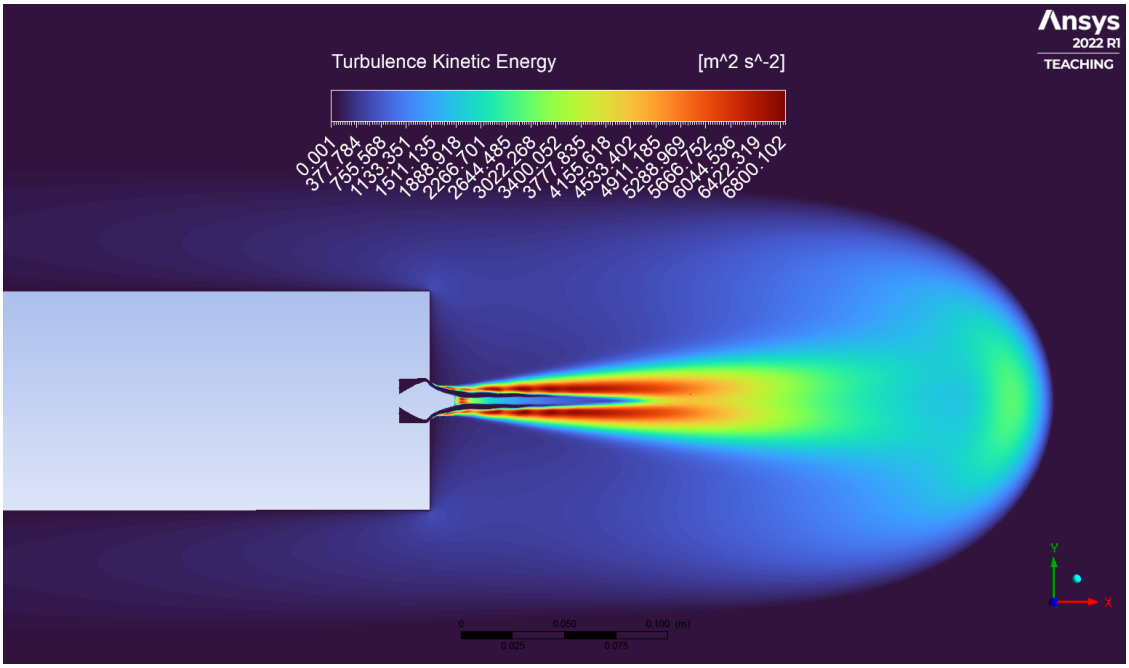


(b) Turbulence kinetic energy contour.

Figure 7.19: AS nozzle case 4 contours.

### Dual Bell

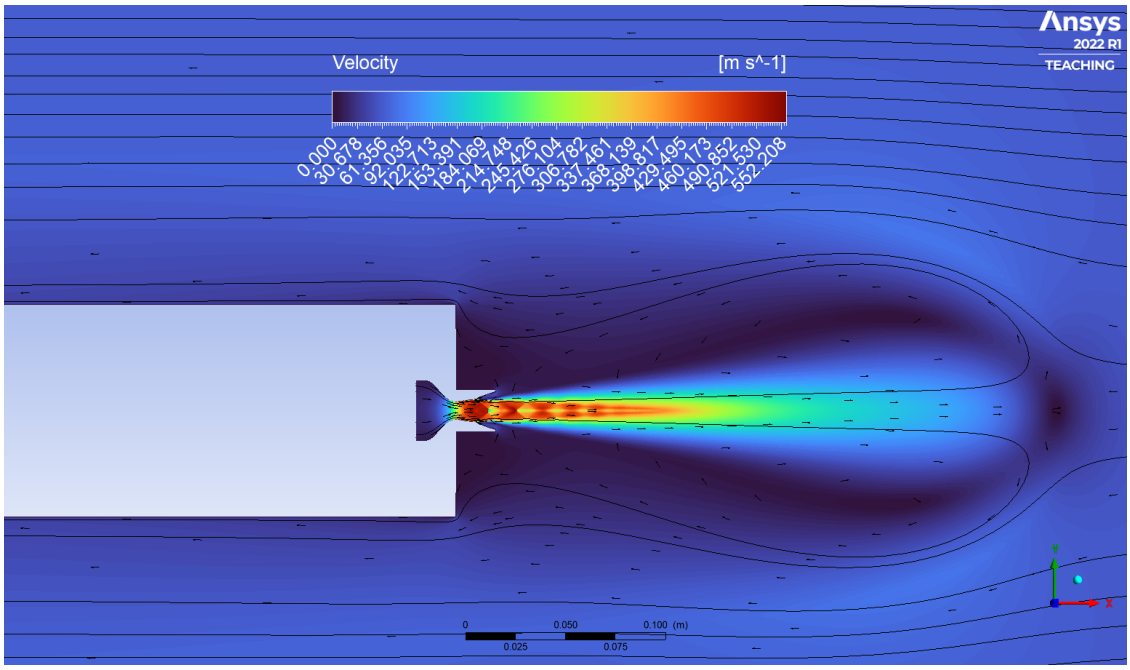


(a) Velocity contour with field vectors and streamlines.

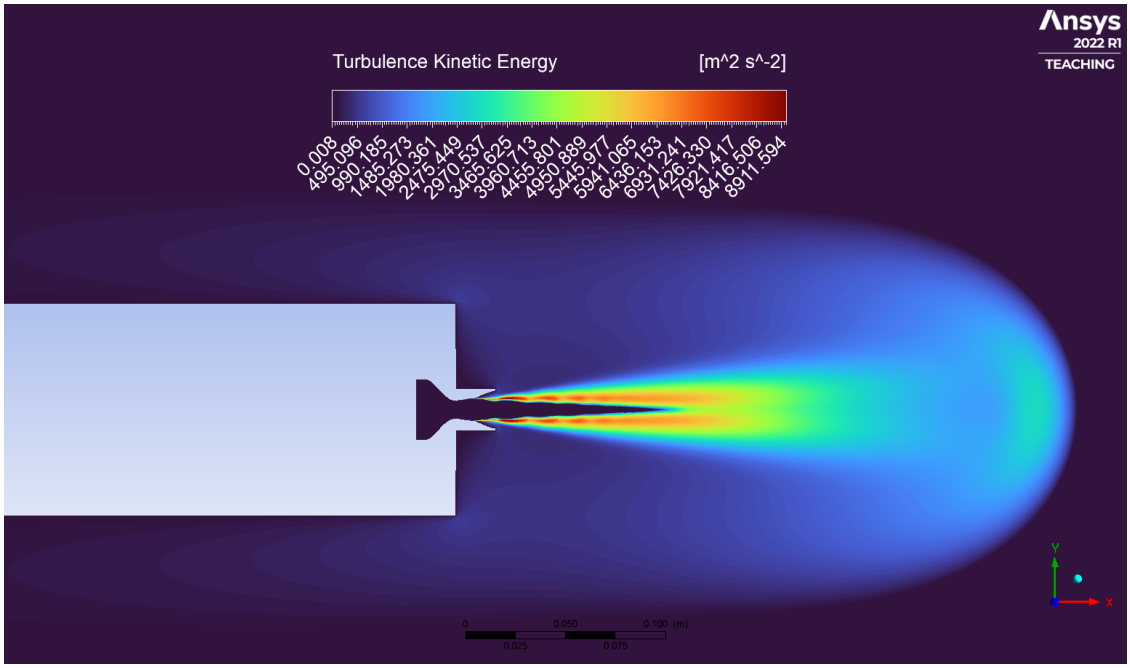


(b) Turbulence kinetic energy contour.

Figure 7.20: DB nozzle case 4 contours.

### Expansion-Deflection

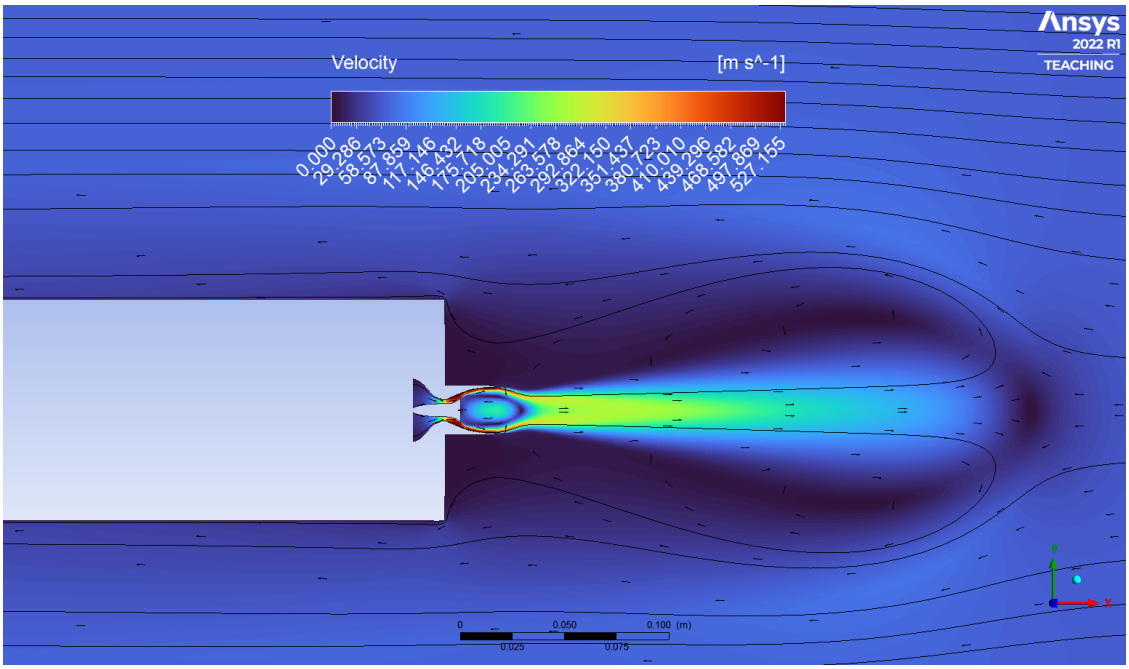


(a) Velocity contour with field vectors and streamlines.

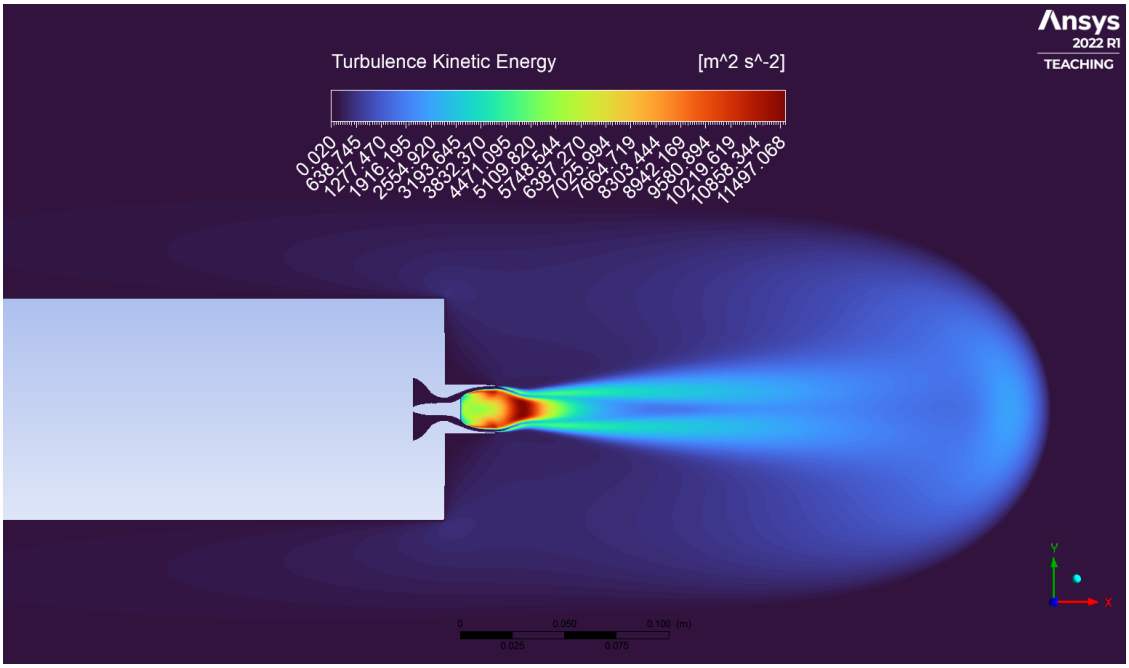


(b) Turbulence kinetic energy contour.

Figure 7.21: ED nozzle case 4 contours.

# *Chapter 8*

# *Verification & Validation*

## 8.1 Verification

As anticipated in Chapter 3, the verification process consisted of two key aspects:

1. Correspondence of the performance with the expected theoretical values, coming from design parameters, hand calculations, and previous literature;
2. Meeting of the desired convergence criteria for the simulation, which are:
   - All residual magnitudes below $10^{-5}$;
   - Stability and monotonous convergence for at least 100 iterations of key parameters: *momentum thrust* ($f_j = \dot{m}_p v_e$) when the engine is turned on, and *drag coefficient* when the counter-flow is turned on ($C_D$).

**Comparison between CFD and analytical results**

Table 8.1 shows the comparison referred to in point 1 for the first two cases, enhanced by a colored gradient. The percentage variations between the CFD results and the expected theoretical values (shown in tables 4.3 and 4.4) are evaluated. Overall there's a sufficient matching between the two: the numerical values almost never differ more than a 3%, and generally they are predictably lower since the hand calculation doesn't take into account the non-isentropic phenomena. Only two exceptions emerge from this trend: the AS – in off-design conditions – performs even a bit better than expected in terms of thrust coefficient and specific impulse; on the other hand, the ED nozzle performs substantially worse, 11-12% less than the expected design performance.

In case 3 the pressure coefficients resemble quite well the expected ones: $c_{pb}$ diverges for a maximum of 17.6% compared to the unitary value, while $c_{ps}$ negative

Table 8.1: Nozzles performance variation (%) of CFD (cases 1 and 2) compared to expected values (hand calculations).

| **Nozzle** | **Case** | $F_x$ | $C_F$ | $I_{sp}$ | $\dot{m}$ |
|---|---|---|---|---|---|
| RAO | 1 | -2.69 % | -2.47 % | -0.77 % | -1.96 % |
| | 2 | -1.89 % | -1.73 % | -1.00 % | -0.93 % |
| TIC | 1 | -1.72 % | -1.84 % | -0.53 % | -1.53 % |
| | 2 | -1.93 % | -0.85 % | -1.00 % | -0.97 % |
| AS | 1 | -2.05 % | -1.25 % | -0.36 % | -1.72 % |
| | 2 | -0.44 % | 0.33 % | 1.17 % | -1.64 % |
| DB | 1 | -2.60 % | -6.24 % | 0.00 % | -1.12 % |
| | 2 | -2.86 % | -2.72 % | 0.00 % | -1.12 % |
| ED[1] | 1 | -12.11 % | -11.94 % | -11.09 % | -1.12 % |
| | 2 | - | - | - | -1.14 % |

[1] $M_e$ variation (onD) = -0.57%

values are coherent with the -0.38 obtained in Nonaka's case 0 (see figures 2.18 and 2.19) [27].

For case 4 a decreased pressure on the base, in expense to an increased one on the sides, and a slight improvement of the nozzle performance were expected. This trend is actually being respected but will be further discussed in Chapter 9.

### Meeting of convergence criteria

Out of the twenty simulations, thirteen converged well meeting all the convergence criteria. The other seven are here listed:

- case 1 and 4 for TIC nozzle;
- case 2 and 4 for RAO nozzle;
- case 1,2 and 4 for DB nozzle.

In these cases the residuals were not able to reach the desired values, instead they entered various loops around the $10^{-3}$ region. At the same time, the monitored key parameters tended to move around certain values, without actually converging in a monotonous way to a constant number, even if the oscillation range was always within a margin of $\pm$ 10%. It should be noticed that all the convergence issues occurred in bell nozzles where the over-expansion generated a shock wave. The latter's position is always trivial to identify with sufficient accuracy for the software, also because of its thickness on the order of $10^{-7}$ $m$ [41, 33]. This phenomenon could easily obstruct the simulation convergence and its stability. In particular, case 4 for TIC and especially RAO, was revealed to be the most challenging one to make converge. A very higher number of cells may encourage the transient effects to come to play, which implies issues for a steady-state solver. For this specific cases

the number of cells was therefore decreased to six digits numbers, since even other Fluent solvers (e.g. *SIMPLE*) – which are supposed to favor the convergence at the cost of some time – or the modification of solving parameters didn't work.

## 8.2 Validation

The results validation was performed both from a qualitative and a quantitative perspective by comparing engine performance (cases 1 and 2), aerodynamic performance (cases 3 and 4), and nozzle jet-flow topology (taking advantage of BOS images).

### Data validation

Table 8.2 displays the experimental results obtained in the laboratory for each of the tested nozzles (unfortunately, there was not enough time to 3D print and test the dual-bell nozzle) and the percentage variation of the CFD values – shown in tables 7.1 and 7.2 – with respect to the reported experimental ones. It should be highlighted that each value of case 2 was subsequently adjusted in order to match the reference $NPR$, after a proper reconstruction of the measurement curves (an explicit comparison of the values pre- and post-correction is shown in Appendix C) [28, 42].

Table 8.2: Nozzles performance variation (%) between CFD (cases 1 and 2) and the reported experimental values.

| **Nozzle** | **Case** | $F_x$ | | $C_F$ | |
|---|---|---|---|---|---|
| | | exp. $[N]$ | var. | exp. $[N]$ | var. |
| RAO | 1 | 34.70 | 4.2 % | 1.23 | 4.4 % |
| | 2 | 24.50 | 12.24 % | 0.87 | 12.31 % |
| TIC | 1 | 34.64 | 4.1 % | 1.23 | 4.3 % |
| | 2 | 27.58 | 6.9 % | 0.98 | 7.8 % |
| AS | 1 | 38.95 | 0.6 % | 1.43 | 1.7 % |
| | 2 | 28.25 | 3.7 % | 1.04 | 4.7 % |
| ED | 1 | 38.73 | 1.3 % | 1.38 | 1.3 % |
| | 2 | 22.27 | -10.9 % | 0.79 | -10.6 % |

Generally, the simulation results are higher than the experimental ones; this fact is expected, since CFD may ignore some losses that are almost impossible to replicate. In particular, bell nozzles in off-design conditions seem to work substantially better (around 6-11% better), which is probably related to inaccuracies in the numerical performance evaluation due to the intern normal shock wave falling within the nozzle. Thrust and thrust coefficient are calculated using eq. 3.2.1 considering the exit pressure in the exit section of the nozzle, the shock wave inevitably affects the precision of these approximate formulas. The only exception is represented by

the ED nozzle: in this case, the experiments highlight a 12.6% better thrust than the CFD in the off-design case. A possible explanation can be attributed to the fact that, in the simulations, the recirculation area formed downstream of the central body of the nozzle remains at the last pressure it was before the closing of the wake around it, leading to non-realistic values that disturb the accuracy of the results.

Regarding cases 3 and 4, the validation focused on the total drag evaluation. Graphs in figure 8.1 show such a comparison: in case of engine off, only the aerodynamic drag is evaluated, while in the retro-propulsion case also the thrust contribution is taken into account (even here, the CFD considers the dual-bell, which has not been experimentally tested). The most obvious observation refers to the values of aerodynamic values in both cases, mainly due to the pretty different counter-flow types. In case 3, the experimental drag is about 40% greater than in CFD, also because of the incompleteness of the vehicle body in the simulation (top on the booster and wake effects ignored). On the other hand, retro-flow experiments point out a drastic decrease in aerodynamic drag: while in CFD it lowers by about 45%, in the laboratory the drop is up to 89%. This is still due to the different counter flow, in fact, the weaker and thinner conical flow gets basically destroyed by the nozzle jet, without the possibility of re-establishing itself downstream; this effect turns out to be directly proportional to the magnitude of nozzle thrust[28]. The uniform counter-flow is instead able to re-attach on the booster sides after a certain distance, which translates into a higher resulting aerodynamic drag.

Despite these disparities, the overall qualitative behavior of each specimen seems to be coherent: the TIC nozzle demonstrates the highest total drag value, closely followed by the aerospike, the RAO ranks just below (still in a range of ca. 2 $N$). Finally, the ED is the worst due to its poor adaptation capability design. The latter acts even worse in CFD due to the nozzle performance, as expected from the same reasons previously given to justify the low thrust values for case 2.

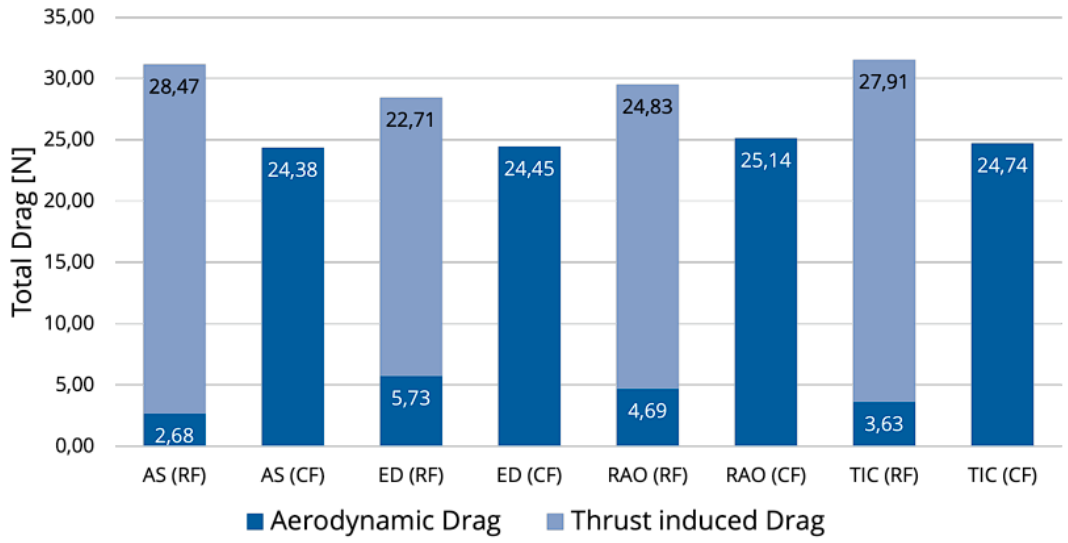


Credits: Portolani [28].

(a) Experiments with conical flow.

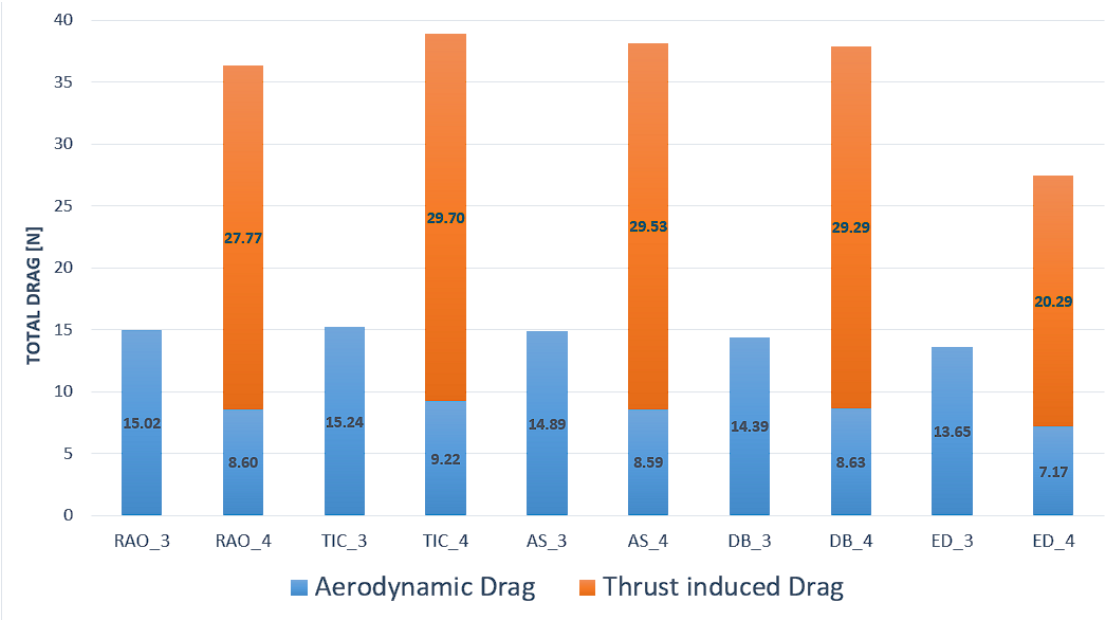


(b) CFD.

Figure 8.1: Total drag generated for every nozzle in cases 3 and 4 compared.

### Visual validation

For the experimentally tested advanced nozzles (aerospike and expansion-deflection), Background-Oriented Schlieren (BOS) was used to derive density gradient images. These are reported below along with the density gradient contours themselves obtained in post-processing. As can be seen from the comparison of the images, there is an excellent match in terms of flow topology and behavior.

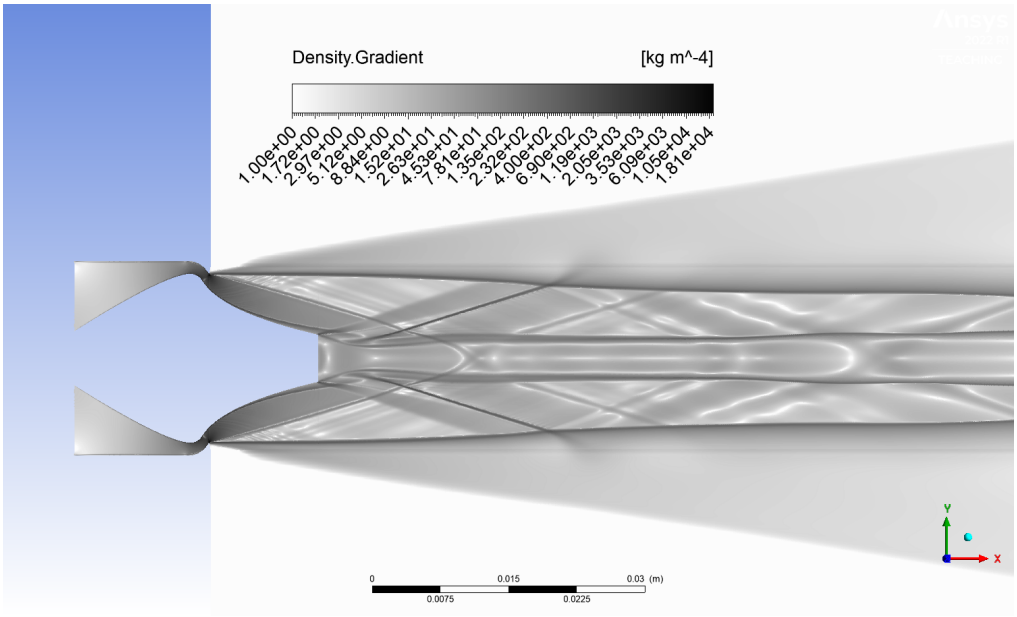


(a) Density gradient contour.

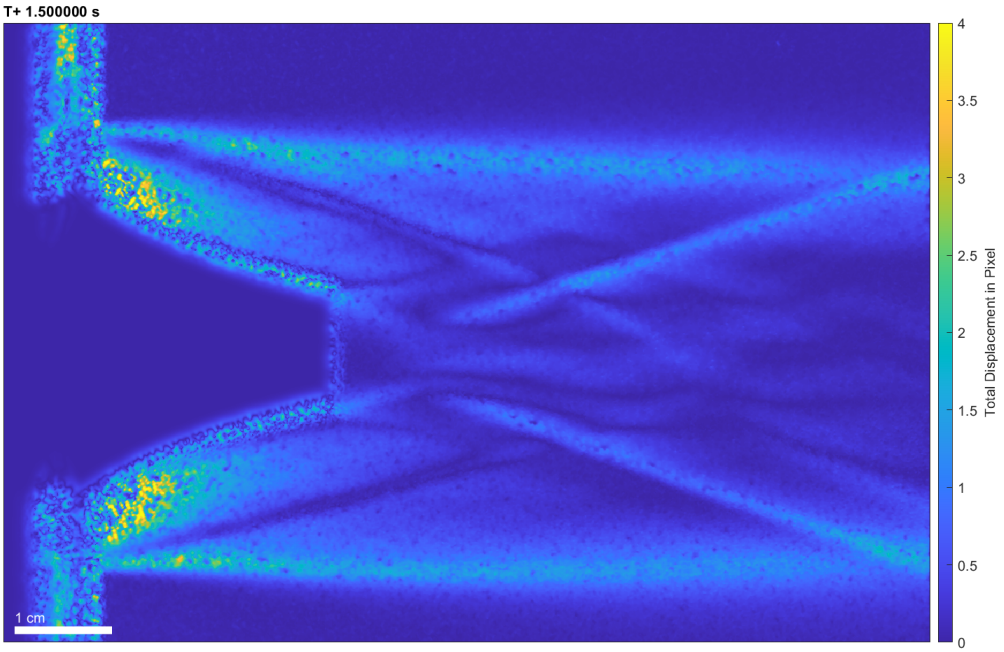


(b) BOS visualization.

Figure 8.2: AS case 1

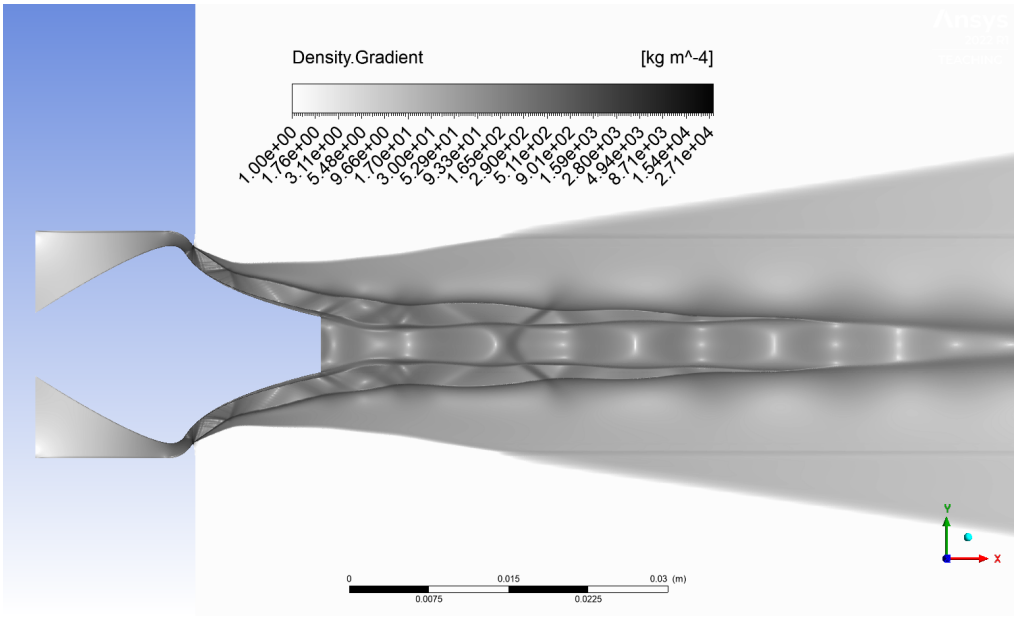


(a) Density gradient contour.

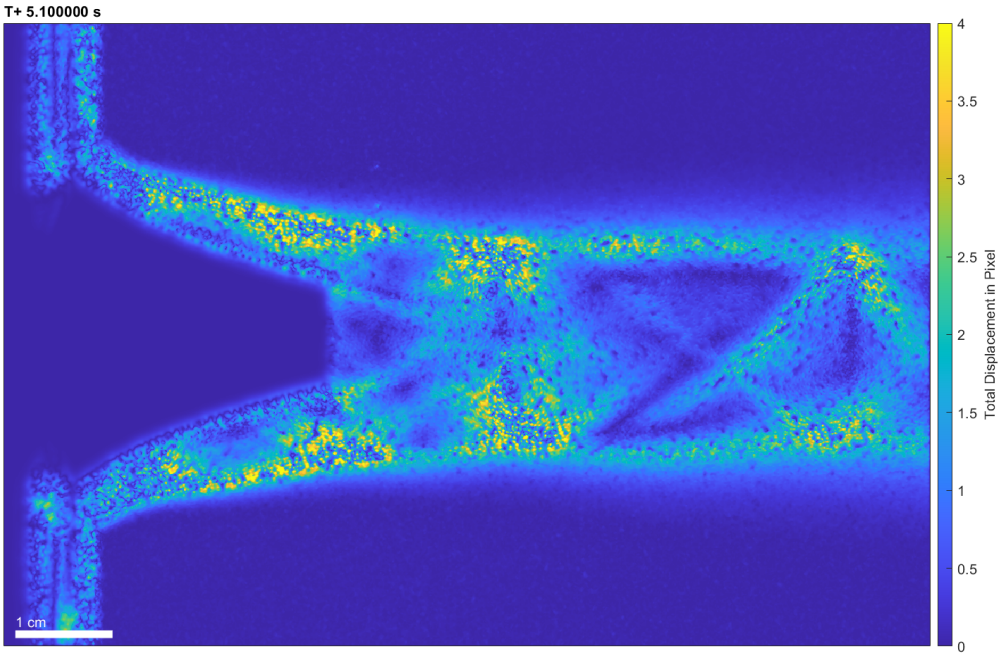


(b) BOS visualization.

Figure 8.3: AS case 2

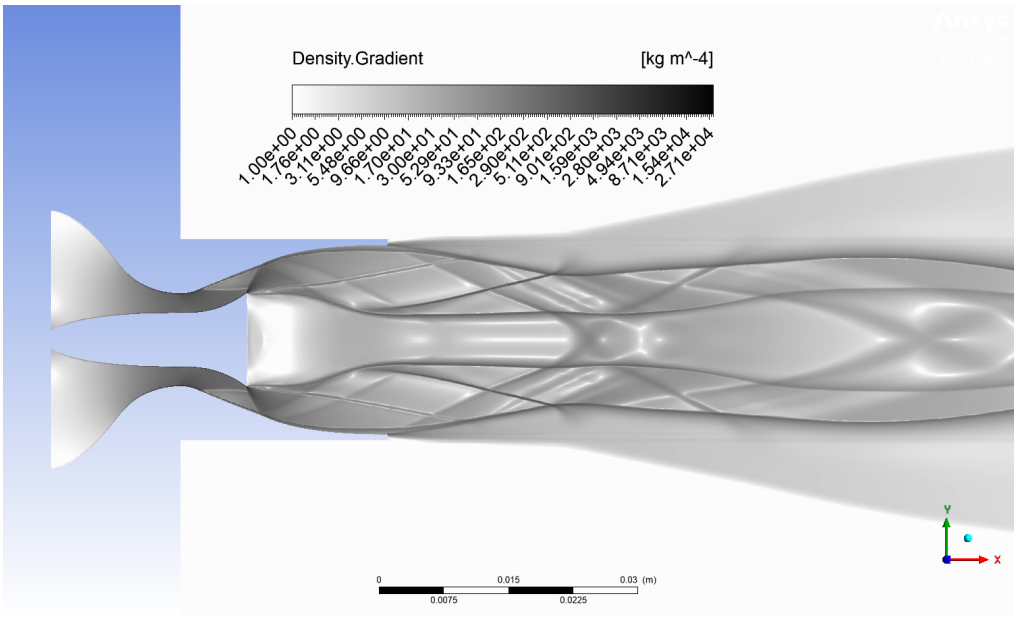


(a) Density gradient contour.

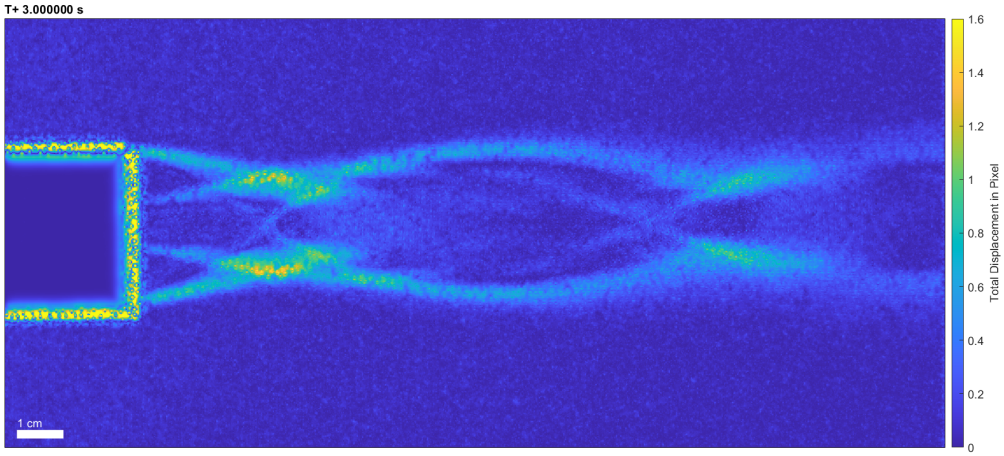


(b) BOS visualization.

Figure 8.4: ED case 1

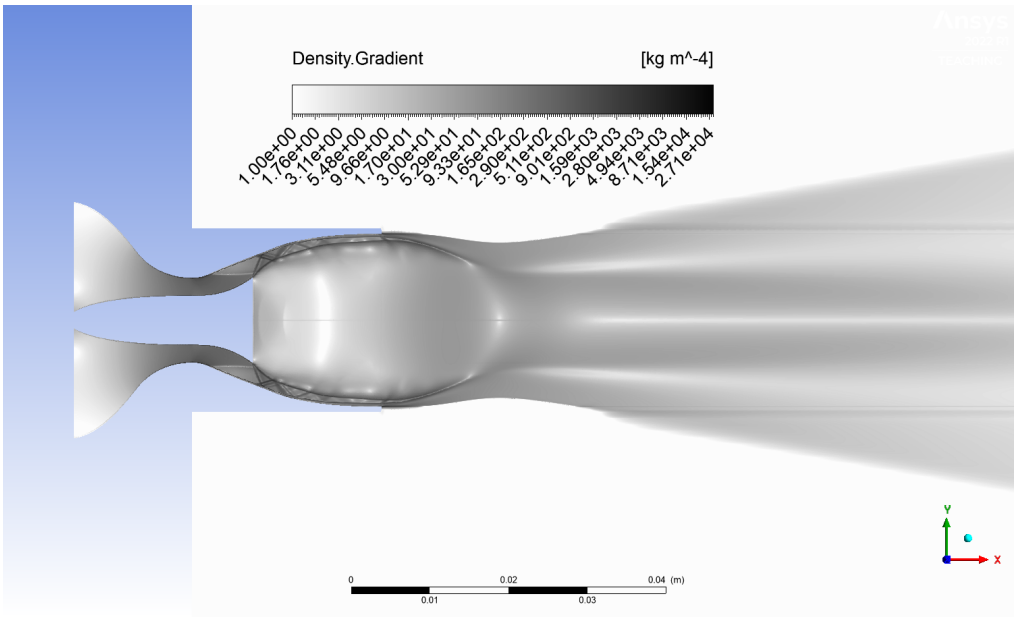


(a) ED case 2 – density gradient contour.

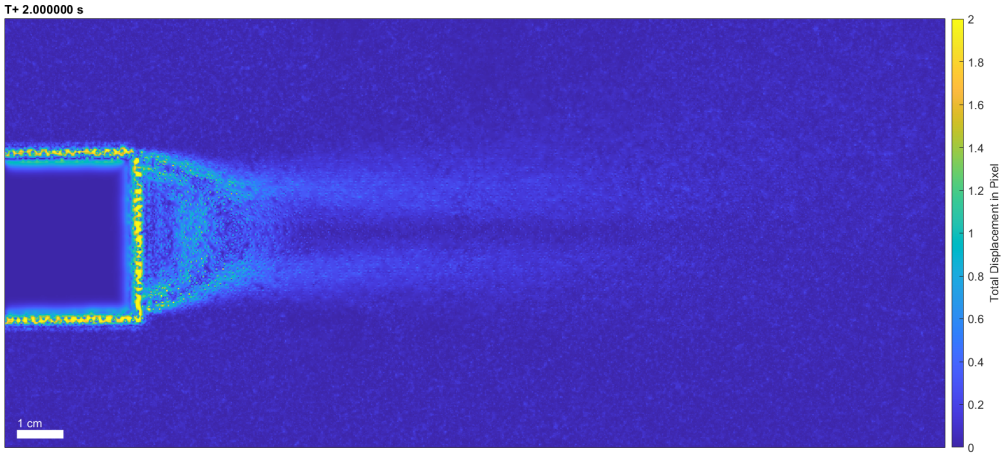


(b) ED case 2 – BOS visualization.

Figure 8.5: ED case 2

# *Chapter 9*

# *Discussion*

The results discussion is convenient to be separated into nozzle and aerodynamic performance. Special attention will be paid to variations between cases 4 and 2, and cases 4 and 3, in order to study how the retro-propulsion scenario influences these two performance aspects.

## 9.1 Nozzle performance

Each nozzle design, except for the expansion-deflection, was successfully verified and validated with great margins of uncertainty (error almost always lower than 5% in both cases). At sea-level (cases 2 and 4) TIC, AS and DB perform similarly better, in the range of 29-30 $N$ (ca. 7% better than RAO and ca. 30% better than ED, see table 7.4). The AS altitude compensation stands out, avoiding the normal shock wave and allowing it to reach optimal adaptation even at higher pressures.

Table 9.1: CFD nozzles performance variation (%) of case 4 (SubRP) compared to case 2 (SLS static burn).

| **Nozzle** | $F_x$ | $C_F$ | $I_{sp}$ | $NPR_{sim}$ | $p_e/p_a$ |
|---|---|---|---|---|---|
| RAO | 0.98 % | 1.02 % | 1.11 % | 2.18 % | -3.03 % |
| TIC | 0.74 % | -0.20 % | 0.70 % | 2.07 % | 1.71 % |
| AS | 0.82 % | 0.84 % | 0.84 % | 2.13 % | -0.12 % |
| DB | 0.31 % | 0.34 % | -0.15 % | 2.11 % | 1.86 % |
| ED | 2.22 % | 2.26 % | 2.26 % | 2.07 % | 0.19 % |

Table 9.1 shows the nozzle performance variations between cases 4 and 2 (equivalent without counter-flow). The presence of the counter-flow itself implies a non-zero dynamic pressure, which turns into a slightly lower static pressure in the

ambient. This translates into a ca. 2% higher $NPR$, meaning less over-expansion and better performance. Each nozzle presents an overall modest improvement in thrust, thrust coefficient, and specific impulse – most of all the ED, which re-gain a little more from the very poor performance of case 2. RAO nozzle displays the only counter-intuitive result, since the pressure expansion ratio lowers instead of increasing; this is probably due to the unpredictability of the normal shock wave that affects the accuracy of $p_e$ measurement.

## 9.2 Aerodynamic performance

From an aerodynamic perspective, the contours of Section 7.4 unveil the interplay of the collision between the counter-flow flow and the exhaust flow during subsonic retro-propulsion, as well as its interaction around the booster. As the nozzle jet meets the stagnation point, the flow assumes a drop-like shape, resulting in a turbulent recirculation exchange of momentum with the surrounding freestream and effectively nullifying its dynamic pressure. Subsequently, a fraction of the flow accelerates closely aligning with the original velocity of 60 $m/s$, remaining securely attached downstream along the vehicle's lateral walls. This happens for each nozzle without being subjected to specific effects from specimen to specimen, so $c_{ps}$ values are equally established at very low values close to zero.

If case 3 results do not show any particular difference among the various nozzles, during retro-propulsion major discrepancies emerge: ED nozzle presents the lowest values of drag (ca. 15% less than the average) and $c_{pb}$ (ca. 19% less than the average), along with the lowest $C_T$ and the shortest distance for the stagnation point – it's already been shown how, in fact, these last two variables seem to be directly correlated (see figure 7.16). RAO, AS and DB nozzles sit around similar aerodynamic performance – despite the diversity in shape of the nozzle itself and the jet plume – developing further stagnation points. Finally, the TIC generates the highest drag; a potential explanation is related to the fact that it's the smallest bell-shaped nozzle, both in length and width, which implies a thinner plume (smaller obstacle for the freestream) and more base surface that can interact with the counter-flow (rising at the same time also $c_{pb}$).

Table 9.2: CFD aerodynamic performance variation (%) of case 4 (SubRP) compared to case 3 (counter-flow only).

| **Nozzle** | $C_{ps}$ | $C_{pb}$ | $C_D$ | $D$ |
|---|---|---|---|---|
| RAO | 91 % | -53 % | -43 % | -43 % |
| TIC | 88 % | -52 % | -40 % | -40 % |
| AS | 87 % | -55 % | -42 % | -42 % |
| DB | 87 % | -56 % | -40 % | -40 % |
| ED | 87 % | -60 % | -47 % | -47 % |

Table 9.2 shows the aerodynamic performance variations between cases 4 and 3

(equivalent without the nozzle jet flow). If, regarding nozzle performance, the ED had the larger improvements, here it is true the opposite: the nozzle is responsible for the major decrease in terms of aerodynamic drag (-47%) and base pressure (-60%). This outcome contrasts with what was found in the experiments, where ED was subjected to the minor decline. However, in this case, the different counter-flow typology remarkably alters the comparison: the jet flow too easily demolishes the conical flow in proportion to the intensity of the thrust, potentially compromising the truthfulness of the result. Among the other nozzles, no significant differences appear, leading to the conclusion that the jet-flow shape doesn't seem to represent a primary importance variable for aerodynamic performance optimization.

# *Chapter 10*

# *Conclusions and Outlook*

## 10.1 Conclusions

In order to study the behavior of advanced nozzle concepts (ANCs) during the landing burn maneuver of a reusable launch vehicle (RLV), a comprehensive RANS numerical simulation campaign was conducted. The objective was to understand and compare the emerging flow patterns, the altitude compensation capability of such alternative nozzles, and the aerodynamic characteristics of the vehicle during subsonic retro-propulsion. These simulation models aim to closely resemble commercial RLVs like SpaceX's Falcon 9.

Therefore, the study consists of a four-case analysis, which provided a control group as a reference to study how jet-flow and freestream counter-flow affect each other. Nozzle designs and the simulation approach and methodology are described in detail, furnishing nozzle and aerodynamic performance results for static-burn, counter-flow only, and retro-propulsion tests. The latter sufficiently agree with the previous literature and with the expected analytical results evaluated from hand calculations. Moreover, the numerical study is validated through a parallel experimental campaign carried out in the vacuum wind tunnel of the Technische Universität Dresden (TUD) laboratory, which provided useful data and BOS images.

The static-burn simulations unveil outstanding performance for the aerospike nozzle: it directly competes with TIC and dual-bell, and outperforms the RAO, even at SLS conditions. This proves its specific ability to adapt the effective expansion ratio depending on the ambient condition. In contrast, the expansion-deflection nozzle demonstrates the poorest efficiency, making it an unappealing alternative to bell nozzles.

Simulations in counter-flow substantiate the expected flow pattern, as the strong influence of the cold jet-flow on the freestream in terms of surface body pressures

and drag (reductions up to 47%). The presence of different nozzles, whether they are on or off, does not significantly affect the aerodynamic characteristics of the vehicle. Nevertheless, the overall comparison in terms of total drag (aerodynamic drag + thrust-induced drag) put respectively TIC, aerospike, and dual-bell in the top three. The RAO performs just slightly worse, followed by the ED, which again reveals to be less preferable.

This thesis serves as a foundation for further investigations (suggested in the following section) into the performance of these nozzles in retro-propulsion, while adding valuable content to TUD's numerical database on ANCs. The findings affirm the promising potential of advanced nozzles; especially, the aerospike design demonstrates the ability to enhance the effectiveness of landing burn maneuvers and emerges as a viable contender to traditional bell nozzles for reusable main stages.

## 10.2 Outlook

As anticipated, this work presents several fronts for potential improvement depending on the needs. These are listed and discussed below:

- In order to reach a better optimization and match with the experimental setup, simulations using a conical flow model may represent a necessary step. This has actually already been attempted during the campaign, but many complications brought to the decision of choosing the uniform flow. The only possible way to recreate a flow topology similar to that obtained in the laboratory (reconstructed by measurements with a Pitot tube [28]) was using a still unpublished turbulence model: Generalized $k$-$\omega$ (GEKO). GEKO is a two-equation model, based on the $k$-$\omega$ model formulation, but with the flexibility to tune the model over a wide range of flow scenarios. The key to such a strategy is the provision of free parameters which the user can adjust for specific types of applications without a negative impact on the basic calibration of the model [43]. In addition to not being peer-reviewed, it brings the same issues of the experiments – such as the impossibility to study the pressure profiles on the side – and it moves away from the real case scenario. Nevertheless, this resource could represent a useful tool to actually mirror the experimental conditions.

- A further domain expansion to include the vehicle top and its wake effects, for a more complete evaluation of the drag resistance, which would come along with the proper mesh refinement. The HPC present at TUD could serve as a great resource in order to achieve this goal since the simulation context would start to become too heavy to be run on a personal computer.

- Review of convergence criteria and simulation stabilization.

- Expansion of the analysis to different design points (different $NPR$).

- Unsteady RANS simulations with increasing pressure over time, resembling the decreasing altitude during landing burn.
- Analogous numerical models using the large-eddy simulation (LES) method.

# *Bibliography*


[1] H. W. Jones. "The Recent Large Reduction in Space Launch Cost". *48th International Conference on Environmental Systems*, 2018.

[2] M. Ragab and F. McNeil Cheatwood. *"Launch Vehicle Recovery and Reuse"*. 2015. doi: 10.2514/6.2015-4490. URL `https://arc.aiaa.org/doi/abs/10.2514/6.2015-4490`.

[3] R. Allain. "The Physics of SpaceX's Wicked Double Booster Landing", 2018. URL `https://www.wired.com/story/the-physics-of-spacex-falcon-heavy-wicked-double-booster-landing/`. Available on line.

[4] H. Hagemann, G.and Immich, T. Van Nguyen, and G. E. Dumnov. "Advanced Rocket Nozzles". *Journal of Propulsion and Power*, 14(5):620–634, 1998. doi: 10.2514/2.5354. URL `https://doi.org/10.2514/2.5354`.

[5] G. Scarlatella, M. Tajmar, and C. Bach. "Advanced Nozzle Concepts in retro-propulsion applications for Reusable Launch Vehicle recovery: a case study". *72nd International Astronautical Congress (IAC)*, Oct. 2021. Dubai, United Arab Emirates.

[6] C. Tapia Mancera. "Numerical simulations of Advanced Rocket Nozzles for retro-propulsion in subsonic counter-flows". Master's thesis, Technische Universität Dresden, Feb. 2022.

[7] G. Scarlatella, J. Sieder-Katzmann, F. Roßberg, F. Weber, C. Tapia Mancera, D. Bianchi, M. Tajmar, and C. Bach. "Design and Development of a Cold-Flow Test-Bench for Study of Advanced Nozzles in Subsonic Counter-Flows". *Aerotecnica Missili & Spazio*, pages 1–13, May 2022. doi: 10.1007/s42496-022-00117-6.

[8] D. C. Freeman, T. A. Talay, and R. E. Austin. "Reusable launch vehicle technology program". *Acta Astronautica, 47th International Astronautical Congress*, 41(11):777–790, Oct. 1997. ISSN 0094-5765. doi: https:

//doi.org/10.1016/S0094-5765(97)00197-5. URL https://www.sciencedirect.com/science/article/pii/S0094576597001975. Beijing, China.

[9] M. T. Vernacchia and K. J. Mathesius. "Strategies for Reuse of Launch Vehicle First Stages". *69th International Astronautical Congress (IAC)*, 2018.

[10] S. Stappert, J. Wilken, L. Bussler, and M. Sippel. "A Systematic Comparison of Reusable First Stage Return Options". July 2019.

[11] SpaceX, Falcon 9. URL https://www.spacex.com/vehicles/falcon-9/. [Online; accessed 19.04.2023].

[12] SpaceX, Missions. URL https://www.spacex.com/mission/. [Online; accessed 19.04.2023].

[13] Wikipedia contributors. Falcon 9 flight 20 — Wikipedia, the free encyclopedia. https://en.wikipedia.org/w/index.php?title=Falcon_9_flight_20&oldid=1122732315, 2022. [Online; accessed 20-April-2023].

[14] T. Ecker, S. Karl, E. Dumont, S. Stappert, and D. Krause. "A Numerical Study on the Thermal Loads During a Supersonic Rocket Retro-Propulsion Maneuver". July 2017. doi: 10.2514/6.2017-4878.

[15] T. Ecker, F. Zilker, E. Dumont, S. Karl, and K. Hannemann. "Aerothermal Analysis of Reusable Launcher Systems during Retro-Propulsion Reentry and Landing". May 2018.

[16] D. Kirchheck, A. Marwege, J. Klevanski, J. Riehmer, A. Gülhan, S. Karl, and O. Gloth. "Validation of Wind Tunnel Test and CFD Techniques for Retropropulsion (RETPRO): Overview on a Project within the Future Launchers Preparatory Programme (FLPP)". Oct. 2019.

[17] G. P. Sutton and O. Biblarz. *"Rocket Propulsion Elements, Ninth Edition"*. John Wiley & Sons (US), 2017.

[18] D. H. Huang and D. K. Huzel. *"Design of Thrust Chambers and Other Combustion Devices"*, pages 67–134. doi: 10.2514/5.9781600866197.0067.0134. URL https://arc.aiaa.org/doi/abs/10.2514/5.9781600866197.0067.0134.

[19] G. V. R. RAO. "Exhaust Nozzle Contour for Optimum Thrust". *Journal of Jet Propulsion*, 28(6):377–382, 1958. doi: 10.2514/8.7324. URL https://doi.org/10.2514/8.7324.

[20] C. Bach. *"Systemanalyse und Prototypenentwicklung einer durch Fluidinjektion induzierten Schubvektorsteuerung für Aerospike-Triebwerke"*. Berichte aus der Luft- und Raumfahrttechnik. Shaker Verlag, Düren, 2020. ISBN 9783844072518.

[21] F. Zilker. "Aerothermal Analysis of Re-usable First Stage during Rocket Retro-propulsion". Master's thesis, Jan. 2018. URL https://elib.dlr.de/119265/.

[22] R. Bhaskaran. "A hands-on introduction to engineering simulations", 2021. edX.

[23] C. Liu J. Tu, G. H. Yeoh. *"Computational Fluid Dynamics: A Practical Approach, third edition"*. Katey Birtcher, 2018. ISBN 9780081011270.

[24] J. D. Anderson. *"Basic philosophy of CFD"*, pages 3–14. Jan. 2009. ISBN 978-3-540-85055-7. doi: 10.1007/978-3-540-85056-4_1.

[25] ANSYS. "Ansys Fluent Meshing User's Guide", Jan. 2016.

[26] W. L. Oberkampf and T. G. Trucano. "Verification and validation in computational fluid dynamics". *Progress in Aerospace Sciences*, 38(3):209–272, 2002. ISSN 0376-0421. doi: https://doi.org/10.1016/S0376-0421(02)00005-2. URL https://www.sciencedirect.com/science/article/pii/S0376042102000052.

[27] S. Nonaka, H. Nishida, H. Kato, H. Ogawa, and Y. Inatani. "Vertical Landing Aerodynamics of Reusable Rocket Vehicle". *Transactions of The Japan Society for Aeronautical and Space Sciences, Space Technology Japan*, 10:1–4, 2012.

[28] M. Portolani. "Investigation of effective altitude compensation of advanced nozzles in retro-flow configurations". Master's thesis, Politecnico di Torino, Apr. 2023.

[29] D. Surek and S. Stempin. *"Stationäre inkompressible Strömung; Hydrodynamik"*, pages 95–211. Oct. 2017. ISBN 978-3-658-18756-9. doi: 10.1007/978-3-658-18757-6_5.

[30] F. Roßberg. *"Set-up and commissioning of a counter-flow nozzle experiment in the vacuum wind channel"*. PhD thesis, Technische Universität Dresden, 2021.

[31] M. Propst, J. Sieder-Katzmann, J. Abel, E. Schwarzer-Fischer, U. Scheithauer, M. Tajmar, and C. Bach. "Influence of manufacturing accuracy on the performance characteristics of miniaturized ceramic cold-gas thrusters". May 2022.

[32] G. P. Sutton and O. Biblarz. *"Rocket Propulsion Elements, Eighth Edition"*. John Wiley & Sons (US), 2010.

[33] J. D. Anderson. *"Fundamentals of aerodynamics"*. McGraw-Hill, 6th edition, Mar. 2016. ISBN 9781259129919.

[34] K. Gutsche, A. Marwege, and A. Gülhan. "Similarity and Key Parameters of Retropropulsion Assisted Deceleration in Hypersonic Wind Tunnels". *Journal of Spacecraft and Rockets*, 58(4):984–996, 2021. doi: 10.2514/1.A34910. URL https://doi.org/10.2514/1.A34910.

[35] C. Tapia Mancera. "Spacetoolbox". https://github.com/carlostapiaman/spacetoolbox/tree/main/spacetoolbox. [Online; accessed 23.05.2023].

[36] M. Vernacchia. "Spike contour algorithm". https://github.com/mvernacc/aerospike-nozzle-design-gui. [Online; accessed 23.05.2023].

[37] Pangea Aerospace, Products. URL https://pangeaaerospace.com/products/. [Online; accessed 23.05.2023].

[38] G. Angelino. "Approximate method for plug nozzle design". *AIAA Journal*, 2(10):1834–1835, 1964. doi: 10.2514/3.2682. URL https://doi.org/10.2514/3.2682.

[39] F. Weber, D. Bianchi, and F. Nasuti. "Advanced nozzle concept trade-off and selection criteria based on launcher mission constraints". *9th European Conference for Aeronautics and Space Sciences (EUCASS)*, June 2022. Lille, France.

[40] A. Wimshurst. "Fluid Mechanics 101, Inflation Layer Calculator". URL https://www.fluidmechanics101.com/pages/tools.html. [Online; accessed 27.05.2023].

[41] Wikipedia contributors. Shock wave — Wikipedia, the free encyclopedia. https://en.wikipedia.org/w/index.php?title=Shock_wave&oldid=1155297301, 2023. [Online; accessed 30.05.2023].

[42] G. Scarlatella, T. Heuling, J. Sieder-Katzmann, F. Weber, M. Portolani, M. Garutti, D. Bianchi, A. Ferrero, D. G. Pastrone, M. Tajmar, and C. Bach. "Cold-Gas Experiments on Advanced Nozzles in Subsonic Counter-Flows". *Aerospace Europe Conference 2023 - 10th EUCASS - 9th CEAS*.

[43] ANSYS. "Best Practice: Generalized k-$\omega$ Two-Equation Turbulence Model in ANSYS CFD (GEKO)", Jan. 2019.

# Appendix A

# Matlab script for spike normal vector evaluation

The following script allows to evaluate the direction factor (cosine of the normalized normal vector) from a set of coordinates given in a .csv file. It is used to find the cosine of the curve spike wall equivalent angle for the aerospike nozzle.

```
clear all

format long

% F1 = readmatrix("KoordinatenTruncatedSpike.csv");
F1 = readmatrix("output_file_nnew2.csv");

dim = size(F1);

N = ones(dim(1)-1, 2);

N_len = zeros(dim(1)-1,1);

for i = 1:dim(1)-1

    % Calculate normal vector of the single line segment
    N(i,1) = -(F1(i, 2)-F1(i+1, 2))/(F1(i, 1)-F1(i+1, 1)
       );

    % Calculate the magnitude of this normal vector
    abs = sqrt(N(i,1)^2 + N(i, 2)^2);

    % Normalize the normal vector of the line segment
    N(i,:) = 1/abs*N(i,:);

    % Calculate the length of the line segment
```

```
    N_len(i) = sqrt((F1(i, 2)-F1(i+1, 2))^2 + (F1(i, 1)-
       F1(i+1, 1))^2);

end

% the individual lengths of the line pieces are related
   to the total length of the spike
length_curve = sum(N_len);
N_len = N_len/length_curve;

% Calculation of the "average" normal vector: Weighting
   of the individual
% normalized normal vectors of the line segments with
   the newly calculated
% length vector (length of line piece related to total
   length)
N_nom = N.'*N_len

% Calculation of the amount of the normal vector
N_nom_abs = sqrt(N_nom(1)^2 + N_nom(2)^2)

% Calculation of the direction factor (cosine of the
   normalized normal vector)
N_nom_alpha = N_nom(1)/N_nom_abs
```

# Appendix B

# Pressure coefficient along booster walls

This appendix displays the pressure coefficient profiles comparison between case 3 and case 4, both on the booster base and sides. As representative examples, the two best-performing nozzles (TIC and AS) graphs are below reported. The images clearly illustrate the impact of retro-propulsion, which reduces the base pressure while increasing the pressure on the sides, where the flow remains attached to the wall surface.

It is observed that the presence of a different nozzle has a more significant influence on the flow behavior at the base, in contrast to the sides where the pressure profiles are nearly identical, both in counter- and retro-flow.

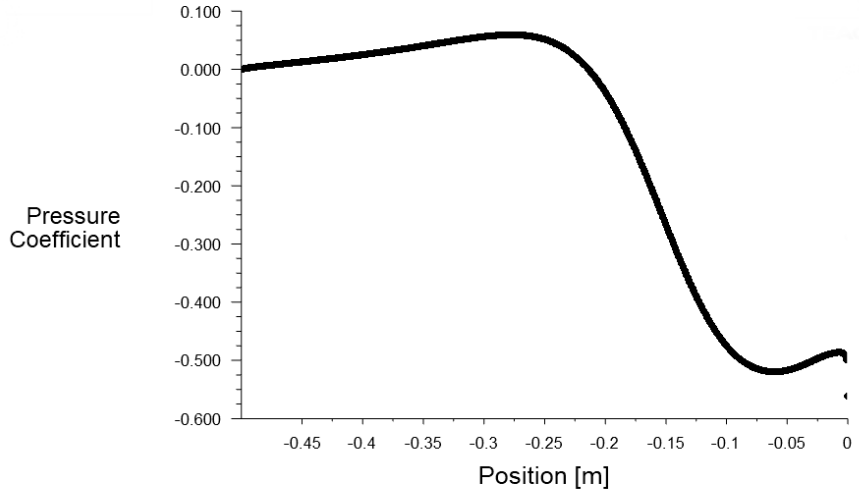


(a) Case 3.

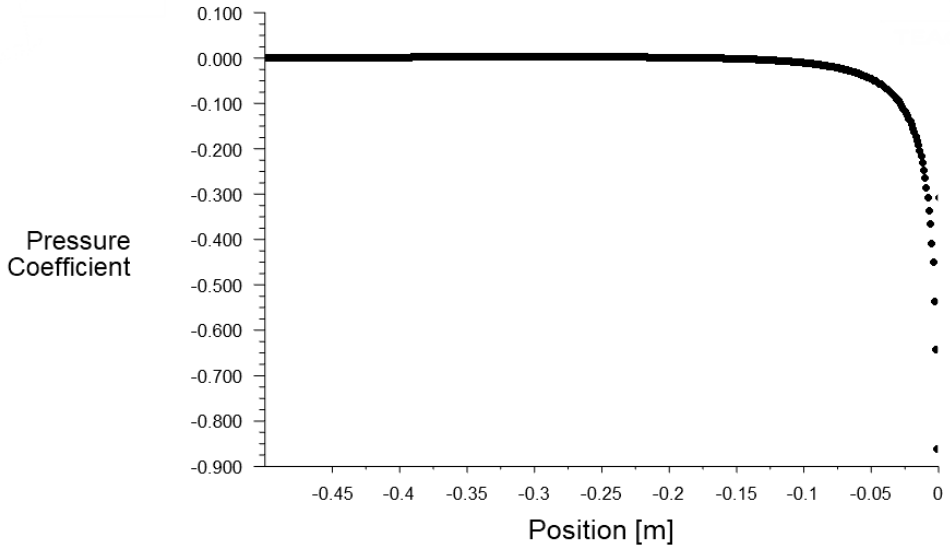


(b) Case 4.

Figure B.1: TIC pressure coefficient along booster side.

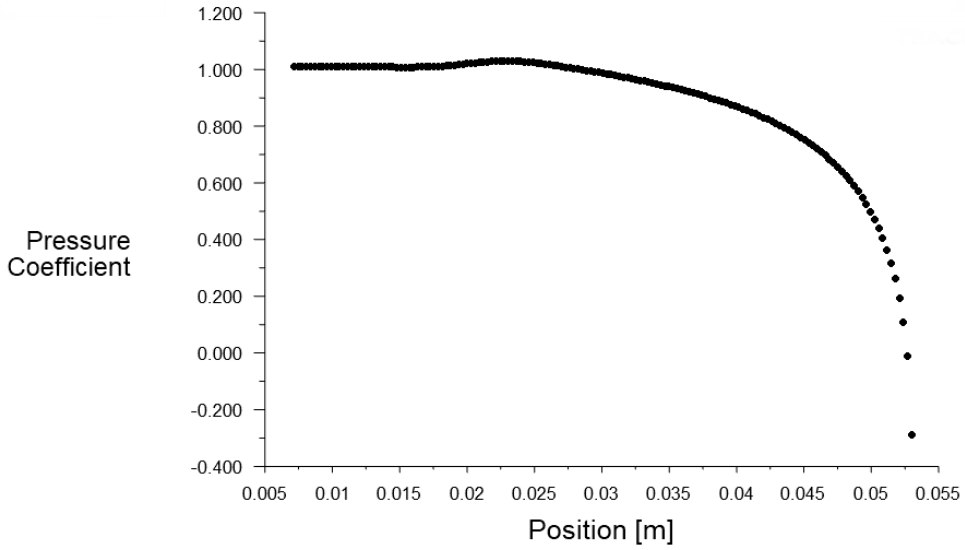


(a) Case 3.

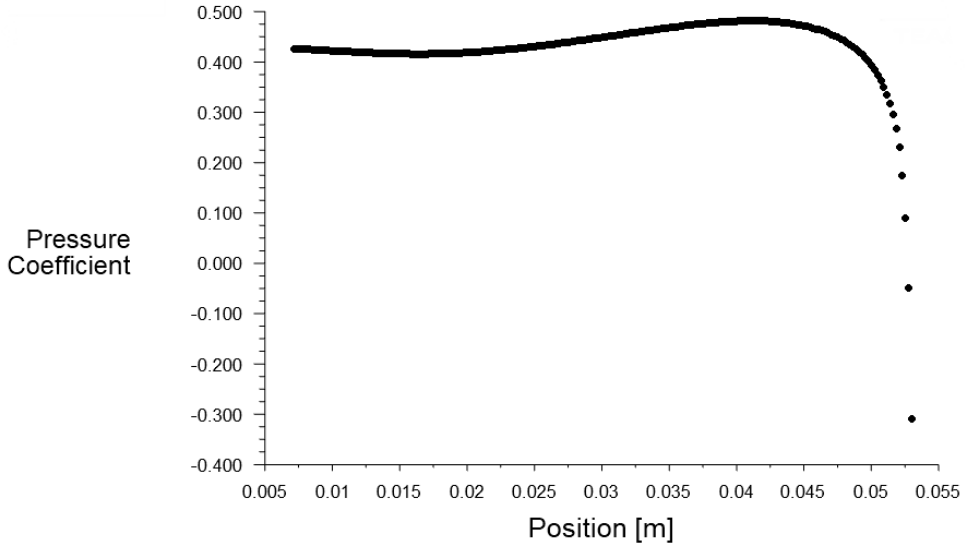


(b) Case 4.

Figure B.2: TIC pressure coefficient along booster base.

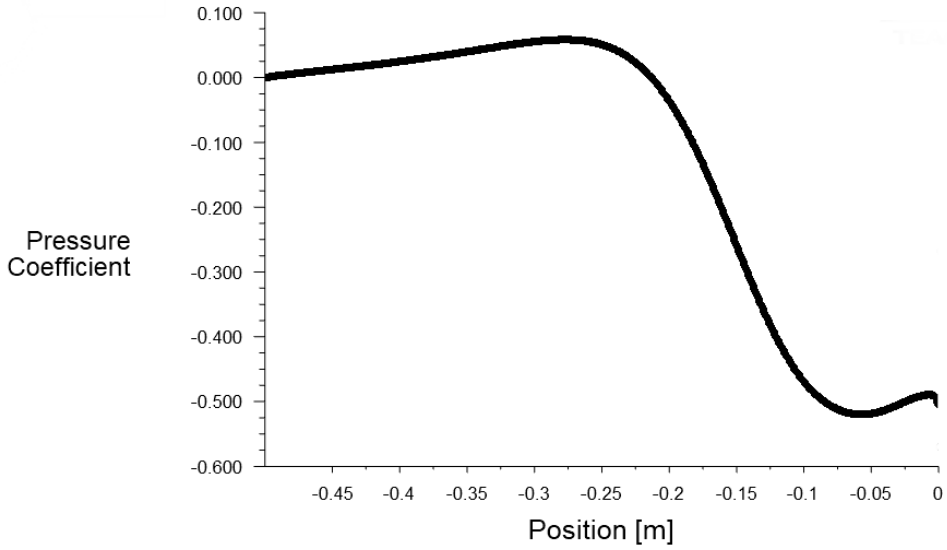


(a) Case 3.

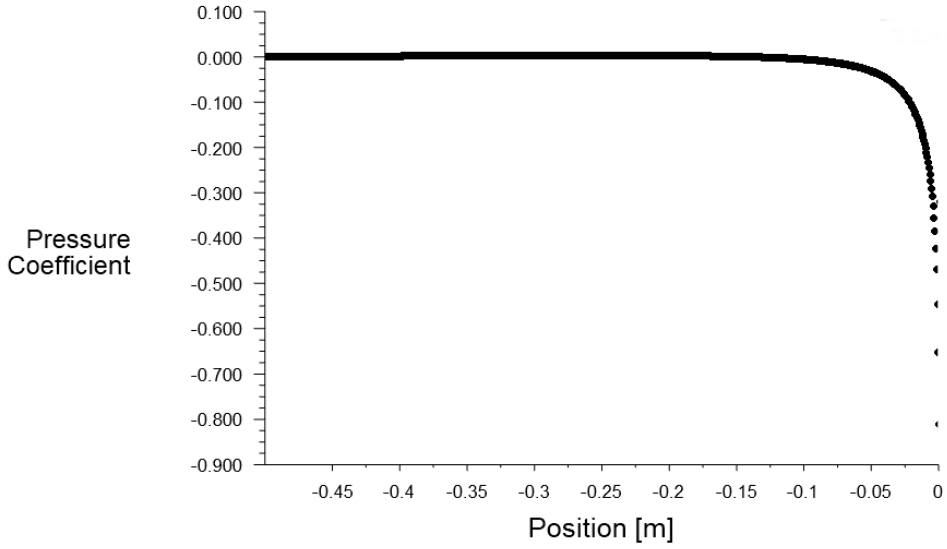


(b) Case 4.

Figure B.3: AS pressure coefficient along booster side.

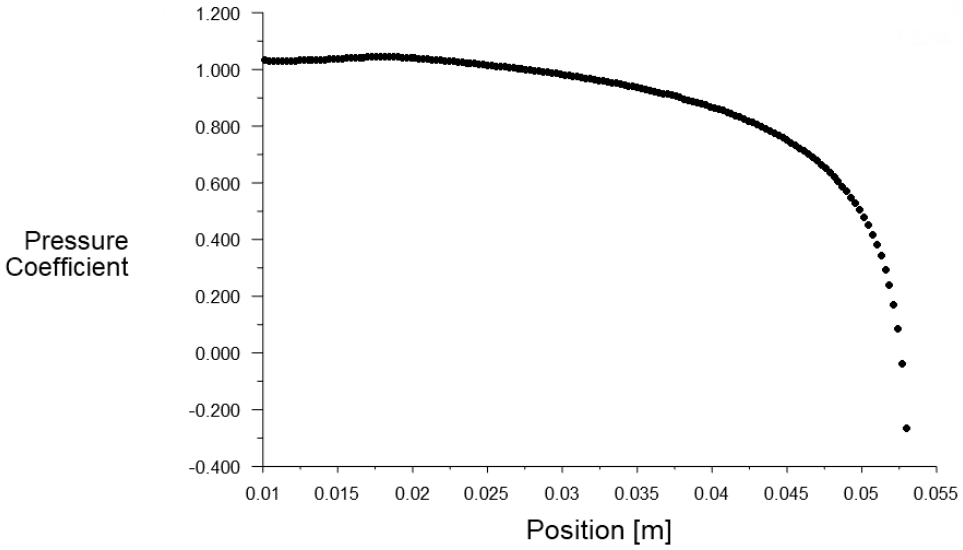


(a) Case 3.

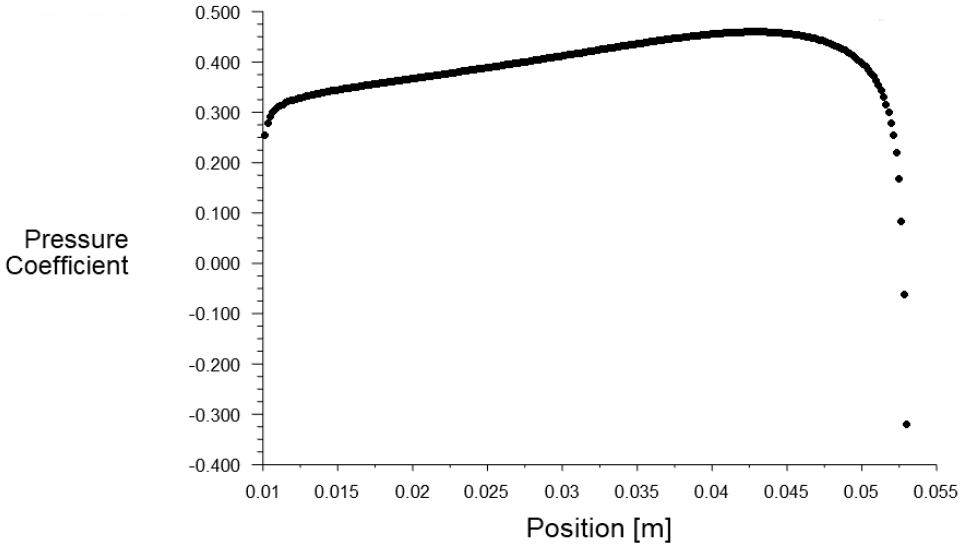


(b) Case 4.

Figure B.4: AS pressure coefficient along booster base.

# Appendix C

# Experimental measurements correction

This appendix briefly shows the variation of the experimental values of thrust and thrust coefficient after the $NPR$ adjustment. It should be noted that this caveat is not the purview of this thesis, and that the data shown are simply taken from the updated database in TUD.

Table C.1: Experimental values variation with $NPR$ adjustment.

| **Nozzle** | $F_x$ | | | $C_F$ | | |
|---|---|---|---|---|---|---|
| | exp. $[N]$ | adj. $[N]$ | var. | exp. $[N]$ | adj. $[N]$ | var. |
| RAO | 24.83 | 24.50 | -0.013 % | 0.88 | 0.87 | -0.011 % |
| TIC | 27.91 | 27.58 | -0.012 % | 0.99 | 0.98 | -0.010 % |
| AS | 28.47 | 28.25 | -0.008 % | 1.05 | 1.04 | -0.010 % |
| ED | 22.71 | 22.27 | -0.019 % | 0.81 | 0.79 | -0.025 % |

RAO, AS and ED are given, while the TIC adjustment is evaluated by averaging the variations of the others.

# Ringraziamenti

Per concludere, mi è doveroso dedicare questo piccolo spazio del mio elaborato a tutte le persone che hanno contribuito alla realizzazione dello stesso.

Ringrazio dunque il mio relatore Pavarin, e soprattutto il mio supervisore e co-supervisore esteri, Giuseppe e Martin, che mi hanno seguito e stimolato giorno per giorno in questi sei mesi di Erasmus.

Grazie anche ai miei colleghi di ufficio Marco Po.  e Leonardo, con cui ho condiviso questa esperienza.

Se sono arrivato fin qui, lo devo però anche a tutte le persone che mi hanno accompagnato in questi sei anni di università.

Innanzitutto, non potrò mai ringraziare abbastanza i miei genitori, che mi hanno permesso di intraprendere questo percorso supportandomi e sostenendomi quotidianamente.

Grazie a Mery, per aver sempre creduto ciecamente in me.

Grazie a Alice, Antonio, Asia, Chiara, Evan, Mattia B., Nicole, sempre stati parte integrante della mia vita.

Grazie a Lorenzo, Luca e Niccolò, con cui ho passato le infinite giornate di lezione e sessioni di esami, contribuendo ad alleggerirle.

Grazie anche ad Alba, Alejandra, Asja, Emanuela, Giulia, Julia, Marco Pr., Mattia P., Raquel e Violeta, per aver reso indimenticabile questo pezzo della mia vita a Dresda.

Grazie a tutti quelli che hanno contribuito anche in minima parte a tutto questo.

Infine, un piccolo grande grazie a me stesso, una persona con cui sono probabilmente spesso più ingrato di quanto non si meriterebbe, nella speranza che questo sia solo il primo passo della mia crescita professionale e personale.